DOCTORAL THESIS

Model Metal-Oxide Electrocatalysts for Energy Conversion

Modelové elektrokatalyzátory kov-oxid pro konverze energie

Modellsysteme für Metall-Oxid-Elektrokatalysatoren im Bereich der Energieumwandlung

under Cotutelle agreement between

Matematicko-fyzikální fakulta Univerzity Karlovy, Praha

Der Naturwissenschaftlichen Fakultät der Friedrich-Alexander-Universität Erlangen-Nürnberg

for obtaining a doctoral title Ph.D./Dr. rer. Nat.
submitted by

Lukáš Fusek

from Prague

I declare that I carried out this doctoral thesis on my own, and only with the cited sources, literature and other professional sources. I understand that my work relates to the rights and obligations under the Act No. 121/2000 Sb., the Copyright Act, as amended, in particular the fact that the Charles University has the right to conclude a license agreement on the use of this work as a school work pursuant to Section 60 subsection 1 of the Copyright Act.

In . . . . . date . . . .

Author's signature

Title: Model metal-oxide catalysts for energy conversion

Author: Lukáš Fusek

Departments:

Katedra fyziky povrchů a plazmatu, Matematicko-fyzikální fakulta univerzity Karlovy, Praha

Department Chemie und Pharmazie, Der Naturwissenschaftlichen Fakultät der Friedrich-Alexander-Universität Erlangen-Nürnberg

Supervisors:

doc. Mgr. Josef Mysliveček, Ph.D.

prof. Dr. Jörg Libuda

Keywords: model catalysis, metal-oxide catalyst, energy conversion

Table of Contents

Abstract

The development of novel (electro-)catalysts is commonly based on a trial-and-error approach without detailed understanding of the catalytic processes at the atomic scale. Reaching such understanding would be desirable, but, practically, it is not possible with real catalysts due to their structural and chemical complexity, and the presence of reaction environment. These limitations can be overcome following the model catalysis approach. In this thesis the elementary aspects of model catalysis are applied on electrochemical reactions to reach detailed understanding of fundamental electrocatalytic processes at the atomic level of various catalysts applicable in energetically relevant reactions. The studied model catalysts consist of rare metals (Pd, Pt) and reducible oxides (Co_3O_4, CeO_2). The main focus lied on the study of morphological and chemical properties of these systems in ultrahigh vacuum (UHV) and electrochemical environment combining surface science and electrochemical methods. The results show a clear link between the structural properties of the catalysts and their stability and performance in the electrochemical environment. The obtained level of understanding allows us to define key parameters to optimize the catalyst properties, identify adsorption sites and describe the elementary steps of catalytic reactions.

Vývoj nových (elektro-)katalyzátorů je běžně založen na metodě pokus-omyl bez detailního porozumění katalytickým procesům v atomárním měřítku. Přestože je dosažení takového porozumění žádoucí, není jej u reálných katalyzátorů možné dosáhnout vzhledem k jejich strukturní a chemické složitosti a přítomnosti reakčního prostředí. Tato omezení lze překonat pomocí modelové katalýzy. V této práci aplikujeme základní aspekty modelové katalýzy na elektrochemické reakce pro dosažení detailního pochopení základních elektrokatalytických procesů na atomární úrovni různých katalyzátorů použitelných v energeticky relevantních reakcích. Studované modelové katalyzátory se skládají ze vzácných kovů (Pd, Pt) a redukovatelných oxidů (Co_3O_4, CeO_2). Zkoumáme morfologické a chemické vlastnosti těchto systémů v UHV a reálném elektrochemickém prostředí kombinací metod povrchové fyziky a elektrochemických metod. Výsledky ukazují jasnou souvislost mezi strukturními vlastnostmi katalyzátorů a jejich stabilitou a výkonem v elektrochemickém prostředí. Získaná úroveň poznání umožňuje definovat klíčové parametry pro optimalizaci vlastností katalyzátorů, identifikovat adsorpční místa a popsat elementární kroky katalytických reakcí.

Die Entwicklung neuartiger (Elektro-)Katalysatoren beruht in der Regel auf einem Ansatz des Versuchs und Irrtums (engl.: trial-and-error), ohne dass ein detailliertes Verständnis der katalytischen Prozesse auf atomarer Ebene vorliegt. Obwohl ein solches Verständnis wünschenswert wäre, ist es für reale Katalysatoren aufgrund ihrer strukturellen und chemischen Komplexität und der vorhandenen Reaktionsumgebung praktisch unmöglich. Diese Einschränkungen können durch den Ansatz der Modellkatalyse überwunden werden. In dieser Arbeit wurden grundlegenden Aspekte der Modellkatalyse auf elektrochemische Reaktionen angewendet. Dadurch wurde ein atomares Verständnis der elektrokatalytischen Prozesse an verschiedenen Katalysatoren erreicht, die in für die Energiewandlung relevanten Reaktionen eingesetzt werden,. Die untersuchten Modellkatalysatoren bestehen aus Edelmetallen (Pd, Pt) und reduzierbaren Oxiden (Co_3O_4, CeO_2). Es wurden die morphologischen und chemischen Eigenschaften dieser Systeme im Ultrahochvakuum (UHV) und in elektrochemischer Umgebung untersucht. Dabei wurden oberflächenphysikalische mit elektrochemischen Methoden kombiniert. Die Ergebnisse zeigen einen klaren Zusammenhang zwischen den strukturellen Eigenschaften der Katalysatoren, ihrer Stabilität und den katalytischen Eigenschaften in elektrochemischer Umgebung. Das gewonnene Verständnis ermöglicht es, Schlüsselparameter zur Verbesserung der Katalysatoreigenschaften zu definieren, Adsorptionsstellen zu identifizieren und die elementaren Schritte katalytischer Reaktionen zu beschreiben.

1. Introduction

1.1. Catalysis and its role in hydrogen economy

The world energy consuption grew by almost 40% over last two decades.[1] An additional growth of more than 10% is predicted by 2040 due to increased demand of developing countries (Asia, Africa, South America).[2] This trend counters the urgent need of reducing the production of greenhouse gas emissions.[3,4] Therefore, transformation to sustainable energy sources is needed to maintain the production capacity and to reach zero net CO_2 emissions in 2050.[3,5] The transformation to renewable energy sources (RES) is already in progress. The share of RES on total energy consumption reached 20% in 2020.[6] According to plans of the European Council, the share of RES should further grow reaching 42.5% by 2030.[6–8]

RES suffer from high fluctuation of their power output caused by meteorological changes.[9,10] Thus, the increasing share of RES has to be accompanied by increasing energy storage capacity. However, the conventional storage technologies, such as a pumped storage power plant or lithium-ion batteries, cannot meet the increased demand. Therefore, new or improved storage systems have to be developed.[11,12]

The promising and extensively investigated approach is to store excessive electrical energy in the form of chemical energy.[9,13,14] Nowadays, a special attention is given to hydrogen as an energy storage vector.[15–17] The excessive energy from RES is used in electrolyzers to form hydrogen, which is stored, transported, and, if needed, converted in fuel cells back into electricity and water.[18–20] However, the storage and transport of hydrogen has distinct drawbacks that stem from its physical properties. Despite its high gravimetric energy density, the volumetric energy density of hydrogen is very low. Furthermore, a hydrogen molecule is small and light, and, thus, tends to leak. This makes a long-distance transport of hydrogen through pipelines prone to significant losses.[21–23]

There are several approaches to hydrogen storage and transport, which are considered. The conventional methods of storing hydrogen as a compressed gas or a cryogenic liquid requires extreme conditions – pressure or temperature. Furthermore, these methods suffer problems with scalability accompanied with increased safety risks.[22] Another possibility is to store hydrogen in vast underground storage facilities such as salt caverns or depleted natural gas deposits.[24] This approach offers large hydrogen storage capacity, but it is restricted only to

areas with convenient geological background and does not solve the problem with the transport. The last method of storing hydrogen in its pure form is physisorption in porous materials. A variety of different porous materials, such as hydrates, zeolites, carbon-based structures or metal-organic frameworks have been studied.[25–27] The limiting factor in this case is a weak interaction between hydrogen and solid resulting in low storage capacity. This can be overcome by using cryogenic temperatures, which, on the other hand, gives rise to further complications.[22,28]

Apart from the above described physical methods of storing hydrogen in its molecular form, there are chemical methods, where hydrogen is bonded chemically in a compound. The release of molecular hydrogen is triggered thermally or catalytically. Solid materials used for hydrogen storage are mostly represented by metal or metal alloy hydrides. The storage capacity of such material usually lies between 5 wt% H and 10 wt% H.[29–31] The operational conditions require elevated temperatures and high pressures (approx. 10 bars), which is not convenient, especially for mobile applications.

Liquid materials, on the other hand, are simpler to manipulate and offer the possibility of using the existing infrastructure. A promising storage vector is liquid ammonia. It shows exceptional gravimetric and volumetric hydrogen storage densities and there are already well-established ways of ammonia storage and transport. It can be liquified at room temperature at high pressure or at ambient pressure and temperatures below -33°C. However, the decomposition temperature exceeds 400°C. Furthermore, use of ammonia faces severe challenges mainly due to huge energy costs of the Haber-Bosch synthesis.[32]

Very promising, and extensively studied approach of hydrogen storage is the use of organic molecules, so called liquid organic hydrogen carrier (LOHC).[33]The concept of LOHCs is based on pairs of hydrogen-rich and hydrogen-lean molecules, which can be transformed reversibly between each other. The excessive hydrogen reacts exothermically with the hydrogen-lean molecule resulting in the hydrogen rich molecule. The release of hydrogen is triggered catalytically, usually at elevated temperature.[34] In comparison with previous methods, LOHCs are liquids, and stable for a long time at ambient conditions – room temperature and atmospheric pressure.[35] Variety of LOHCs were described in the literature. Dibenzyltoluene, methylcyclohexane and N-ethylcarbazole represent the present state-of-the-art LOHCs.[36] LOHCs show gravimetric storage capacity above 5%wt and volumetric storage capacity comparable to compressed hydrogen at 700 bars.[35,37]

1.2. Model (electro-)catalysis

Catalysis plays an important role in most of the above-mentioned chemical processes relevant to H storage, and, thus, in the whole hydrogen driven economy. A catalyst is the key component of fuel cells (FCs)[38,39], electrolyzers[40–42] and chemical storage converters[17,34]. Therefore, catalysis attracts scientific interest in order to optimize the processes involved in H storage, develop new useful materials and decrease the costs. Most of the catalysts involved in H storage are based on rare noble metals, such as platinum or iridium, which limits their widespread use.[43] This results in general tendency to replace rare metals with less expensive and more abundant materials or to reduce the amount of used rare metals.[44] However, it is nearly impossible to reach a detailed understanding of individual catalytical processes with real catalysts due to their high morphological and chemical complexity. To obtain molecular-level insight into catalytic processes model studies at well-defined catalyst surfaces and interfaces are required.[45]

Model heterogenous catalysis was introduced by Ertl in the 1970's, who used quickly developing experimental methods of surface science to investigate and describe morphological and chemical properties of catalysts, and reaction pathways of catalyzed reactions.[46,47] Scanning probe microscopies provided atomically resolved images of the model catalyst surface in real space, while various spectroscopic techniques offered a detailed information about the chemical composition, oxidation states of the catalyst, and the chemical states of adsorbates and intermediates. [48,49] This information helped to explain various catalytical processes and describe elementary steps of catalytical reactions.[50,51]

Similar approach can be applied in the field of electrocatalysis. However, studying solid/liquid interface raises additional challenges. Initially, the model electrocatalytical studies were limited to single crystal electrodes prepared by flame annealing[52] or in UHV and transferred into EC cell.[53,54] In order to mimic real catalyst surfaces better, the complexity of the model catalysts has to be systematically increased.[45,49,55,56] The electrocatalyst complexity can be increased in two ways (Figure 1.1) – by incresing the morphological complexity by introducing structural defects to the system[57] (e.g. controlling of the step density) or by increasing the chemical complexity by changing to model oxide surfaces[58], conventional[59] or inverse metal-oxide catalysts[60] or bimetallic alloys[61]. Preparation of these systems can be conducted under UHV conditions using experimental methods of surface science.[62] However, it is not possible to study the solid/liquid interface under ultra-high vacuum (UHV)

conditions. Therefore, novel approaches had to be developped. These experiments provide more realistic conditions, incorporating successfully a controlled transfer of the model electrocatalyst samples from UHV chamber to the electrolyte and back.[63] In general, information at four different levels – morphology and chemical state of the catalyst, stability of the catalyst, adsorption properties, and reaction pathways – can be obtained from a model electrocatalytical study.

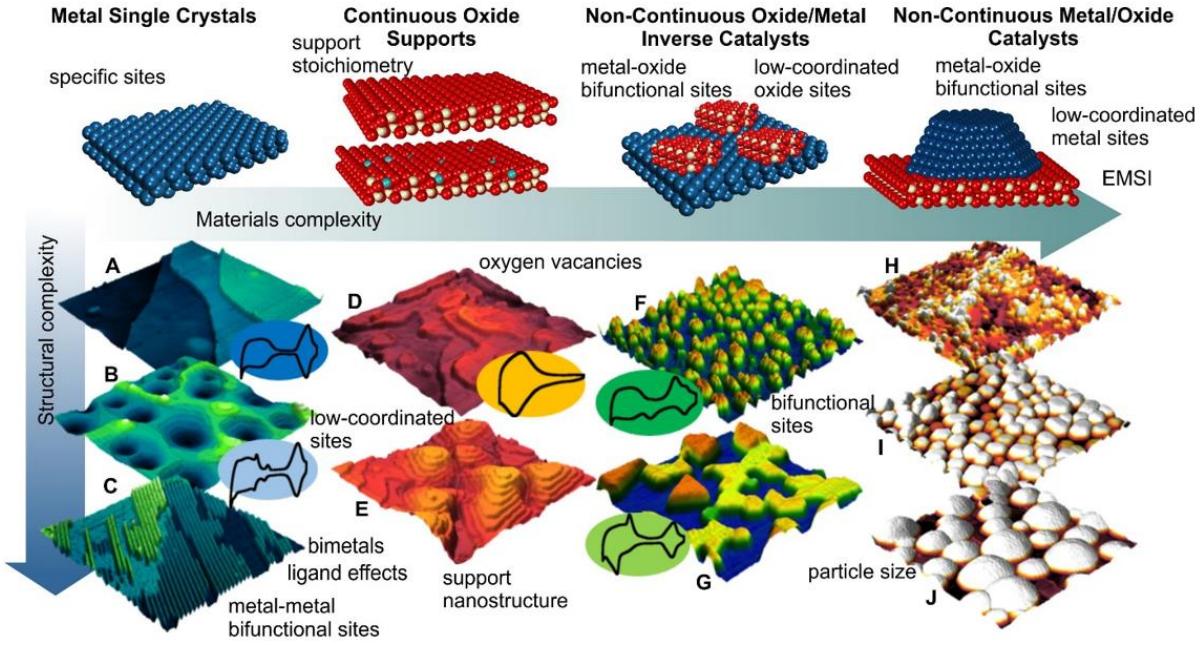

Figure 1.1: Two ways of increasing catalyst's complexity in model catalysis. STM images 100x100 nm^2 (A-G) and 50x50 nm^2 (H-J). Inlets are CV recorded in 0.1 M KOH. Authors: doc. Josef Mysliveček and Dr. Yaroslava Lykhach

Firstly, detailed information about the morphology and chemical state of as prepared catalyst can be obtained using the methods of surface science under UHV conditions. In the case of oxide supported metal nanoparticles, the morphology and the chemical state are strongly affected by the interaction of the metal with the oxide support. This interaction is typically associated with charge transfer and it is called electronic metal-support interaction (EMSI). Secondly, the model electrocatalyst is transferred in an ultra-clean fashion into electrochemical cell to study the stability and behaviour of the electrocatalyst in the electrochemical environment. Various changes can occur after exposure of the as-prepared catalyst to electrochemical conditions. Namely, it may be dissolution of the catalyst, etching of the catalyst surface, sintering of the catalyst nanoparticles or diffusion of the catalyst into bulk.[64,65] From the chemical point of view, the change of the catalyst composition and

oxidation state is very important.[58,66,67] All above effects could be triggered by contact with electrolyte with a given pH, and a particular applied potential. Long-term morphological and chemical stability under the operational conditions represents one of the key requirements for an applicable electrocatalyst.

Thirdly, we obtain information about adsorption sites, adsorbates and their binding on the catalyst surface. Atomically resolved geometry of adsorption sites, their density and reactant/intermediate/product adsorption energy are the parameters determining the catalytical reaction.[68,69] Experimental methods of surface science allow to control crystallographic orientation of model catalyst surfaces, and the character and density of defects on the catalyst surface. Control of the character and density of the adsorption sites allows to obtain control over the catalyzed reaction.[70,71] Model catalyst surfaces can be also modified with a layer of adsorbate. In example, a functional organic film on catalyst surface may affect its activity or selectivity.[72] Additionally, these systems are also widely used in various applications outside of catalysis, such as photovoltaics[73,74], molecular electronics[75,76] or gas sensing[77,78].

Lastly, it is the information on the catalytic reaction itself. A devolepment of real catalysts has been traditionally based on trial-and-error approaches. However, a detailed understanding of the elementary steps of the catalytic reaction allows us to improve the catalyst properties in a knowledge-based manner.[46,47] Both, activity and selectivity can be tuned by above mentioned morphological and chemical properties of the catalyst.[71,79] Therefore, model studies can enlighten the already established catalytic processes and identify the parameters to be optimized for further improvements of the real catalysts. For example, Besenbacher decribed the role of MoS_2 nanoclusters for hydrodesulfurization reaction, and proposed a real catalyst.[80] Similarly, Rodriguéz's results about inverse CeO_2/Cu catalyst lead to a development of a real catalyst for water-gas shift reaction.[81]

1.3. Scope of the Thesis

This Thesis was conducted at Department of Surface and Plasma Science at Charles University in Prague, Czech Republic, and at the Department of Chemistry and Pharmacy of the Friedrich-Alexander University in Erlangen, Germany. The thesis focuses on application of the above described approach combining UHV surface science methods and electroanalytical methods for investigations of electrified solid/liquid interfaces. One important achievement at our department at Charles University was the implementation of the

electroanalytical experimental methods, which can benefit from a synergy with already well developed surface science methods.

From a scientific point of view, this thesis focuses on identifying morphological and chemical properties of model metal-oxide catalysts for selected chemical reactions relevant for energy conversion and storage. The oxides play a crucial role in the electrocatalysis as a a catalyts material or catalyst modifier. Their surface structure and chemical states, which determine catalytic properties, show high complexity. Therefore, the model approach is required to bring an important insight into their elementary electrochemical processes. This thesis addresses all four aspects of model electrocatalysis described in the previous section – state of the as prepared electrocatalyst and its stability in the electrochemical environment, adsorption sites of the electrocatalyst surface, and electrocatalytical reaction pathways. The investigated model catalyst systems consist of rare metals (Pt, Pd) in combination with reducible oxides (CeO_2, Co_3O_4) in both the conventional geometry with metal nanoparticles supported on oxide substrate, and the inverse geometry with oxide nanoparticles supported on metal substrate.

The selected materials provide synergistic bi-functional effects. Platinum group metals are well-known for their good catalytical properties. They are at the top of Volcano plots for various energetically relevant reactions including hydrogen evolution reduction (HER) and oxygen reduction reaction (ORR).[82,83] On the other hand, catalytic applications of reducible oxides benefit from its intristic ability to change the oxidation state. As a result, oxides can quickly provide oxygen to the reaction. Furthermore, oxide supports can help to stabilize well-dipersed metal nanoparticles against sintering, thus increasing the noble metal efficiency.[84,85] In a limiting case, this results in a concept called single atom catalyst, where the noble metal is atomically dispersed on the oxide support reaching the maximum of noble metal efficiency.[86,87] Reducible oxides are also less expensive and more abundant than rare metals. Therefore, the combination of these two classes of materials can potentially lead to designing highly active, highly selective, stable, and economical electrocatalysts.

1.4. Reducible oxides

1.4.1. Cerium oxide

Nowadays, cerium oxide is implemented in many catalytical applications, e.g. CO oxidation[88], water-gas shift[89], alcohol oxidation[90], NO reduction[91]. There are two stable forms

of cerium oxide with cerium in oxidation state Ce(III) or Ce(IV). The fully reduced Ce_2O_3 has a hexagonal or a cubic bixbyite structure while the fully oxidized CeO_2 (ceria) has a fluorite structure.[92] The surface of fully oxidized CeO_2 can be easily reduced, and therefore, can serve as a reservoir of oxygen for catalytical reactions that involve an exchange of oxygen.[93] It has been shown that crystallographic structure of partially reduced CeO_{2-x} is based on fluorite structure with Ce atoms close to FCC positions and with several well-defined crystallographic structures determined by oxygen vacancy ordering (Ce_7O_{12}, $Ce_{11}O_{20}$, Ce_6O_{10}…).[94]

For the purpose of model catalysis, ordered surface of ceria is typically obtained in the form of a ceria thin film deposited on metal or oxide substrate. The three low-index ceria planes – (100), (111), (110) – differ in catalytic activity, chemical stability, density of available oxygen atoms and Tasker classification.[94] CeO_2(111) is the most stable and the most studied surface. It is prepared by cerium deposition in O_2 atmosphere on close-packed surfaces of metals. Various studies has been published for Pt(111), Cu(111), Au(111), Pd(111), Ru(0001) or Rh(111).[94] In this work, the focus is on CeO_2(111)/Pt(111) model catalysts.

Pt/CeO_2 catalyst were extensively studied as a suitable electrode for proton exchange membrane fuel cell (PEMFC)[95,96] application due to its enhanced ORR activity and tolerance against CO poisoning. However, the applicability of this system is not limited to fuel cells. The energetically relevant applications include various oxidation processes – CO oxidation, methanol and ethanol oxidation, hydrogen storage systems, water-gas-shift (WGS) or photocatalytic reactions.[97] Therefore, the material properties of Pt/CeO_2 were investigated in detail.

The group of Paola Luches conducted detailed surface science studies on the preparation, morphology, chemical state, thermal stability and behaviour under redox conditions of ceria thin films on Pt(111).[67,98–103] Ceria forms large, flat islands with fluorite structure. Island edges are alinged with the main crystalographic directions of Pt(111).[100,101] After annealing in oxygen, the islands consist mainly of Ce^{4+} ions. This structure is stable when exposed to air.[67] Ceria can be reduced by thermal treatment in vacuum or by redox processes in gas atmosphere. Small changes are observed in the film morphology during the reduction, and the film maintains its crystallinity, changing the structure from fully oxidized fluorite to fully reduced bixbiyte.[99] This process is reversible and the initial fluorite structure is recovered by

annealing the film in oxygen. Model electrocatalytic studies on CeO_2 are, however, not available so far.

1.4.2. Cobalt oxide

Another oxide material, which is broadly used in (electro-)catalysis is cobalt oxide. Cobalt belongs to the iron triad (Fe, Co, Ni). Oxides of these transition metals are gaining popularity in catalysis as a less expensive alternative to noble metals.[69] The possible use of cobalt oxide ranges from biomedical applications[104] through gas sensing materials[105], lithium-ion batteries[106] to various catalytic applications. For example, it serves as a electrocatalyst for the hydrogen and oxygen evolution reactions[69], oxygen reduction reaction[107], oxidation of CO[108,109] or formaldehyde[110]. Several model studies focused on using Co_3O_4 as a cathode for Zn-air batteries.[111,112] Apart from that, adsorption of organic molecules onto Co_3O_4 have been studied for an application as an organic-oxide hybrid material.[113,114]

Cobalt oxide has two stable forms – CoO with a rocksalt crystal structure and Co_3O_4.[115] The latter is a mixed oxide containing Co^{2+} and Co^{3+} ions in a ratio 1:2. It crystallizes in a spinel structure with Co^{2+} ions positioned in tetrahedral sites and Co^{3+} ions in octahedral sites.[116] Thin films of these oxides can be prepared on the surface of Ir(100). The films grow preferentially in (111) orientation. Co_3O_4(111) is terminated by Co^{2+} ions in a hexagonal unit mesh with a unit cell lenght of 5.7 Å. Typical step height ranges from 4.6 – 4.7 Å. However, strong relaxations of Co and O positions are observed near surface due to the compensation of the surface dipole. [117]

Co_3O_4 can easily lose oxygen and transform to CoO. Biedermann et al. observed oxygen release from Co_3O_4 films during annealing to 800 – 900 K in vacuum as a function of the film thickness showing that only rocksalt CoO is stable above 900 K.[116] They also showed that minimum film thickness of approx. 3-4 Co_3O_4 bilayers is required to form a stable structure at lower temperatures. Only CoO exists below this value. Due to these restrictions, a complex preparation procedure[115,117] is required to form a well-ordered stochiometric Co_3O_4.

Co_3O_4(111) is typically prepared on Ir(100) substrate by evaporation of Co in an oxygen atmosphere at room or liquid nitrogen (LN_2) temperature with subsequent annealing in oxygen atmosphere and UHV. Prior to the deposition, an oxygen (2x1) superstructure is formed on the reconstructed Ir(100)-(5x1).[115,117] Detailed description of the preparation procedure is given in Section 3.1.2.

2. Theory and fundamentals

2.1. Scanning tunneling microscopy

Scanning tunneling microscopy (STM) was introduced by Binnig and Rohrer in 1982 as a new microscopic technique with an unprecedented resolution on the atomic scale.[118] The principle of STM is based on the quantum tunneling effect. In contrast to classical physics, a particle in quantum physics, represented by a wave function, has a non-zero probability of penetrating through a potential barrier, which is higher than the energy of the particle (Figure 2.1). For a square barrier, the tunneling probability is given by the transmission coefficient T

$$T \propto e^{-2d\sqrt{\frac{2m(V_0-E)}{\hbar}}}, \tag{2. 1}$$

where V_0 is the height of the barrier, d width of the barrier, m mass of the particle, and E its energy.[119]

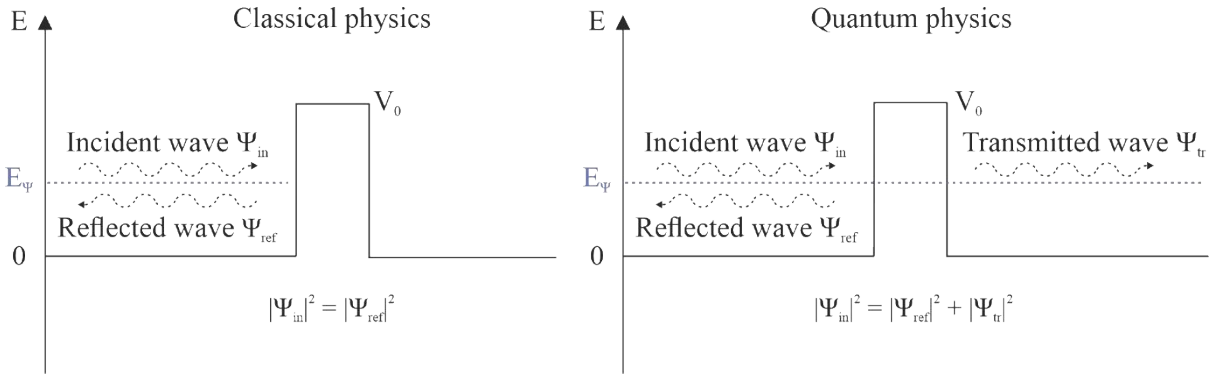

Figure 2.1: Quantum tunneling. Difference between classical physics, where the incident wave is fully reflected, and quantum tunneling, where the incident wave is partially reflected and partially transmitted.

In the case of STM, the tunneling particle is an electron, and it is tunneling through a metal-insulator-metal junction. More specifically, an electron is tunneling between a conductive planar sample and a sharp metal tip in the proximity of the sample through a vacuum (Figure 2.2a) with an applied bias voltage between the tip and the sample. Based on the polarity of applied bias voltage, the electrons can tunnel either from occupied states of the tip into unoccupied states of the sample or vice versa (Figure 2.2b).

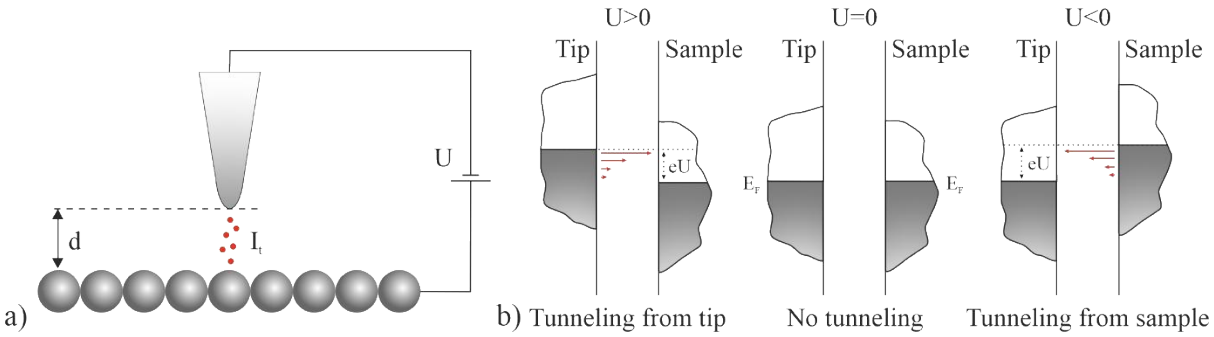

Figure 2.2: a) Schematic drawing of STM geometry – a metal tip is scanning in the proximity of the sample's surface with an applied bias voltage between the tip and the sample. b) The effect of bias voltage polarity on tunneling: If there is no bias voltage, the Fermi levels of the tip and the sample are aligned, and no tunneling occurs. In the case of positive bias at the surface ($U > 0$), the electrons tunnel from the occupied states of the tip into unoccupied states of the sample. On the other hand, if $U < 0$, the electrons are tunneling from the sample's occupied states to the unoccupied states of the tip.

Due to the applied bias voltage U, the potential barrier has, in the first approximation, a triangular shape. Therefore, we can get the first estimate of tunneling current from the Fowler-Nordheim theory of field emission[120]

$$I_t \propto \frac{U}{d} e^{-\frac{d}{U}},$$

(2. 2)

where d stands for tip-sample distance. Fowler-Nordheim theory in this form is valid for two planar surfaces. Bardeen's theory provides a more precise calculation of the tunneling current.[121] In this case, the electrons tunnel from a metal A (tip), described by spatial wavefunctions ψ_m, to a metal B (sample), described by spatial wavefunctions φ_n. Calculations show that the tunneling probability is highest for elastic tunneling, where the initial and final state have the same energy $E_m = E_n$, and drops quickly for $E_m \neq E_n$.[122] Assuming the elastic tunneling, the tunneling current reads[121,123]

$$I_t \propto \int_{-\infty}^{\infty} \rho_A(E + eU)\rho_B(E) \times [f(E) - f(E + eU)]|M_{mn}|^2 dE,$$

(2. 3)

where ρ_A, ρ_B stands for density of state of metals A and B, f(E) is the Fermi distribution function and M_{mn} is a tunneling matrix coefficient:

$$M_{mn} = \frac{\hbar^2}{2m}\int \psi_m \frac{\partial \varphi_n^*}{\partial z} - \varphi_n^* \frac{\partial \psi_m}{\partial z}\, d\mathbf{S}.$$

(2. 4)

The integration is over a separation surface between metals A and B.

Bardeen's theory faces several drawbacks. The main one is the complicated calculation of the tunneling matrix coefficient. A widely used approach to model the tunneling current is the Tersoff-Hamman approximation.[124,125] It is based on Bardeen's theory with two simplifications. Whereas the sample is treated exactly, the STM tip is supposed to have spherical symmetry and only s-orbitals are considered. Additionally, the approximation is limited to small voltages. Under these assumptions, the tunneling current is

$$I \propto V\rho_A \sum_n^{\square} |\varphi_n(\boldsymbol{r_0})|^2 \delta(E_n - E_F).$$

(2. 5)

Please note that the sum is simply the local density of states of the sample at the tip position.[125] Due to its simplicity and reliability, the Tersoff-Hamman approximation is the most used approach in modeling STM current.[126–128]

Even though the theoretical background of STM was known for decades, the experimental implementation was challenging. Binnig and Rohrer mentioned in their paper two main difficulties – vibration isolation and a sufficiently precise scanner.[118] Assuming that tip-sample distance is in the range of several angstroms[129,130] and tunneling probability depends exponentially on this distance (Eq. 0.1), exceptional vibration stability is required. The two-step spring system introduced by Binnig and Rohrer in their initial work effectively suppresses vibrations in the frequency range >1Hz.[118] Modifications of this system are used as a commercial standard in modern STMs.

The STM scanner is based on the inverse piezoelectric effect.[131,132] The piezosensitivity of STM scanners lies in the range of $1 - 5\ \mathrm{nm/V}$, which provides sufficiently precise control of the scanner movement.[133] The originally used tripod geometry consists of three piezo-rods in orthogonal configuration controlling separately the movement in x, y, and z direction.[118] A single-tube geometry quickly replaced this design.[134] The scanner is made out of a tube from piezoelectric material. Both inner and outer surfaces are covered with metal and serve as electrodes. The tube scanner is simpler than a tripod geometry and has higher resonance frequency and piezosensitivity. Therefore, it is better suitable for STM.

In the STM, we distinguish two resolutions – z-resolution and lateral resolution. The z-resolution is mainly determined by the changes in the tunneling current. The exponential dependency makes resolving heights down to one-tenth of Angstrom possible. More crucial is the lateral resolution, which strongly depends on the size and shape of the tip.[135] The radius of the tip is typically several tens of nm.[136] However, it was shown that more than 90% of the tunneling current goes through the atom closest to the surface (Figure 2.3a).[122] Therefore, it is possible to reach the atomic resolution.

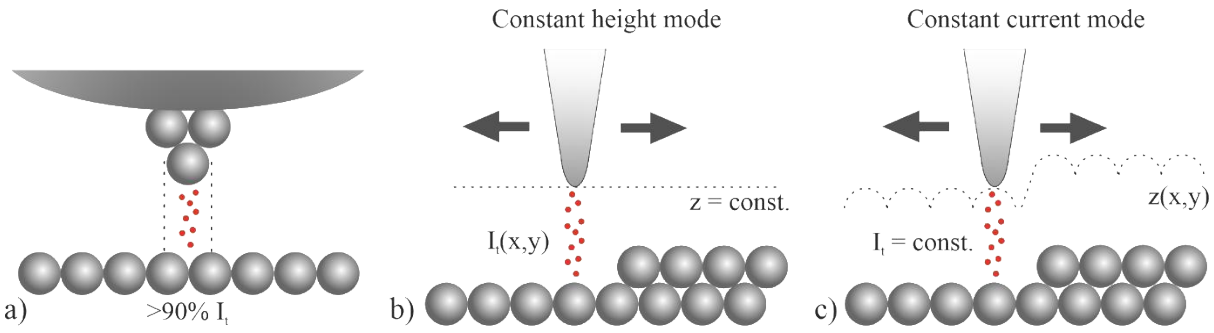

Figure 2.3: a) The majority of the tunneling current goes through the tip's atom closest to the surface. b) Constant height mode – tunneling current changes during scanning based on the surface morphology. c) Constant current mode – feedback loop is adjusting z-coordinate to keep tunneling current constant, z(x,y) directly reflects surface morphology.

The STM is usually operated in one of the following modes – constant height mode (Figure 2.3b) and constant current mode (Figure 2.3c). In the first case, the tip is held at constant height (z-coordinate). While scanning, the tip-sample distance changes due to surface morphology and, consequently, the tunneling current changes. We can calculate the surface morphology by recording the tunneling current as a function of x, y. The constant height mode is suitable only for scanning small areas of extremely flat surfaces. On the other hand, in the more often used constant current mode, the feedback loop adjusts the tip height to keep the tunneling current constant. Visualization of $z(x, y)$ provides a view of the surface morphology.

2.2. Photoelectron spectroscopy

While STM reveals surface morphology, photoelectron spectroscopy offers information about the surface's chemical composition and chemical states. The principle is based on the photoelectric effect.[137] The surface is exposed to monochromatic electromagnetic radiation, usually, X-rays (X-ray Photoelectron Spectroscopy, XPS), which leads to an emission of

electrons from core levels. The emitted electrons are filtered by their kinetic energy in an analyzer and subsequently counted at a detector. If there is an electrical contact between the sample and the analyzer, kinetic energy of the photoelectrons depends only on the wavelength of the X-ray beam ν, the analyzer's work function χ_{an} and the binding energy of the photoelectron E_B (Figure 2.4)[138]

$$E_k = h\upsilon - E_B - \chi_{an}.$$

(2. 6)

Photon energy and the analyzer's work function are known parameters of an experimental setup. Consequently, kinetic energy is directly related to electron binding energy, which is characteristic for each element. Therefore, peak positions of the XPS spectrum reflect the chemical composition of the sample. Please note, that photoionization of an electron from a different than s-orbital results in a doublet because of spin-orbit splitting. After photoionization, the unpaired electron left in the orbital can be in two energy states depending on whether the spin and the angular momentum of the unpaired electron are parallel or antiparallel.[138]

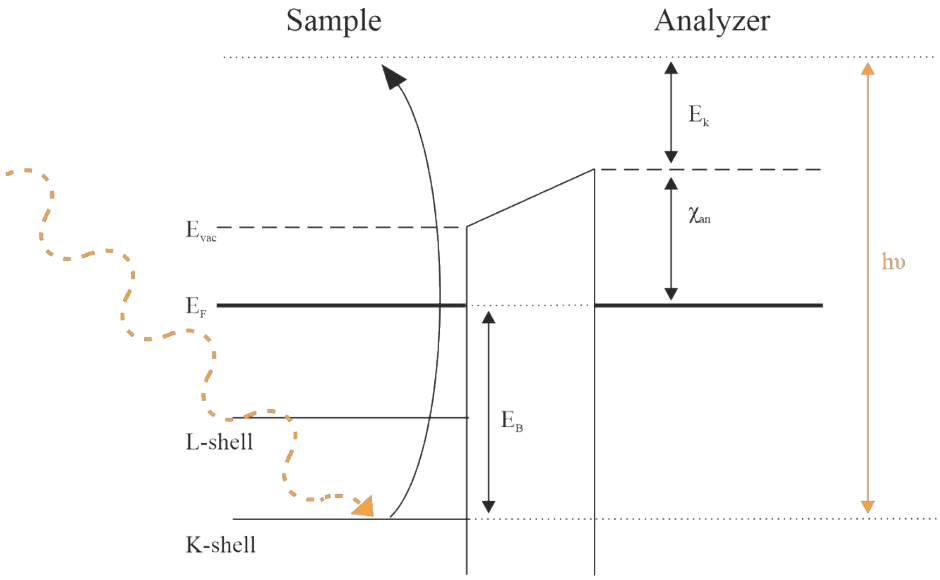

Figure 2. 4: Energy diagram of XPS

The electron binding energy is an energy difference between the final ion and the initial atom. In the first approximation, it is only the energy of the orbital determined relative to the Fermi energy. However, additional effects have to be considered for a detailed analysis of the XPS spectra, such as initial state effects, final state effects, or relativistic correction.[139–141] The most important initial state effect is a chemical shift. The binding energy changes as a

function of the atom surroundings. This reflects differences between an isolated atom, nanoparticles and bulk, and most importantly, the oxidation state of the atoms and respective chemical bonds.[142] Well-known examples are metal oxides, whose binding energy is, in comparison with respective metals, larger by several eV.[140] This is caused by redistribution of electron density and, consequently, lower screening of the nucleus. The typical changes of binding energy caused by chemical bonding are tabulated,[143] allowing a detailed analysis of the sample's chemical state. From final state effects, it might be a relaxation of the electronic structure or correlation energy. Firstly, the emitted electron leaves behind a hole, which leads to relaxation of the electronic structure, and subsequently to an apparent decrease of the photoelectron binding energy.[140] This effect might be partially compensated by correlation energy, which, increases the binding energy.[144]

Apart from that, there are effects causing an appearance of additional peaks in XPS spectra. Firstly, the atom may end up after the photoionization in an excited final state, i.e., due to an excitation of a valence electron to an unoccupied state.[145] The kinetic energy of the ionized photoelectron is lowered by the energy required for the excitation. These electrons effectively appear in the spectra as an additional peak, a so-called shake-up satellite, with higher binding energy and lower intensity with respect to the main peak.[138] Secondly, the emitted photoelectron may loose energy by plasmon excitation. This process also results in additional peak appearing in the spectra at higher binding energy.

The peaks mentioned above originate from photoelectrons. Apart from them, there are peaks in XPS spectra related to Auger electrons. They result from a three-electron process during the relaxation of a photoionized atom (Figure 2.4b). An electron from an outer shell fills the hole at the core level formed during the photoionization during the relaxation. The energy released during this process is sufficient to ionize an additional electron from an outer shell. Therefore, the energy of the Auger electron is fully independent of the photon energy and depends only on the energy levels of the three electrons involved in the Auger process.[146]

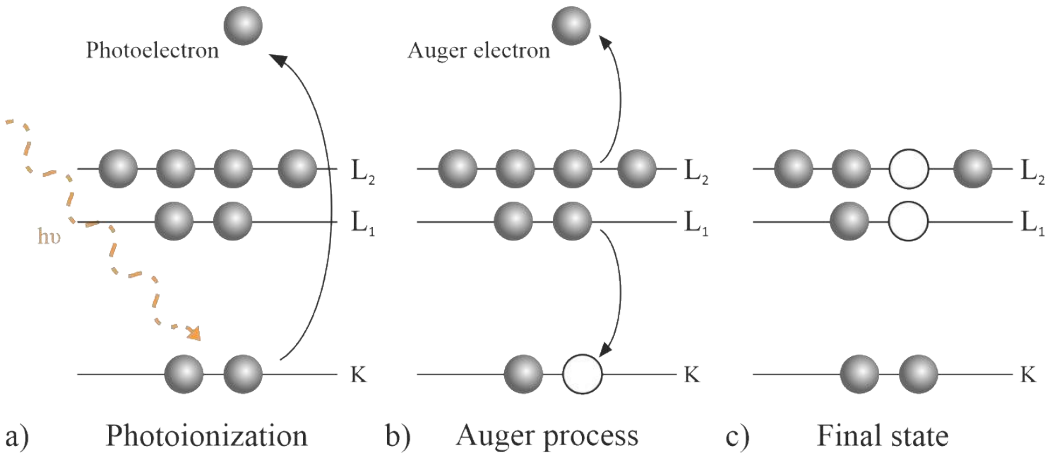

Figure 2. 5: Visualization of KL_1L_2 Auger process. a) During the photoionization, an electron is emitted from K-shell, leaving behind a hole. b) An electron from L_1-shell fills the hole in K-shell. The energy released during this transition is sufficient to ionize an electron from L_2-shell. c) In the final state, the atom is two times ionized. The core shell (K) is fully occupied, and two electrons from outer shells (L_1 and L_2) are missing.

The advantage of XPS is its high surface sensitivity. A photoelectron has to leave the material without energy losses to contribute to a useful XPS signal. Assuming that electron's energy losses are caused only by inelastic scattering, the intensity of the signal I is exponentially decaying with the depth d according to Lambert-Beer law[138]

$$I_d = I_0 e^{-\frac{d}{\lambda \sin\theta}},$$

(2. 7)

λ is the inelastic mean free path (IMFP) of the electron with given energy in the given material, and θ is the take-off angle with respect to the surface plane. IMFP of an electron with an energy of hundreds eV varies for most of the materials in the range of Angstroms up to tens of Angstroms[147] Therefore, more than 95% of the signal is coming from the depth $d < 10\,nm$ for $\theta = 90°$. By measuring at near-grazing collection angle, the surface sensitivity increases to a few atomic layers.

The source of photons plays a crucial role in the application of photoelectron spectroscopy. The most common are conventional X-ray sources (Al Kα, Mg Kα) for laboratory XPS. Another possibility is the usage of a synchrotron radiation (Synchrotron Radiation Photoelectron Spectroscopy, SRPES). Synchrotron radiation offers several advantages in comparison with laboratory X-ray sources. Firstly, the photon beam is more monochromatic, resulting in a much-improved resolution and sensitivity. Furthermore, it is the tunability of the photon energy allowing, i.e., measuring valence bands using low-energy radiation in the

ultra-violet region (Ultra-violet photoelectron spectroscopy, UPS),[148] highly resolved determination of the oxidation state of Ce and Co ions in the corresponding oxides via resonant photoemission spectroscopy (RPES)[149,150] or depth profiling by measuring series of spectra with different photon energy.[151]

In RPES, we benefit from a resonance between the standard photoionization and Auger process. Resonance behaviour causes significant changes in the spectral features of the valence band region.[152] This method was successfully implemented for determining oxidation state of transition metal oxides.[48,149,153]

The kinetic energy of emitted photoelectron for a given material depends on the photon energy (Eq. 2.6). In addition, the kinetic energy of electron determines its inelastic mean free path in the material. Thus, using small photon energies results in high surface sensitivity, since the information depth grows with increasing photon energy. Therefore, tuning the photon energy in the range from tens eV to hunderds eV can be used for a non-destructive depth profiling.

2.3. Electrochemical infrared reflection absorption spectroscopy

The second spectroscopic method used in this thesis is infrared reflection absorption spectroscopy (IRRAS). IRRAS is highly sensitive to molecular structure and orientation providing information about adsorbates, adsorption sites, binding motifs and chemical interactions on the surface. The principle of this method is based on an interaction of infrared (IR) light with solvated or adsorbed molecules and absorption of this light due to vibrational excitations of the molecules.[154] The interaction is described by quantum theory, which yields several conditions for vibrational excitation. According to time-dependent perturbation theory, the probability p of vibrational excitation from an initial state ψ_i to a final state ψ_f is[155]

$$p \propto \left|\langle \psi_i | \boldsymbol{\mu} \cdot \boldsymbol{E} | \psi_f \rangle\right|^2, \tag{2. 8}$$

where $\boldsymbol{\mu}$ is the molecule's dipole moment and $\boldsymbol{E}$ is the electric field of the incident light. The Eq. 2.8 gives the first condition, which is a non-zero dipole moment of the molecule. Therefore, nonpolar molecules (e.g. O_2, N_2) are IR inactive. The second condition also refers to Eq. 2.8. We may expand $\boldsymbol{\mu}$ into Taylor series together with the fact that wavefunctions ψ_n form an orthogonal basis. This show, that only such vibrational excitations, when vibrational

quantum number υ changes by ± 1, are allowed in the first approximation.[156,157] The vibrational excitations with $\Delta\upsilon > \pm 1$ are related to higher terms of the Taylor expansion. Thus, the intensities of corresponding IRRAS peaks are very low.

Apart from the above-mentioned conditions originating from the absorption properties of molecules, there is an additional rule – the metal-surface selection rule (MSSR)[158] – related to the experimental configuration. In the conventional IRRAS setup, the IR beam is reflected by a metal surface and has to pass the layer of adsorbates. Let's assume an adsorbed molecule with non-zero dipole moment. The molecule's dipole moment induces a reorganization of charge density in the metal forming a charge image to compensate an electric field in the metal (Figure 2.6a).[159] If the dipole moment is parallel to the surface, the dipole moment of charge image has an opposite orientation. Therefore, the overall dipole moment is zero, and, due to Eq. 2.7, the molecule is IR inactive. On the other hand, the dipole moment of perpendicularly oriented molecule and its charge image have the same orientation, which effectively increases the absorption peak intensity I.[160] In general, this is expressed by following equation[157]

$$I \propto |2\mu \cos\theta|^2, \tag{2. 9}$$

where θ is the angle between molecule dipole moment and surface normal. The same is also valid also for molecules adsorbed on thin oxide layers on metal substrates.[161] In conclusion, only molecules with non-zero component of dipole moment perpendicular to the surface are IR active.

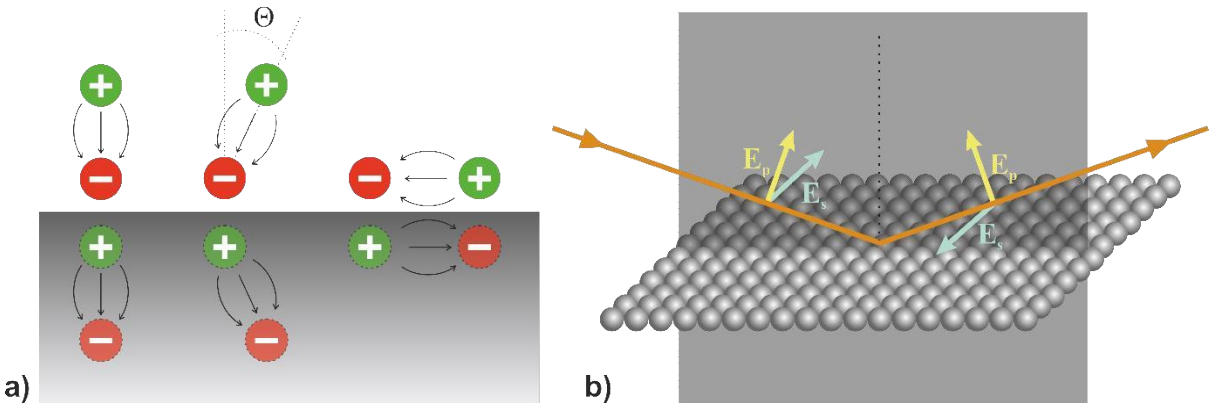

Figure 2. 6: a) MSSR - dipole momentum of an adsorbed molecule and its charge image in the metal substrate b) p- and s- component of electric field of IR beam

Furthermore, the IR beam is polarized, so that the vector of electric field of p-polarized light is parallel with the plane of incidence and the vector of electric field of s-polarized light is perpendicular to the plane of incidence, and, thus, it is parallel with the metal surface (see Figure 2.6b). In the previous paragraph, it was showed that the component of the overall dipole momentum parallel with the metal surface is zero and only the perpendicular component remains. Based on this, the dot product in Eq. 2.7 is zero for s-polarized light. Therefore, the adsorbed species can be detected only by p-polarized light.[162]

IRRAS was originally developed for UHV measurements. However, Bewick et al. proved that it can be used also in the electrochemical environment (Electrochemical Infrared Reflection Absorption Spectroscopy, EC-IRRAS).[163,164]

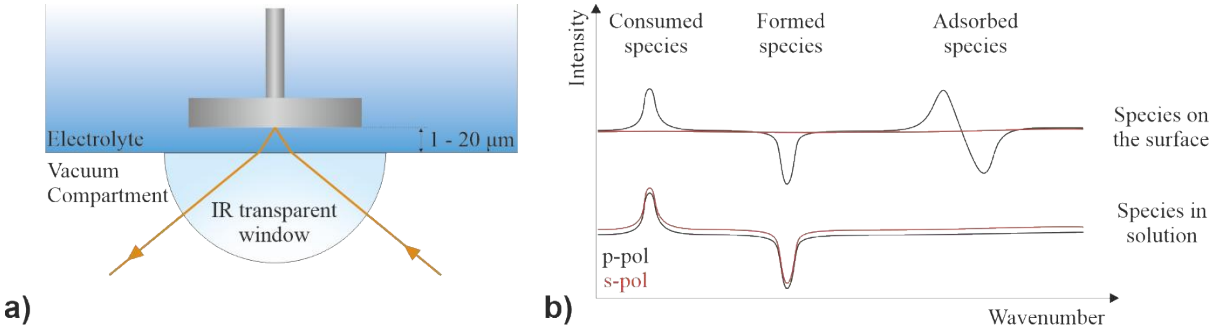

Figure 2. 7: a) Thin layer configuration of EC-IRRAS setup b) Interpretation of bands in EC-IRRAS spectrum – positive bands (facing up) correspond to species consumed during the process, negative bands (facing down) to formed species and s-shape bands to adsorbed species

EC-IRRAS setup consists of two parts – vacuum compartment with a spectrometer, optics and a detector, and electrochemical (EC) cell with electrolyte, where the sample is placed. Both parts are separated by an IR transparent window. This configuration allows in-situ spectroelectrochemical IR measurement at solid-liquid interface. The crucial condition for avoiding total absorption is a thin layer configuration (Figure 2.7a). A typical distance between the sample and the IR transparent window varies from 1 µm to 20 µm.[163–165] Therefore, this volume is diffusionally decoupled from the rest of the electrolyte, which causes several consequences. Firstly, the mass transport between the thin layer and the rest of the electrolyte is limited. Thus, pH and concetrations may change during the measurement compared to the rest of the electrolyte.[166] Secondly, the resistance of the thin layer is high. However, this can be partially compensated by sufficiently high concentration of the supporting electrolyte.[167]

To minimize the effect of electrolyte absorption on the spectra, a potential-difference method is used. In this method, a normalized difference between spectrum R and a reference spectrum R_0 measured at a given potential is plotted[165]

$$\frac{\Delta R}{R} = \frac{R - R_0}{R}.$$

(2. 10)

Therefore, only changes – produced, consumed or adsorbed species – appear in the spectra. More specifically, a loss of absorbing species results in an increase of signal measured by detector and vice versa. Thus, positive bands correspond to consumed species and negative bands to produced species. In the case of adsorbed species, the band position changes with applied potential due to shifting of vibrational frequency with changes in external electric field, so called Stark effect, which results in s-shape bands (Figure 2.7b).[168] Furthermore, we can obtain an additional information by comparing p-polarized and s-polarized spectra. Due to the MSSR, adsorbed species can be detected only with p-polarized light, while species in solution are detectible with both p- and s- polarized light. This allows us to distinguish between species adsorbed at the surface and species dissolved in the solution.[169]

3. Experimental

This thesis focuses on the study of heterogenous model metal and metal-oxide catalysts. The work was done in cooperation between the Depertment of Surface and Plasma Science at Charles University (CU) in Prague (group of doc. Mgr. Josef Mysliveček, Ph.D.) and the Department of Physical Chemistry at the Friedrich-Alexander University (FAU) Erlangen-Nürnberg (group of Prof. Dr. Jörg Libuda). Thanks to this cooparation, I was able to combine methods of surface science - STM, XPS, Low Energy Electron Diffraction (LEED) - and electrochemical methods – EC-IRRAS, and Cyclic Voltammetry (CV). Furthermore, some experiments were carried out at Material Science Beamline (MSB) at Elettra-Sinchrotrone Trieste, Italy. The employed surface science apparatuses in all laboratories were equipped with controlled transfer between UHV chamber and an electrochemical cell for EC-IRRAS or CV measurements.

3.1. Experimental setup at CU

The main focus of the experimental work at CU was on preparation and characterization of well-defined model metal-oxide catalysts. Characterization included space-averaging methods of surface science (XPS, LEED) and a microscopic technique (STM). All methods are integrated in one UHV system, including the transfer of model catalyst samples between the UHV chamber and an electrochemical cell.

3.1.1. UHV Chamber

The UHV system (Figure 3.1) consists of three chambers – main chamber, STM chamber, and a load-lock chamber. All chambers are connected with transfer rods. Furthermore, an electrochemical cell can be connected to a load-lock chamber allowing transfer of a sample from UHV to electrolyte without exposure to ambient atmosphere. The scheme of the whole system is shown in Figure 3.1a.

The main chamber is pumped with a turbomolecular pump (TMP, Pfeiffer, TMU 521 Y P) as a secondary pump and a scroll pump (SP, Anest Iwata, ISP-250C) as a primary pump. Additionally, there is an ion getter pump (IP, Delong Instruments, ISP 04) installed. The base pressure in the main chamber is reaching 10^{-10} mbar. The chamber enables the preparation and the chemical analysis of the sample. Therefore, it is equipped with a gas dosing system with variable leak valves (Duniway Stockroom, Model 1000), a wide-range ion gun (Specs,

IQE-11-A), a focused ion gun (Specs, PU/IQE 12/38), a single electron-beam evaporator (Tectra), a dual electron-beam evaporator (Tectra), a quadrupole mass spectrometer (QMS, Pfeiffer Prisma Plus), and laboratory XPS with X-ray source (Specs, XRC 1000), water cooling system Specs, CCX 60) and hemispherical analyzer (Specs Phoibos 150) with a multi-channel detector.

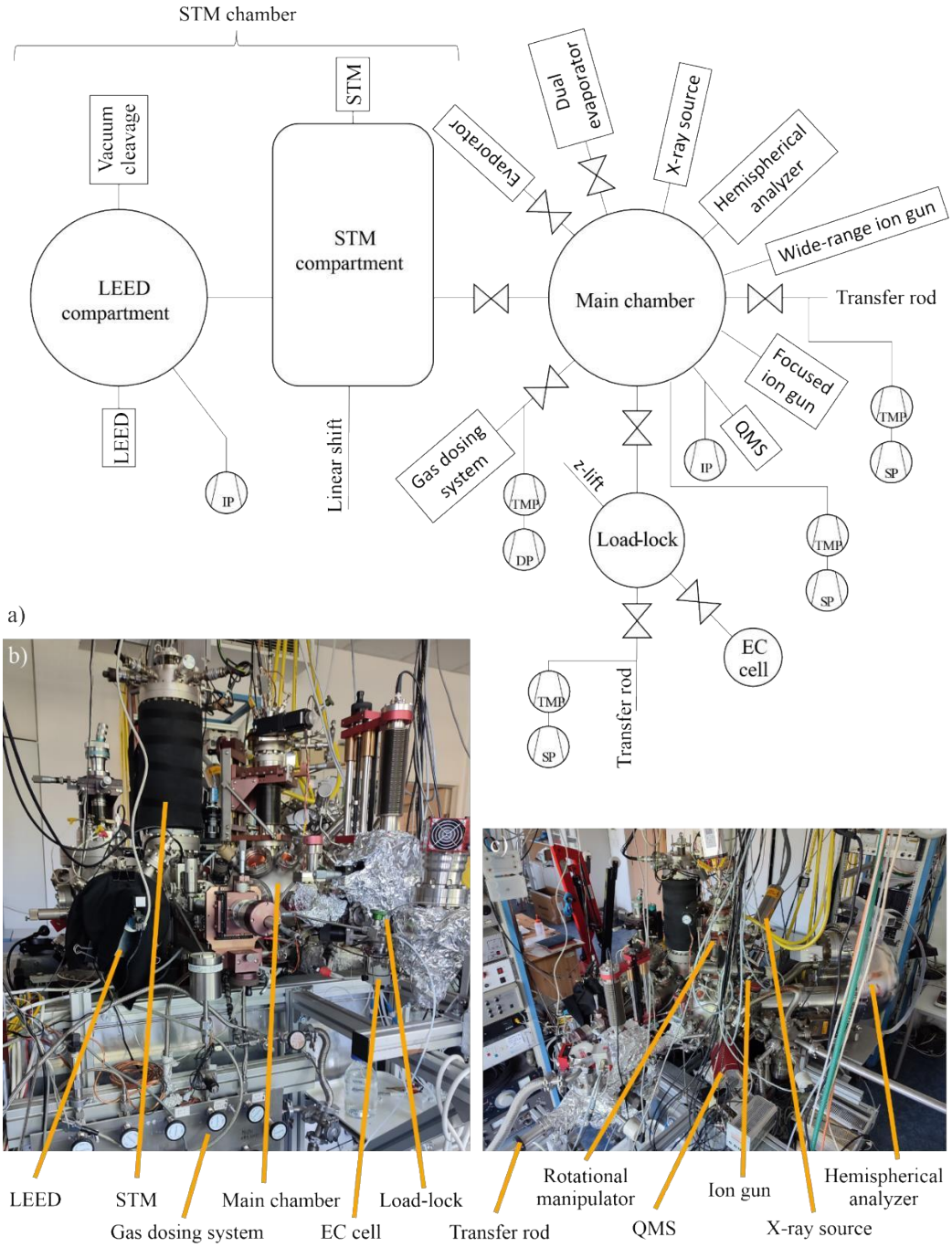

Figure 3. 1: a) Simplified schematic drawing of UHV system at CU (TMP – Turbomolecular pump, SP – Scroll pump, DP – Diaphragm pump, IP – Ion pump). b) – c) Photos of the UHV system

The sample is mounted on a rotational manipulator (Figure 3.2) with four degrees of freedom ($x, y, z,$ and ϑ) and a LN_2-cryostat. A quartz crystal microbalance (QCM, Inficon, gold coated crystal, 750-1000-G10) with a thickness meter (Tectra) is mounted on the manipulator in the proximity of the sample allowing direct control of the amount of deposited material during the deposition. The sample holder provides a radiative sample heating with an automatic PID regulated temperature control in the range of 90-1350 K.

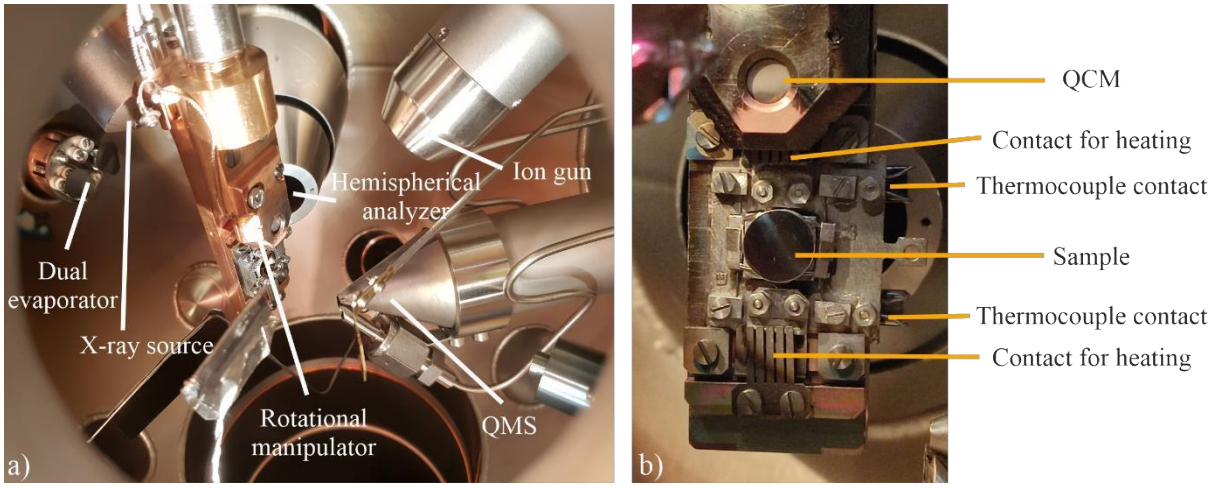

Figure 3. 2: The main chamber. a) Inside of the chamber with rotational manipulator (photo: Mgr. F. Lavický) b) Detail of the manipulator

The STM chamber consists of two compartments – one for STM and one for LEED. The whole chamber is pumped through the gate valve with the TMP in the main chamber. Afterwards, the vacuum is maintained with the IP (Perkin-Elmer) reaching a base pressure of 10^{-11} mbar. More details about STM compartment is in Section 3.1.3. Similarly to the main chamber the LEED compartment is equipped with a rotational manipulator with five degrees of freedom. The LEED itself uses a ErLEED 1000 A optics (SPECS). The diffraction pattern is recorded by a CCD camera (ImagingSource DMK 33GX174). The system also allows to record the screen current required for iv-LEED. Apart from that, the chamber is equipped with a home-built system to prepare clean surfaces by cleaving the sample mechanically in vacuum.

All chambers are separated by gate valves (MDC Vacuum Products, GV-1500; VAT, Series 01). The transfer of the sample between the chambers is carried out by two perpendicularly oriented linear transfer rods (Thermionics FLLRE-.275-50-36). Furthermore, the load-lock chamber is equipped with a vertical lift, which enables to transfer the sample into an electrochemical (EC) cell. The EC cell is an adapted version of the EC cell designed by Dr. Brummel used at MSB (more details in Section 3.3).[66]

3.1.2. Scanning tunneling microscopy

An important step in heterogenous model catalystic studies is the determination of morphological parameters of the catalysts, such as nanoparticle coverage, substrate step density or the size and shape of nanoparticles. STM is a suitable tool to determine the surface morphology of metals or thin oxide layers on metals. In this thesis, a home-built STM equipped with a commercial STM measuring head (CreaTec GmbH) (Figure 3.4a), a LN_2 cooled cryostat and a home-built control unit was used. STM images were acquired with home-written software and analyzed using the Gwyddion software .[170] Two types of STM tips were prepared for the measurement - electrochemically etched W tips and mechanically cut PtIr tips. In both cases the tips were sputtered and annealed in vacuum before use.

A high stability of the tunneling junction is essential to obtain well-resolved STM images. Therefore, the changes in tip-sample distance shouldn't be higher than tenths of angtrom. This requires a good shielding of mechanical and acoustic vibrations. To reach this, the whole UHV system is mounted on pneumatic vibration isolator (Newport I-2000 series) shielding frequencies higher than 1 Hz. In the second step, the STM table is in the UHV chamber hanging on three springs filtering the low frequencies.

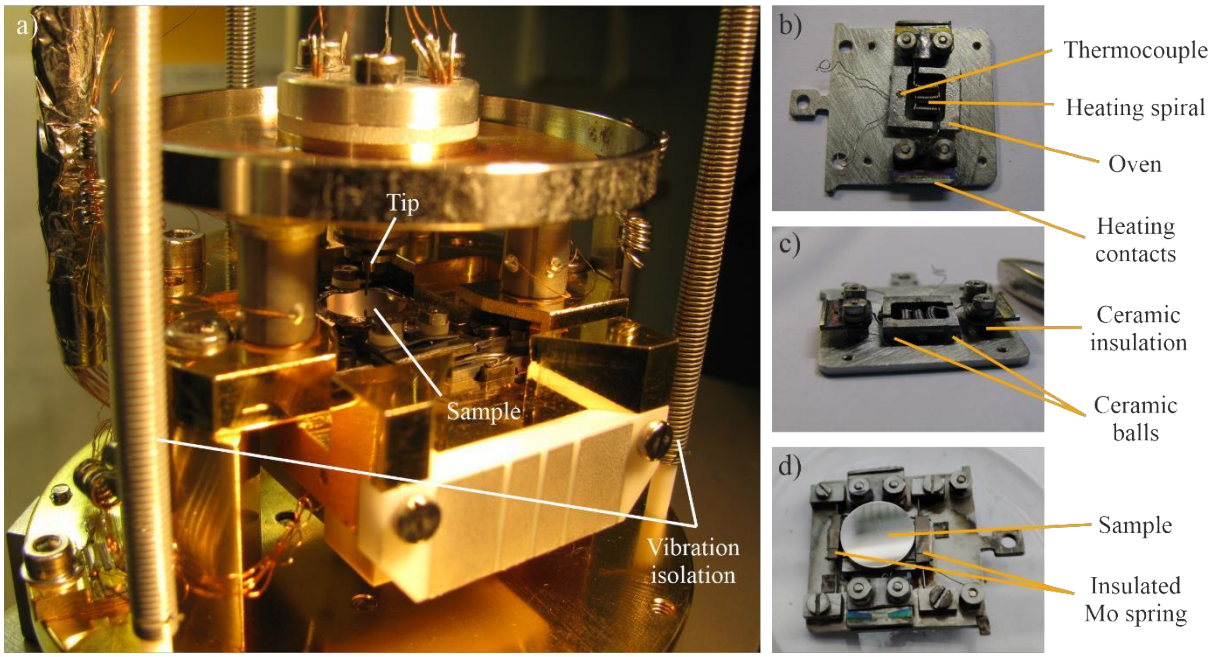

Figure 3. 3: a) STM table (photo: doc. J. Mysliveček) b) – c) Partially disassembled sample holder with the oven and heating spiral d) complete sample holder

Another component affecting the stability of the tunneling junction is the sample holder. There are several requirements for sample holder's properties originating in the used

preparation and characterization methods. The sample holder contains a small oven, on which the sample is placed, providing radiative heating. A thermocouple is installed in the proximity of the sample. The sample with the thermocouple, heating system and the sample holder, which is in the contact with the UHV chamber, is electrically separated from each other. The sample holder has to fulfill the high level of mechanical stability required for the STM measurements. Apart from that, all used materials have to be compatible with UHV and with high temperatures. Photo of the sample holder is shown in Figure 3.3 b-d. The oven with the sample is placed on three isolating ceramic balls and pressed against the sample holder with a insulated W spring providing the mechanical stability. The thermocouple wires are connected to the wall of the oven touching the bottom of the sample. At the same time, the thermocouple serves as an electrical connection to the sample in STM.

3.2. Experimental setup at FAU

Major part of the work done at FAU was focusing on the *in-situ* study of adsorbates and chemical reactions at metal or metal-oxide model catalysts using EC-IRRAS. The samples were prepared either in an UHV chamber and then transferred into electrochemical cell (oxide thin films) or by flame annealing or induction heating (metal single-crystals).

3.2.1. Electrochemical infrared reflection absorption spectroscopy

All measurements were done at EC-IRRAS setup containing a vacuum based Fourier transformed infrared (FTIR) spectrometer with optics (Bruker Vertex 80v) controlled with OPUS software and LN_2 cooled narrow band mercury-cadmium-telluride (MCT) detector (Figure 3.4a). [171] The sample compartment is equipped with an automatized polarizer (KRS-5) and gold mirrors bending the IR beam to and from the EC cell providing the incident angle of $60° \pm 5°$ and $30° \pm 5°$. The sample compartment and the EC cell are separated with a hemispherical IR transparent window with a diameter of 25 mm. The window material is chosen based on the required interval of transmitted wavelengths: CaF_2 (Korth, >1100 cm^{-1}) or ZnSe (Korth, >600 cm^{-1}).

The EC cell consists of PTFE housing and PTFE lid (Figure 3.4b,c). To avoid leaking of electrolyte from the cell to the evacuated spectrometer, the EC cell is sealed with Kalrez gasket. The lid contains several inlet and outlet holes. Namely, two inlets for gas line – one for purging the electrolyte with Ar, and second one for establishing protective atmosphere above the electrolyte, one gas outlet and three inlets for electrodes – the working electrode,

the counter electrode and the reference electrode (Figure 3.4d). The potential is controlled by a commercial potentiostat (Gamry 600) operated by Gamry Framework software. The sample, which is the working electrode, was connected with a Pt wire mounted in a glass

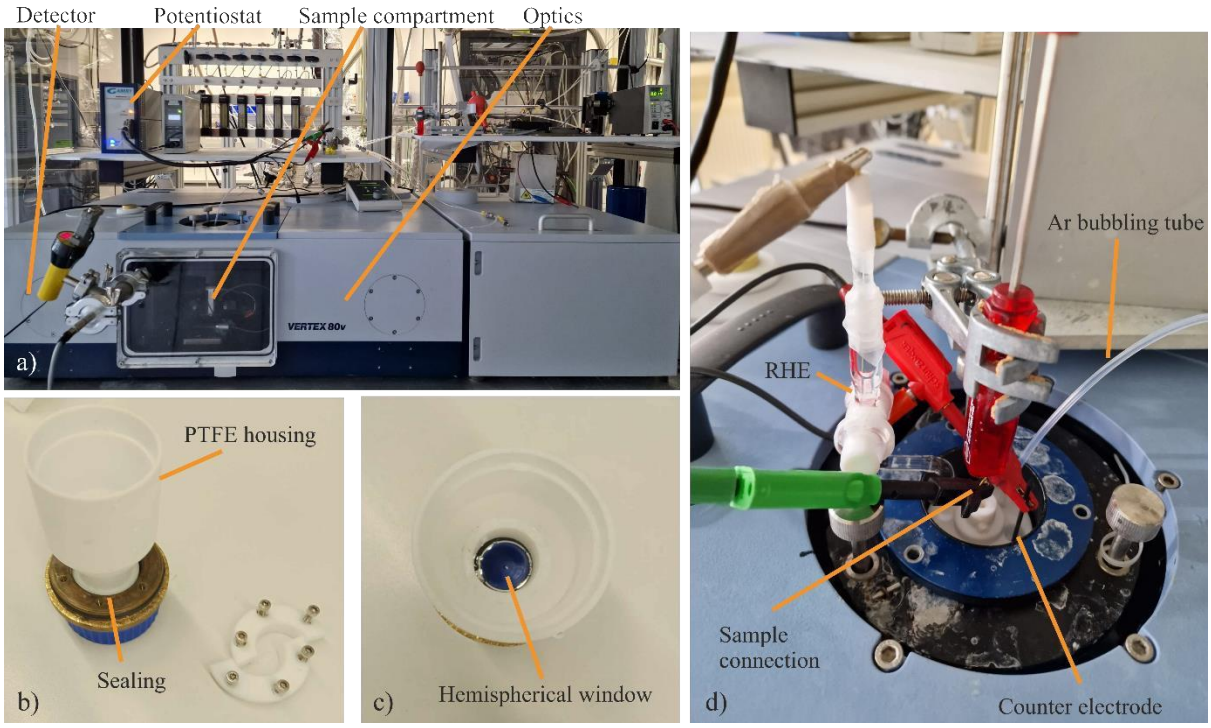

Figure 3. 4: EC-IRRAS setup. a) IR spectrometer b – c) EC cell with IR transparent hemisperical window d) lid of EC cell with electrode connections (Photo: Z. Hussain, P. Kumar Samal)

tube. The Pt wire or Au wire (Hauner, 99.999%) were used as a counter electrode, and a Ag/AgCl (RE-1B, ALS Co.) or a home-built reversible hydrogen electrode (RHE) as reference electrode. The potentials $E_{Ag/AgCl}$ referenced to Ag/AgCl were converted to potentialsE_{RHE} referenced to RHE as follows:

$$E_{RHE} = E_{Ag/AgCl} + E_0 + 0.059 \cdot pH, \tag{3. 1}$$

with $E_0 = 0.195\ V$ at $25°C$.

The reference spectra were measured by attenuated total reflection (ATR) IR spectroscopy using a Ge ATR window (Bruker) in the EC-IRRAS spectrometer. The measured ATR spectra were compared with a spectra calculated by DFT to assign individual bands to corresponding vibrational modes.

3.2.2. Cleaning procedure and sample preparation

EC-IRRAS allows elecgtrochemical in-situ measurements with model catalysts. However, to maintain the high-level of control, ultra-clean conditions are required. Therefore, a thorough cleaning procedure was followed.

All glassware, Teflon parts, and metal wires are stored in a bath of concentrated sulfuric acid (Merck, EMSURE®, 98%) with NoChromix (Sigma Aldrich) for at least 12 h. Before the measurement, all parts were rinsed three times with ultra-pure water (MilliQ synergy UV, 18.2 MΩ at 25°C) and subsequently boiled in ultra-pure water for 30 min. The rinsing-boiling cycle was repeated three times. At the end, all parts were rinsed again three times with ultra-pure water. Additionally, all wires were annealed in the flame of a Bunsen burner and rinse them with ultra-pure water.

The Pt(111) single-crystal (MaTecK) catalyst was prepared by annealing in the flame of Bunsen burner and subsequent cooling down in a protective Ar/H_2 atmosphere (ratio 3:1). All contaminations are removed during the annealing step and the temperature is sufficient to recover surface's crystallographic structure. Cooling down in Ar/H_2 atmosphere prevents oxidation of the surface. After cooling down, the sample was dipped into ultra-pure water to form a protective layer and transferred into EC-cell.

$Co_3O_4(111)$ thin layer catalysts supported on Ir(100) were prepared in a UHV chamber with a base pressure of 10^{-10} mbar. The chamber was equipped with an ion gun (Specs, IQE 11/35), an evaporator (Focus EFM 3), a gas dosing system, a LEED (Specs, ErLEED 150), and a quadrupole mass spectrometer (Hiden Analytical). Heating was provided by electron bombardment to the back side of the sample. The preparation procedure follows the recipe of Heinz and Hammer.[115–117] The details about the preparation are provided in Section 3.4. After the preparation, the sample is transferred to EC cell using a special transfer cell developped at the chair of Interface Research and Catalysis at FAU.[63] The schematic drawing of their design is shown in Figure 3.5. The transfer cell can be filled with ultra-pure water or electrolyte protecting the sample during the transfer. Before inserting the sample and during the transfer, the cell is purged with a constant flow of N_2 (Linde, 5.0).

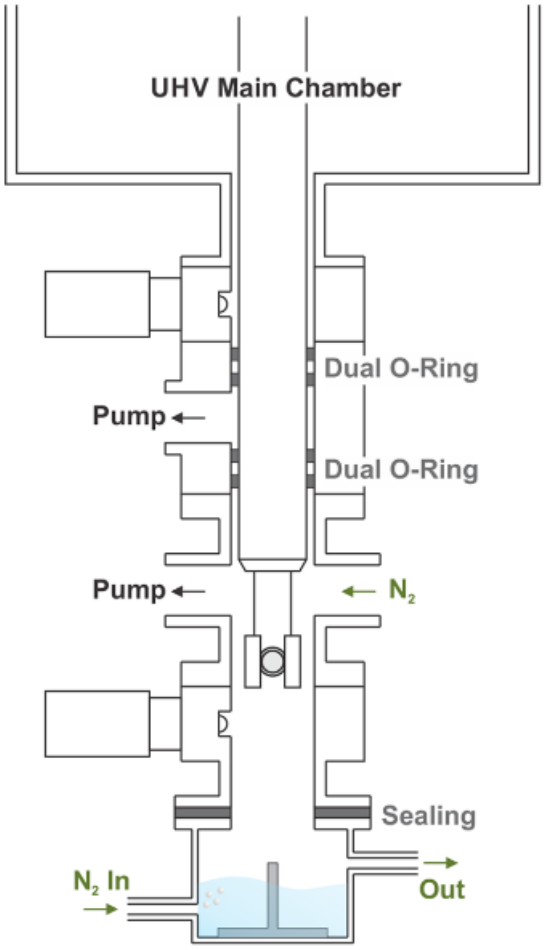

Figure 3. 5: Schematic drawing of UHV-EC cell transfer system (adapted from ref. 58)

3.3. Material Science Beamline

MSB allows to perform SRPES measurement with high energy resolution and tunable photon energy. The beamline uses a radiation from a bending magnet of the Elettra storage ring. Prior to entering the MSB end station, the polychromatic photon beam passes through several focusing mirrors and a plane grating monochromator (SX-700) resulting in a focused monochromatic beam with a tunable photon energy in a range of 22 eV – 1000 eV. A gold mesh measuring the photon flux is mounted on the entrance to the end station.

The end station consists of five UHV chambers – an analysis chamber, two preparation chambers, a load-lock chamber and an electrochemistry chamber. In the matter of briefness, only short description of analysis chamber and electrochemistry chamber is given bellow. The full description of the MSB can be found at their online beamline overview.[172]

The analysis chamber reaches a base pressure of $1 \cdot 10^{-10}$ mbar and is equipped with three evaporators (Tectra e-beam), an ion gun (Varian 981-2043), a gass dosing system, a QMS

(Pfeiffer Prisma QMS200), a LEED optics (OCI BDL800IR-LMX-ISH), and a hemispherical analyzer (Specs Phoibos 150) with a multi-channel detector (1D-DLD). Additionally, the chamber is equipped with a conventional laboratory X-ray source (Specs XR50) for better comparability of the obtained spectra with XPS spectra measured with lab sources. The analysis chamber is separated from the preparation chamber with a gate valve (Thermionics PFB-G-2500H).

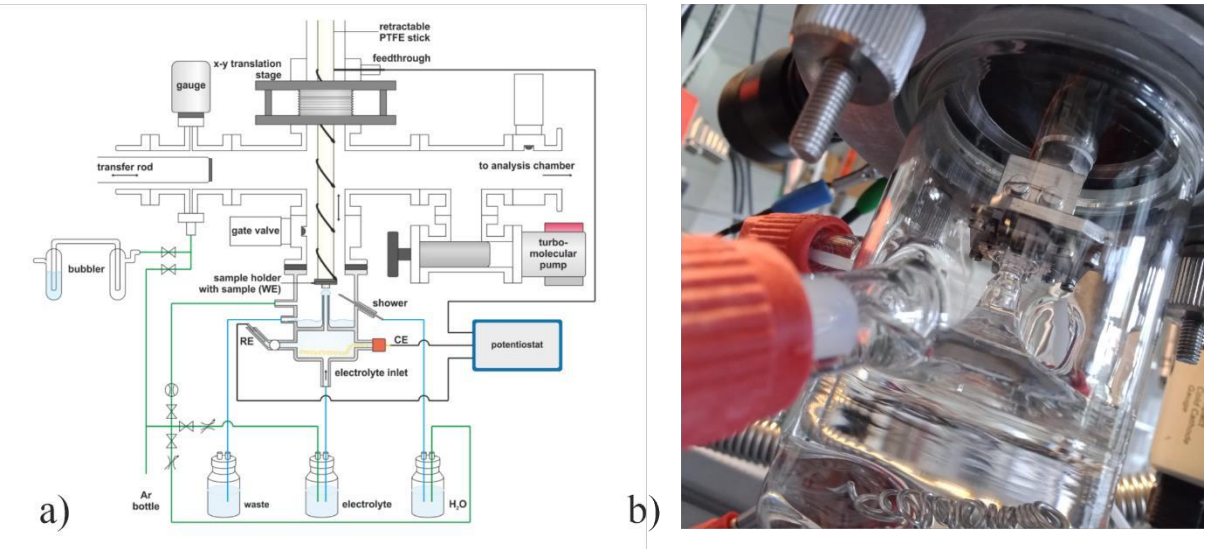

Figure 3. 6: a) Schematic drawing of the EC cell (adapted from ref. 66) b) Photo of the sample in the EC cell in the contact with the electrolyte – hanging meniscus configuration (Photo: P. K. Samal)

The sample can be transferred from the analysis chamber to the electrochemistry chamber under UHV conditions. The electrochemistry chamber is connected to a glass EC cell via a gate valve. The schematic of the electrochemistry chamber and the EC cell is illustrated in Figure 3.6. The EC cell is divided into two compartments. The bottom one is filled with electrolyte and contains inlets for reference electrode (Ag/AgCl, RE-1B, ALS) and counter electrode (Au wire, Hauner, 99.999%). The electrolyte flows through a thin capillary to the upper compartment by Ar overpressure forming a droplet at the top of the capillary. The upper compartment features one gas inlet, one inlet with ultra-pure water (shower) allowing to rinse the sample after the experiment, and a waste outlet. This setup allows to perform ex-situ emersion SRPES measurements. Prior to the measurement, the electrolyte and the EC-cell are purged with Ar, and the upper part of the EC-cell and the electrochemistry chamber are filled with Ar. Afterwards, the gate valve is opened and small Ar overpressure in the electrolyte reservoir pushing the electrolyte through the capillary is used to form a stable electrolyte droplet. In the last step, the sample approaches the droplet at the top of the

capillary forming a hanging meniscus configuration (Figure 3.6b) while the potential is controlled. After the measurement (approx. 1 – 10 min) the sample is rinsed with ultra-pure water, retracted back to the electrochemistry chamber, pumped down and transferred to the analysis chamber for SRPES measurement.

3.4. Sample preparation

An important part of the experimental procedures in the Prague laboratory was preparation of metal-oxide catalysts. The focus was on transition metal oxides, namely Pt and Pd nanoparticles on cobalt oxide and cerium oxide nanoparticles on Pt(111). Both oxides can exist in several possible phases with different oxidation states. Therefore, a precise preparation procedure is crucial for the final structure and stoichiometry. [100,116,117,173]

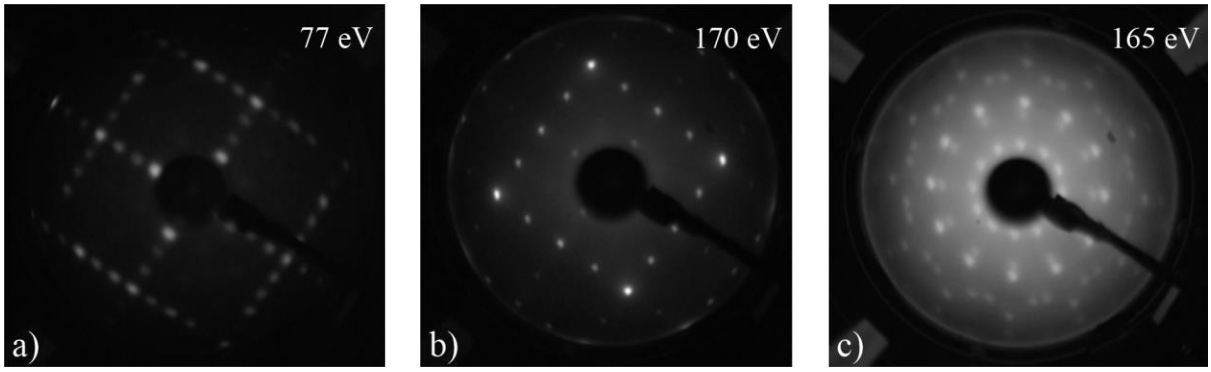

Figure 3. 7: LEED patterns of preparation of Co_3O_4(111)/Ir(100) thin film. a) Ir(100)-(5x1) b) Ir(100)-O-(2x1) c) spinel structure of Co_3O_4(111)

Cobalt oxide exists in two structures – a rocksalt CoO and a spinel Co_3O_4. This work focuses on the latter. The samples were prepared following a preparation procedure described by Heinz and Hammer.[115] Ir(100) single-crystal (MaTecK) serving as a substrate was cleaned by cycles of Ar^+ (Argon 6.0, Linde) sputtering and annealing to 1330 K resulting in a Ir(100)-(5×1) reconstruction. Afterwards, the Ir(100)-(5×1) was annealed to 1270 K in oxygen atmosphere (Linde 5.0, $5 \cdot 10^{-7}$ mbar) to create a Ir(100)-O-2×1 superstructure. All structures during the preparation procedure were checked by LEED (Figure 3.7). Cobalt (Alfa Aesar, 99.995%) was deposited by physical vapor deposition (PVD) from electron-heated Co rod in reactive oxygen atmosphere ($1.5 \cdot 10^{-6}$ mbar) for approx. 15 min. The Ir substrate was kept at room temperature during the deposition. Prior to deposition, the spatial homogeneity and time stability of the deposition rate were controlled with a QCM. The thickness of Co_3O_4(111) film was determined with the QCM using Sauerbrey‘s approximation[174]

$$\Delta f = -\frac{2f_0^2}{A\sqrt{\rho_q \mu_q}}\Delta m,$$

(3. 2)

where Δf stands for the change of frequency, f_0 the quartz resonant frequency, A the quartz area, ρ_q the quartz density, μ_q the quartz Shear modulus and Δm is the change of the mass corresponding to the amount of deposited material. The typical thickness of the film varied between 5 – 6 nm, which is above the critical thickness, bellow which the spinel $Co_3O_4(111)$ is unstable.[117] After the deposition the sample was annealed in oxygen atmosphere ($2 \cdot 10^{-6}$ mbar) at 680 K for 60 min and, subsequently, flashed at 720 K in UHV. The obtained spinel structure was verified with LEED (Figure 3.7c) and oxidation state of Co with XPS (Figure 3.8). Furthermore, the thickness d of the $Co_3O_4(111)$ was verified from an attenuation of Ir 4f signal in XPS[48]

$$d = -\lambda \ln \frac{I}{I_0}.$$

(3. 3)

I and I_0 stand for the intensity of Ir 4f signal after and before deposition, respectively, and λ is the inelastic mean free path of the electron with a corresponding kinetic energy in the deposited material. Pt or Pd nanoparticles were deposited on $Co_3O_4(111)$ thin film by PVD from electron-heated wires (Pt: Safina, 1 mm, 99.99%; Pd: Goodfellow, 1 mm, 99.99%). The amount of deposited material was determined from QCM and from the attenuation of the Ir 4f signal in the XPS spectrum.

Similarly, cerium oxide films were prepared by PVD in reactive oxygen atmosphere on Pt(111) following the procedure of Luches et al.[175] Pt(111) single-crystal (MaTecK) was cleaned by cycles of Ar^+ sputtering and annealing. Cerium (Goodfellow, 99,9%) was deposited from an electron-heated Ta crucible in the presence of oxygen ($2 \cdot 10^{-5}$ Pa). The amount of deposited cerium was controlled with the QCM. After the deposition, the sample was annealed in oxygen atmosphere ($2 \cdot 10^{-5}$ Pa). Both, the temperature during the deposition and the annealing temperature strongly affects the final morphology. Further details are provided in Section 4.4.

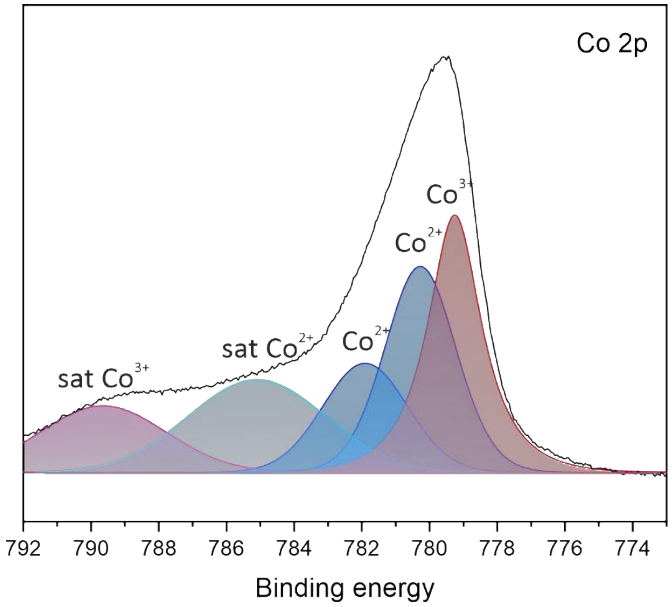

Figure 3. 8: Co 2p XPS spectrum of an as prepared Co_3O_4 film.

4. Results

This thesis focuses on model studies of metal and metal-oxide catalysts applicable in energetically relevant electrochemical reactions. The presented studies address all four aspects of model catalysis – morphology and chemical state of the catalyst, stability of the catalyst, adsorption properties, and reaction pathways – described in Section 1.2. and demonstrate that by using a proper combination of experimental techniques it is possible to answer all of them. The studied catalytical systems vary from metal single-crystal through continuous oxide film to metal-oxide catalyst in both – classical and inverse – geometry covering a wide range of chemical and morphological complexity. Each system addresses specific questions about a particular catalyst.

Firstly, a model study of atomically dispersed Pt catalyst on a $Co_3O_4(111)$ is presented. The study focus on the chemical state of the supported Pt nanoparticles, and their properties and stability under various UHV conditions. Sections 4.2. – 4.4. present a detailed study on the stability and properties of the active metal phase of $Pd/Co_3O_4(111)$ catalyst. Namely, Section 4.2 represent an analogous study to Section 4.1 describing the growth of Pd nanoparticles on $Co_3O_4(111)$ substrate from the initial state of nucleation, the formation of $Pd/Co_3O_4(111)$ interface and the EMSI. In the next step, a thermodynamical stability of these nanoparticles when exposed to oxidizing or humid conditions using near ambient pressure XPS is investigated (Section 4.3.). Finally, Section 4.4 deal with the stability of Pd nanoparticles supported on $Co_3O_4(111)$ and highly oriented pyrolitic graphite (HOPG) in alkaline electrolytes (Section 4.4.).

All so far mentioned studies investigate the metal-oxide catalyst in conventional geometry. Therefore, the main focus lies on the properties and stability of the metal phase. Section 4.5 represents a model study of inverse metal-oxide catalyst, which focuses on the properties and stability of the oxide phase. Namely, it is the stability of CeO_2/Pt catalyst in alkaline electrolyte as a function of applied potential, the size of ceria nanoislands, and the preparation method.

In sections 4.1-4.5 we addressed the first two aspects of model catalysis – morphology and properties of the catalyst and its stability under electrochemical conditions. In Section 4.6, we move on to the third aspect – adsorption properties. Monophosphonatophenyltriphenyl

porphyrin (MPTPP) was anchored to atomically defined $Co_3O_4(111)$ film and its binding motif was identified by EC-IRRAS.

Finally, Section 4.7. addresses the last aspect – the electrocatalytical reaction itself. The dehydrogenation of 1-cyclohexyl ethanol, which may serve as a potential electrochemically active LOHC, is studied using Pt single-crystal catalysts. The electrooxidation products were identified by EC-IRRAS.

4.1. [P1] – Atomistic picture of metal support interaction and role of water

Metal-oxide materials play a key role in various applications in (electro-)catalysis and energy storage.[176] The presented work focuses on the properties of as-prepared Pt nanoparticles supported on a reducible oxide, namely $Co_3O_4(111)$. It consists of a fundamental study of electronic metal support interaction between highly dispersed Pt and a well-ordered $Co_3O_4(111)$ thin film with a focus on the role the most ubiquitous molecules in applications have on the dispersion of Pt nanoparticles on the catalyst surfaces. To reach detailed understanding of processes at atomic level, we combined experimental microscopical (STM) and spectroscopical (SRPES) methods with theoretical DFT calculations. $Co_3O_4(111)$ thin film was prepared by PVD following the procedure described in Section 3.4. 0.02 MLE, 0.04 MLE, and 0.10 MLE of Pt was deposited onto $Co_3O_4(111)$ film. The STM image of the as-prepared $Co_3O_4(111)$ film (Figure 4.1a) reveals well-ordered terraces terminated by Co^{2+} cations with two types of structural features – bright protrusions (marked with yellow circle, hereafter denoted as species I) and dark depressions (marked with blue circle, hereafter denoted as species II).

The species I disappear after deposition of Pt (Figure 4.1b-d), but two additional types of species appear – bright protrusions in registry with $Co_3O_4(111)$ (marked with green circle, hereafter denoted as species III) and triangular shaped large bright protrusions in threefold hollow sites (marked with red circle, hereafter denoted as species IV). Apart from that, larger bright species X were identified at Pt coverages of 0.04 and 0.10 MLE (marked with orange circle), which are assigned to small $Pt^{\delta+}$ aggregates. The overview of observed species is provided in Table 1.

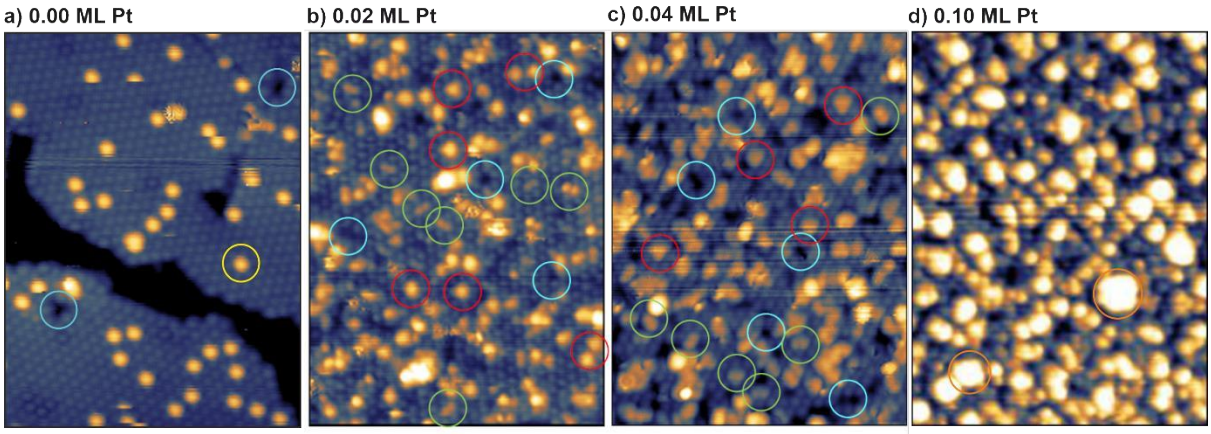

Figure 4.1: STM images a) Co3O4(111) b) 0.02 ML Pt/Co3O4(111) c) 0.04 ML Pt/Co3O4(111) d) 0.13 ML Pt/Co3O4(111). Adapted from ref. 177.

In order to identify the nature of species I-IV, theoretical group of prof. S. Piccinin* simulated STM images of various surface configurations with density functional theory (DFT) using the Tersoff-Hamann approximation. We compared the simulated STM patterns and measured parameters of species I-IV with respect to the position, symmetry, and apparent height. Based on this, we suggest the following interpretation (Figure 4.2). Species I represent a single OH^- group on top of Co^{2+} cation with H^+ on a neighboring oxygen anion. For Species II, DFT calculations suggest that the dark depressions are voids caused by missing surface Co^{2+} cation. The most probable interpretation of species III appearing after Pt deposition is Pt atoms substituting Co^{2+} cations. This interpretation represents also the most energetically favorable configuration of adsorbing Pt single atoms. Finally, species IV are attributed to so called triaqua complexes – Pt atoms in FCC sites decorated by three OH^- groups interacting with three H^+ cations adsorbed on the surrounding oxygen cations.

Table 1: The observed species and their relative density. Adapted from ref. 177.

Pt (MLE)	Species I (nm^{-2})	Species II (nm^{-2})	Species III (nm^{-2})	Species IV (nm^{-2})	Species X (nm^{-2})
0	0.12	0.03	0	0	0.03
0.025	0	0.10	0.08	0.04	0.27
0.04	0	0.35	0.08	0.02	0.28
0.10	0	n.a.	n.a.	n.a.	0.51

* DFT calculations were performed by theoretical group of prof. S. Piccinin from Istituto Officina dei Materiali, Consiglio Nazionale delle Richerche, Trieste

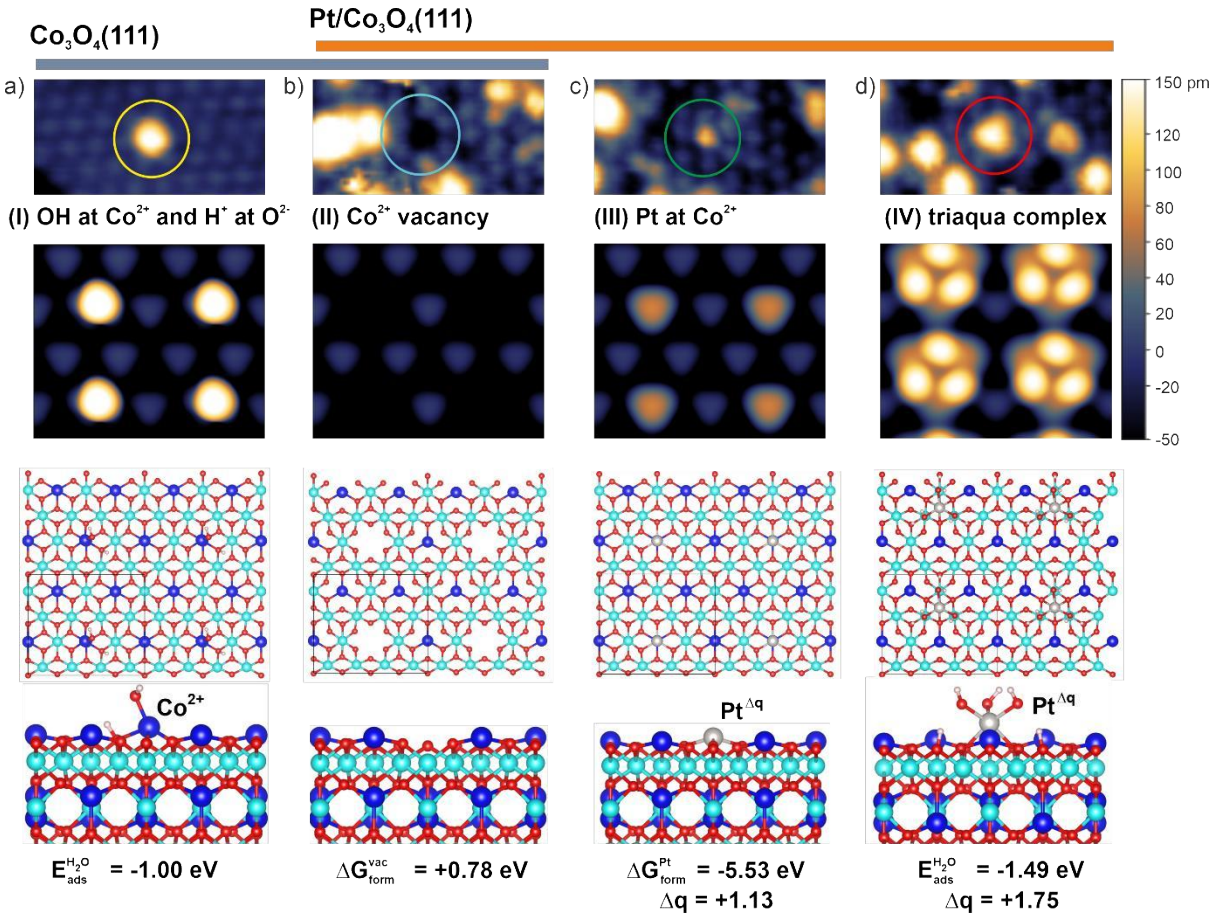

Figure 4.2: Interpretation of species I-IV based on DFT calculations. Adapted from ref. 177.

The Bader charge calculations show that Pt substituing Co^{2+} cation (species III) is in the oxidation state of Pt^{2+}. While formation of triaqua complexes results in Pt in octahedral coordination with the Bader charge corresponding to oxidation state of Pt^{4+}. These calculations are in good agreement with our SRPES measurements (Figure 4.3). After Pt deposition, two doublets in the Pt 4f region appeared. The first doublet at 72.3 eV, can be assigned either to atomically dispersed Pt^{2+} cations or to ultra-small $Pt^{\delta+}$ aggregates. The second doublet at 74.0 eV represents Pt^{4+} species.

The dissapearance of OH^- groups adsorbed on Co^{2+} cations (species I) after Pt deposition is most probably caused by migration of OH^- groups from Co^{2+} sites to Pt sites. Based on the DFT calculations of prof. Piccinin's group, we identified a driving force for this process originating in the difference of adsorption energies. The OH^- group binds most strongly to Pt at the FCC site (-1.51 eV) followed by Pt substituting the surface Co^{2+} cation (-1.24 eV) and Co^{2+} cation (-1.00 eV).

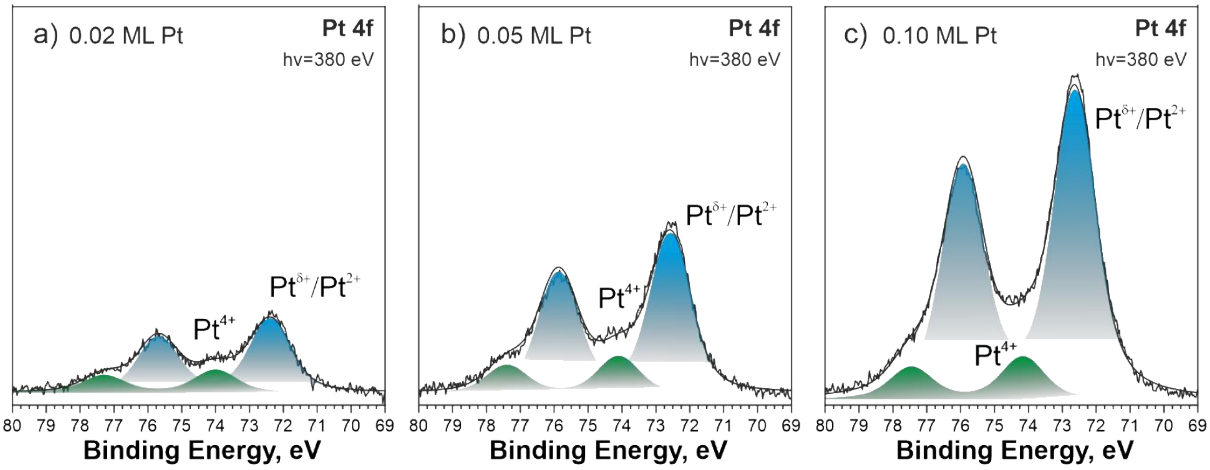

Figure 4.3: SRPES Pd 4f spectra a) 0.02 ML Pt b) 0.04 ML Pt c) 0.10 ML Pt. Adapted from ref. 177.

To further investigate the role of water on the atomic dispersion of Pt, 0.1 MLE of Pt was deposited on three types of $Co_3O_4(111)$ – dehydroxylated, hydroxylated and moist (Figure 4.4). The as-prepared samples predominantly consist of Pt^{2+} substituting Co^{2+} cations, Pt^{4+} triaqua complexes and ultra-small $Pt^{\delta+}$ aggregates. The amount of Pt^{4+} upon deposition is similar for all three samples. Annealing to 350 K lead to formation of triaqua complexes accompanied by increase of Pt^{4+} and decrease of Pt^{2+}/ $Pt^{\delta+}$ signal. This tendency is more pronounced on the moist sample. Water stabilizes Pt at FCC sites or relocate Pt^{2+}/ $Pt^{\delta+}$ to the FCC position forming triaqua complexes. However, after the loss of the hydroxyl group, Pt at the FCC sites are prone to sintering. Therefore, with further annealing, Pt^{4+} species are reduced to Pt^{2+}/ $Pt^{\delta+}$ and further to metallic Pt^0 above 450 K with the highest amount of Pt^0 for the moist sample. Additionally, an increase of Pt^{4+} signal was observed above 600 K. However, in this case it is not related to formation of triaqua complexes. The depth profiling indicates sub-surface subtitution of Co^{3+} cations. DFT shows that this configuration is energetically the most favorable with formation free energy of -6.45 eV.

This work showed the key role of EMSI in morphology and chemical state of small Pt nanoparticles. Atomically dispersed Pt were observed predominantly in the form of Pt^{2+} and Pt^{4+}. Additionally, the stabilizing effect of water to Pt^{4+} and the formation of triaqua complexes was demonstrated.

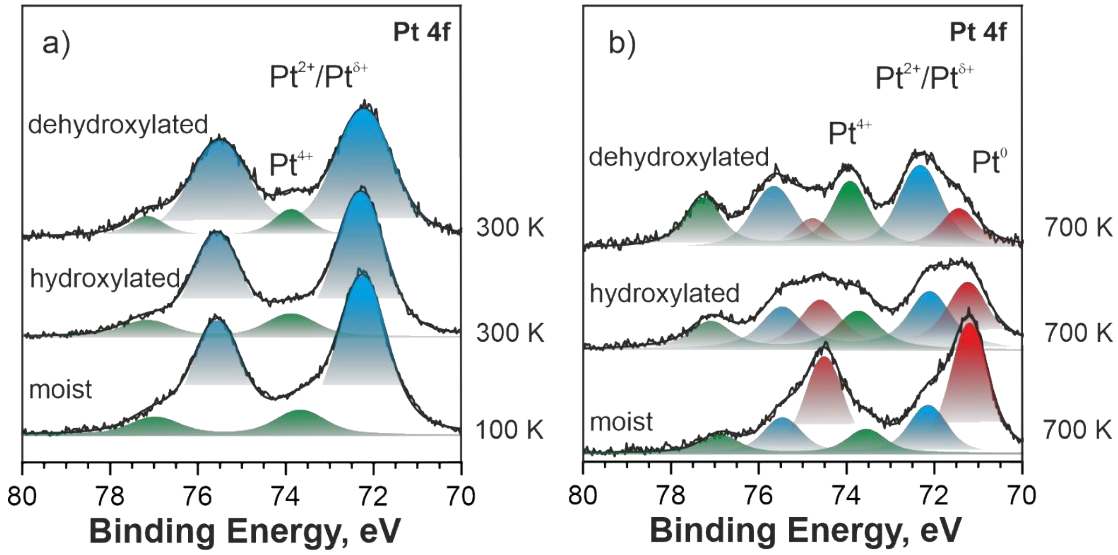

Figure 4.4: Pt 4f spectrum of dehydroxylated, hydroxylated and moist sample a) as prepared b) after annealing at 700 K. Adapted from ref. 177.

4.2. [P2] – Pd/Co_3O_4(111) interface formation

A model study presented in Section 4.1 focuses on the properties of the as-prepared Pt nanoparticles supported on Co_3O_4(111), their growth, stability and interaction with the support. The following presents an analogous study focusing on the properties of Pd nanoparticles on Co_3O_4(111) in UHV conditions. The growth of Pd nanoparticles is described from the initial state of nucleation and formation of Pd-Co_3O_4 interface. The EMSI strongly affects their stability and catalytical properties.[178] For the purpose of this study, Pd was deposited onto Co_3O_4(111) with the coverages varying between 0.05 monolayer equivalent (MLE) and 2 MLE. The as-prepared samples were investigated by means of STM and SRPES combined with DFT calculations of prof. Piccinin's group.

STM images of Pd nanoparticles with the coverages of 0.06 MLE, 0.18 MLE, and 1.91 MLE (Figure 4.5) reveal the grow of Pd nanoparticles from the initial state of nucleation. In all three cases, Pd nanoparticles are homogeneously dispersed on the Co_3O_4(111) surface. At low coverages, Pd forms small clusters with a characteristic size of approximately 1 nm. These clusters coalesce at higher coverage and form flat faceted islands of several nanometers. The size of the particles was calculated from their density and height determined from STM images and the amount of deposited Pd measured by QCM under the assumption of a cylindrical shape of the nanoparticles. The obtained values including the average number of Pd atoms per particle are summarized in Table 4.2.

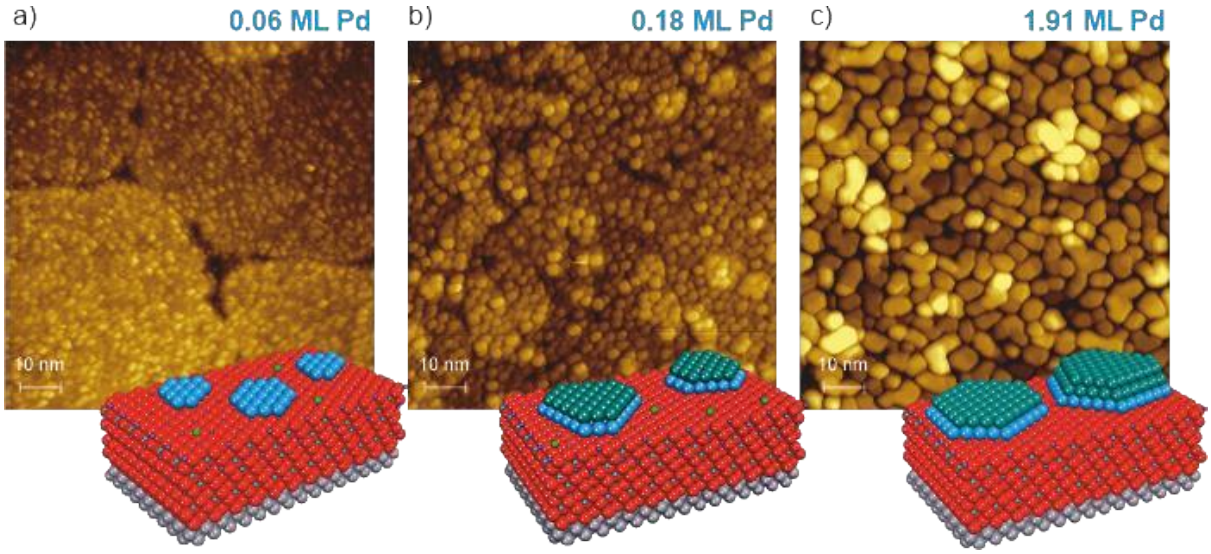

Figure 4.5: STM images of Co_3O_4 supported Pd nanoparticles. a) 0.06 ML b) 0.18 ML c) 1.91 ML. Adapted from ref. 179.

Table 2: Structural parameters of Pd nanoparticles. Adapted from ref. 179.

Pd (MLE)	Cluster density (cm^{-2})	Height (ML)	Average diameter (nm)	Atoms per nanoparticles
0.06	$0.7 \cdot 10^{13}$	1	1.1	15
0.18	$0.8 \cdot 10^{13}$	2	1.3	34
1.91	$0.27 \cdot 10^{13}$	3-4	5-6	1084

DFT[†] showed that the energetically most favorable site for a single Pd atom to adsorb on $Co_3O_4(111)$ is the FCC site with an adsorption energy of -2.84 eV and the corresponding Bader charge of +0.74e, which correspons to the state of Pd^{2+}. Pd atoms interact stronger with Co_3O_4 than among themselves. The adsorption energy of Pd dimer is -2.63 eV and the value for trimer is even lower. However, the adsorption energy starts growing for tetramers. Therefore, the driving force for Pd adatoms to form particles is relatively small. The analysis of Bader charge of Pd aggregates shows that Pd is partially oxidized in the state of $Pd^{\delta+}$. The average charge per Pd atom decreases with increasing size of the aggregate. In addition, DFT calculations suggest that small Pd aggregates tend to get oxidized to PdO in the presence of oxygen.

[†] DFT calculations were performed by theoretical group of prof. S. Piccinin from Istituto Officina dei Materiali, Consiglio Nazionale delle Richerche, Trieste

For small coverages of 0.05 MLE and 0.19 MLE, SRPES measurements (Figure 4.6) show two doublets in the Pd 3d spectrum at 337.1 eV and 338.4 eV. Based on the DFT calculations discussed in the previous paragraph, peaks might be assigned to small $Pd^{\delta+}$ metallic aggregates or PdO_x clusters, and atomically dispersed Pd^{2+} ions, respectively. The binding energies of $Pd^{\delta+}$ and Pd^{2+} in PdO match and small fraction of oxygen or water is always present in the UHV chamber. Therefore, it is not possible to distinguish between $Pd^{\delta+}$ and Pd^{2+} by means of SRPES. Since the position of $Pd^{\delta+}/Pd^{2+}$ doublet does not change with the coverage, the aggregates contain around 30 Pd atoms or less.[180] With increasing coverage, an additional doublet appears at 336.2 eV and shifts towards lower binding energy reaching 335.7 eV at the coverage of 1.24 ML. This behavior corresponds well with the growth of larger Pd^0 nanoparticles with Pd^{2+} and $Pd^{\delta+}$ serving as a nuclei for Pd^0 nanoparticles. The depth profiling shows that metallic Pd^0 covers Pd^{2+} and $Pd^{\delta+}$, which form the $Pd/Co_3O_4(111)$ interface.

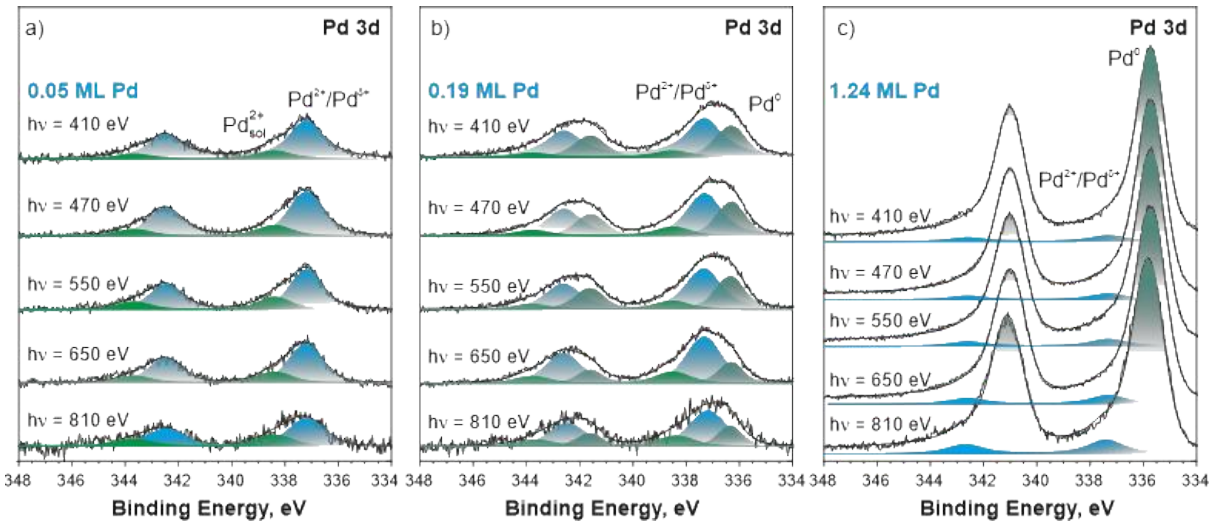

Figure 4.6: SRPES, Pd 3d spectra a) 0.05 ML b) 0.19 ML c) 1.24 ML. Adapted from ref. 179.

Finally, the charge transfer at the $Pd/Co_3O_4(111)$ interface was analyzed by comparing Co^{2+} and Co^{3+} intensities in the valence band spectra obtained with photon energy of 60 eV and in the resonant photoemission spectra. The obtained Co^{3+}/Co^{2+} ratio is shown in Figure 4.7a. The difference between these two methods originates in different photon energies affecting the information depth. This enabled us to determine the depth distribution of Co^{3+} and Co^{2+} ions (Figure 4.7 c, d**)**. The charge transfer is affecting the first two Co layers. Firstly, there is a preferential reduction of a small fraction of Co^{3+} in the first layer, which is most probably located at defect sites. Afterwards, the second layer consisting of Co^{3+} ions is reduced until the ratio reaches 1 at the coverage of 1.24 MLE. The number of electrons transferred from Pd

to Co_3O_4 equals the number of reduced Co^{3+} ions (Figure 4.7 b). Based on this assumption and the values in Table 4.1, the average charge transferred per Pd atom was determined. The obtained values of +1.02, +0.93, and +0.21 for coverages of 0.06 MLE, 0.18 MLE, and 1.91 MLE, respectively, shows that the charge transfer is located at $Pd/Co_3O_4(111)$ interface.

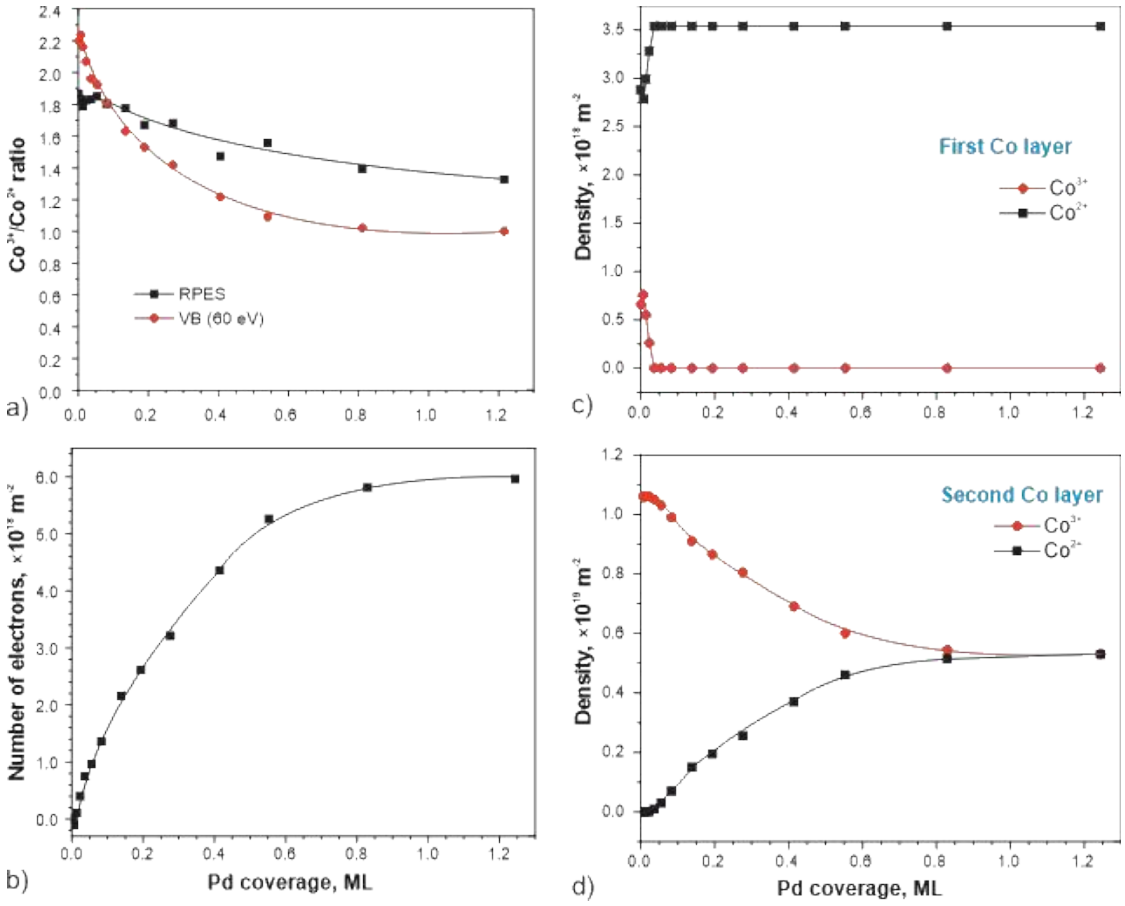

Figure 4.7: Pd coverage dependance of a) Co2+/Co3+ ratio b) charge transfer c), d) Co2+ and Co3+ distribution. Adapted from ref. 179.

In conclusion, deposition of small amount of Pd onto $Co_3O_4(111)$ results in highly dispersed and homogenously distributed Pd species. The interaction of the Pd species with the Co_3O_4 support results in a substantial charge transfer oxidizing the Pd species. Atomically dispersed Pd^{2+} species, and $Pd^{\delta+}$ aggregates in combination with PdO_x clusters were identified.

4.3. [P3] Stability of the $Pd/Co_3O_4(111)$ model catalysts in oxidizing and humid environments

In the follow-up work, the focus is on the stability of Pd nanoparticles supported on $Co_3O_4(111)$ substrate under humid and oxidizing environment mimicking the operation conditions of heterogeneous catalysts. For that purpose, Pd nanoparticles with coverage of

2 MLE were prepared and analyzed by means of STM and XPS in the temperature range of 300 K – 700 K in UHV and near-ambient pressure (1 mbar) conditions.

In UHV, the as-prepared sample show the behavior consistent with the results discussed in the previous chapter. STM showed that Pd forms flat nanoislands homogeneously dispersed on the $Co_3O_4(111)$ surface with a characteristic size of 4 nm (Figure 4.8a). The chemical state of Pd nanoparticles was determined from the Pd 3d XPS spectrum. The nanoparticles predominantly consist of metallic Pd^0 (contribution 1) with a small fraction of Pd^{2+} either in the form of PdO (contribution 2) or dissolved in $Co_3O_4(111)$ layer (contribution 3). Additionally, there is a minor contribution (contribution 4), which corresponds to plasmon features. The contribution 4 is separated from the metallic Pd^0 (contribution 1) by 6.4 eV, which fits the typical value of energy loss during the plasmon excitation.[181] After annealing at 700 K, Pd nanoparticles sinter and form larger well-faceted cluster (Figure 4.8b) with approximately half the density compared to RT. The Pd 3d XPS spectrum remains virtually unchanged. Sintering of the Pd nanoparticles caused only observed slight decrease of the intensity. The Co 2p spectrum also does not alter after annealing showing a high stability of the $Pd/Co_3O_4(111)$ catalyst under UHV conditions.

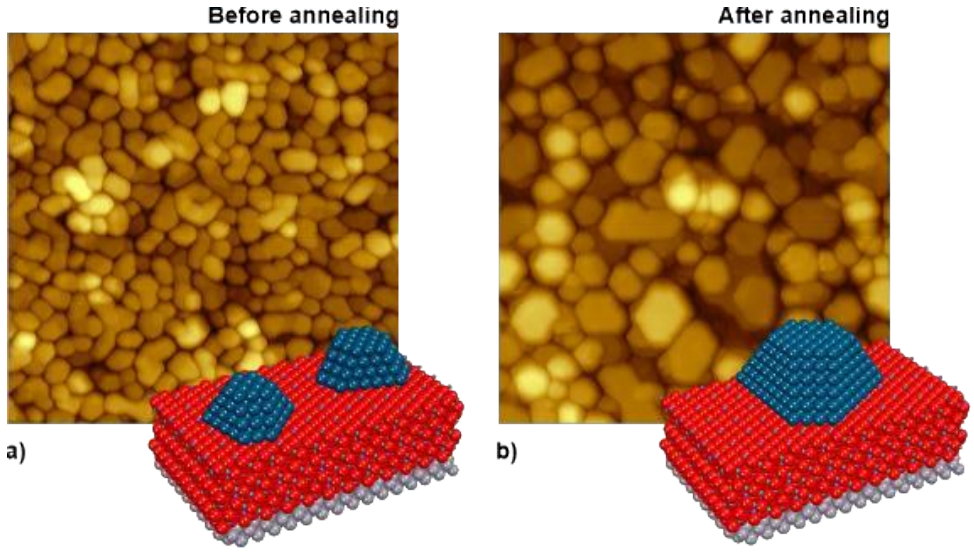

Figure 4.8: STM images of Co_3O_4 supported Pd nanoparticles a) as-prepared b) after annealing to 700 K. Adapted from ref. 182.

Afterwards, the stability of $Pd/Co_3O_4(111)$ was studied in the NAP cell using a monochromatized Al K-α source, which allows us to distinguish between the bulk (contribution 1a) and adsorbate-induced surface (contribution 1b) contribution of Pd^0 signal. To study the effect of oxidizing conditions XPS spectra were measured under three different

conditions – (i) UHV (<10^{-8} mbar), (ii) 1 mbar O_2, and (iii) evacuated (<10^{-5} mbar) – at constant temperature between 300 K and 700 K (Figure 4.9).

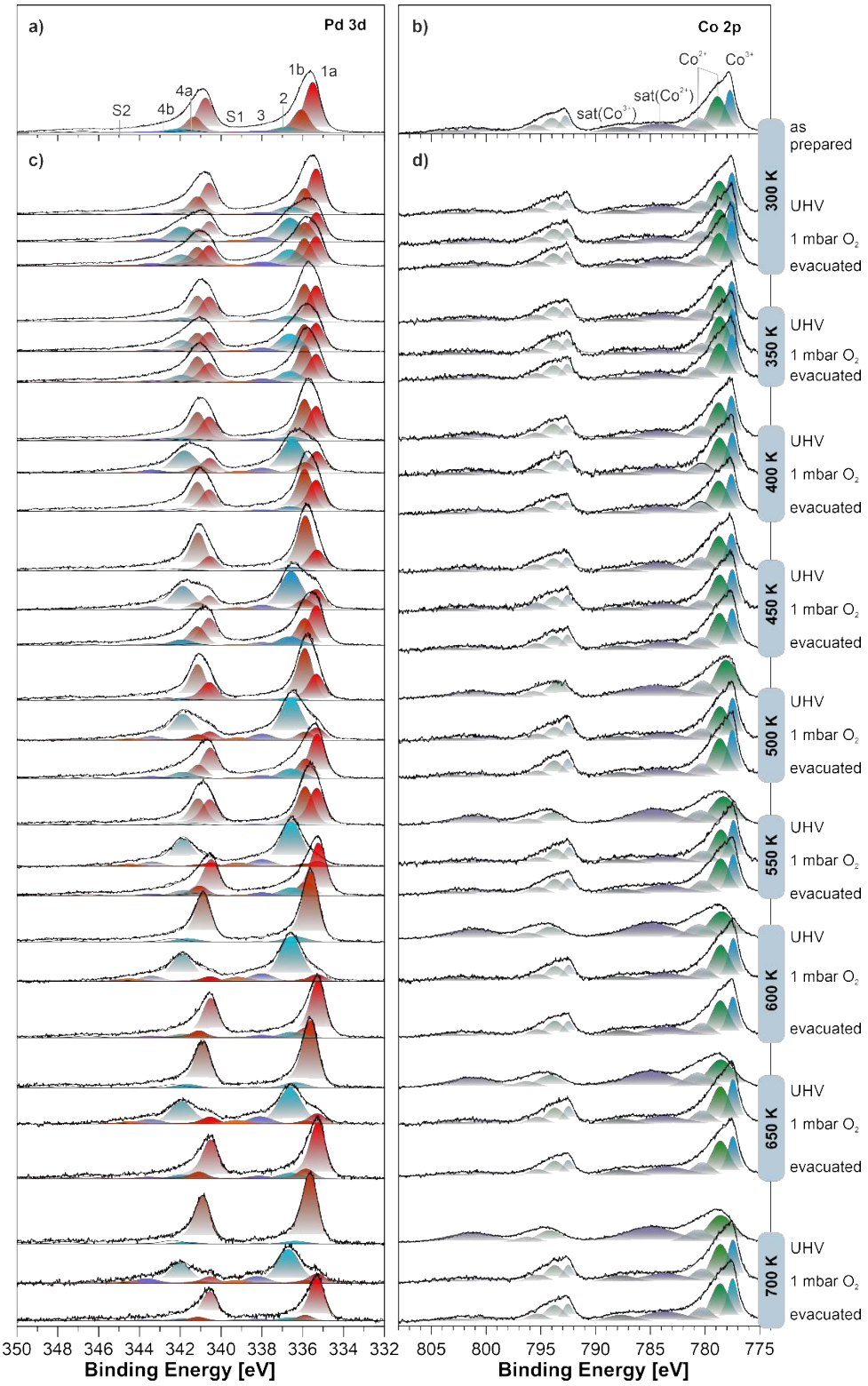

Figure 4.9: NAP-XPS, Pd 3d spectrum (a) and Co 2p spectrum (b) of the as-prepared Pd nanoparticles supported on the Co_3O_4(111). The evolution of XPS spectra during the annealing and exposure to oxygen a) Pd 3d spectra b) Co 2p spectra. Adopted from ref. 182.

After exposure to 1 mbar of oxygen, contribution 2 associated with formation of PdO increased starting at 300 K. PdO is stable in the whole temperature region 300 – 700 K. Noteworthy, the typical temperatures of the oxidation of single-crystal Pd surfaces lies above 550 K. Therefore, the oxidation of Pd nanoparticles is more favorable than oxidation of bulk Pd. In addition, the reducible oxide support may also play a role. However, it is not possible to distinguish whether the PdO is formed at the surface of the Pd nanoparticles or at the Pd/Co_3O_4(111) interface.

PdO decomposes after evacuation of the NAP cell. Contribution 2 decreases with simoultaneous increase of contribution 1. More specifically, the decrease of contribution 2 is coupled with a increase of contribution 1b between 300 K and 500 K, and contribution 1a above 500 K. The increase of contributrion 1b suggests that PdO decomposition yields either chemisorbed, surface or subsurface oxygen.

After annealing in UHV, Co_3O_4 started to reduce above 500 K with a complete reduction to CoO at 550 K. The CoO is oxidized back to Co_3O_4 after exposure to oxygen and remains oxidized until the next annealing in UHV. The increase of Co^{2+} signal during the redution is coupled with an increase of the Pd contibution 1b at the expanse of contribution 1a. This indicates that oxygen released during Co_3O_4 reduction is dissolved in Pd nanoparticles.

Similar to oxidizing conditions, the stability of Pd nanoparticles under humid conditions was studied. The same experimental procedure was followed where only the step (ii) was replaced by exposure to 1 mbar of H_2O. No changes were observed at temperatures below 450 K. At 450 K, the contribution 1b dramatically increases at the expense of contribution 1a. Similar to oxidizing conditions, this process is coupled with reduction of Co_3O_4 to CoO. In contrast with oxidizing conditions, CoO remains reduced and only minor changes are observed in the spectra above 450 K.

Finally, the NAP-XPS data were used to analyze the sintering and dissolution of Pd nanoparticles (Figure 4.10). During the annealing in UHV, the total intensity of Pd 3d spectra remain unchanged up to 550 K. Above this temperature, a slight decrease was observed caused by sintering of Pd nanoparticles. On the other hand, an intensity dropped significantly during annealing under oxidizing and humid environment. At 700 K, the loss of intensity reaches 80 % and 35 %, respectively. The detailed analysis of contributions 1-3 during the annealing cycles suggests that Pd^{2+} species diffuse under oxidizing conditions. The simulation of the intensity evolution showed that most of Pd^{2+} diffused into Co_3O_4 further

dissolve in the underlying Ir(100) substrate. Furthermore, the diffusion into Co_3O_4 is partially reversible, whereas, Pd dissolved in Ir(100) is permanently lost from the surface.

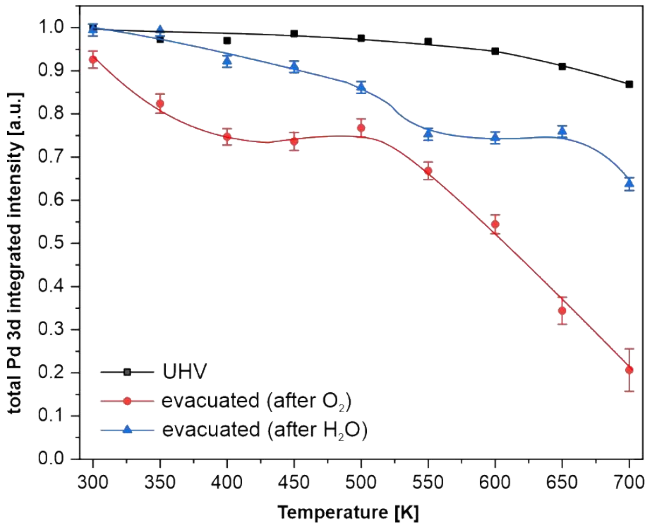

Figure 4.10: Dissolution of Pd. Total Pd 3d intesities after annealing in UHV (black) and during evacuation of the NAP cell after annealing in oxygen (red) and water (blue). Adapted from ref. 182.

This study showed that exposure to oxygen and subsequent annealing results in formation of PdO layer. On the other hand, exposure to water has no major effect on Pd nanoparticles. PdO is stable under oxygen atmosphere, but it decomposes after annealing in UHV. Additionally, a dissolution of Pd^{2+} into Co_3O_4 support, and subsequently the underlying Ir(100) was observed.

4.4. [P4] Particle size and shape effects in electrochemical environments: Pd particles supported on ordered Co_3O_4(111) and highly ordered pyrolytic graphite

This work continues in the study of the properties of Pd nanoparticles supported on Co_3O_4(111). The well-defined model catalyst may undergo a substantial changes in both chemical state and morphology after the first exposure to electrolyte resulting in the formation of new active electrocatalyst phases.[183]. The behavior and stability of Pd/Co_3O_4 catalyst were investigated under electrochemical conditions, specifically in alkaline electrolyte in a potential window between 0.5 – 1.5 V_{RHE}. In addition, the behavior of Co_3O_4 supported Pd nanoparticles was compared with Pd nanoparticles supported on highly ordered pyrolytic graphite (HOPG). In contrast to metal-oxides, HOPG represents a typical example

of a weakly interacting support. The metal-support interaction strongly affects the shape and properties of the supported nanoparticles.[184] For that purpose, three types of samples were prepared: Pd nanoparticles supported on $Co_3O_4(111)$ with high (2.5 MLE) and low (0.15 MLE) coverage and 1 MLE of Pd on HOPG.

The morphology and chemical state of as-prepared Pd nanoparticles on $Co_3O_4(111)$ were discussed in detail in the previous chapters. Pd nanoparticles supported on HOPG show qualitative differences in comparison with those supported on $Co_3O_4(111)$. Firstly, the Pd nanoparticles are hemispherical, but their density is comparable to the density of cylindrical nanoparticles on $Co_3O_4(111)$. Similarly to Pd nanoparticles on $Co_3O_4(111)$, Pd nanoparticles on HOPG are predominantly metallic. However, SRPES revealed an additional minor contribution at binding energy of 336.9 eV, which is assigned to Pd-carbon species located at the surface of the nanoparticles.

Afterwards, the samples were transferred without exposure to ambient atmosphere into electrochemical cell and immersed in alkaline electrolyte for several minutes under potential control. To evaluate the catalyst stability, an emersion SRPES measurements were performed with photon energies between 410 eV and 930 eV. The whole procedure was repeated for each potential step in the range of 0.5 – 1.5 V_{RHE}. The data for the lowest photon energy are shown in Figure 4.11. The oxidation state of Pd/HOPG and 2.5 ML Pd/ $Co_3O_4(111)$ is practically unaffected between 0.5 V_{RHE} and 1.1 V_{RHE}. There is only a minor contribution emerging at 338.4 eV for Pd/HOPG at 0.9 V_{RHE} and 1.1 V_{RHE}. The depth profiling shows, that this contribution is located at the surface indicating that it is associated with formation of surface oxide. For both, the formation of PdO starts at 1.3 V_{RHE} and continues at 1.5 V_{RHE}. In the last step, spectra after immersion-emersion at the initial potential of 0.5 V_{RHE} were measured. Even though, PdO is predominantly reduced back to metallic Pd^0, a contribution of PdO is still observed on top of the nanoparticles. For 0.15 ML Pd/ $Co_3O_4(111)$, the contribution associated to atomically dispersed Pd^{2+} in $Co_3O_4(111)$ disappears after first emersion at 0.5 V_{RHE}. Afterwards, no changes are observed in the Pd oxidation state. However, the contribution of partially oxidized $Pd^{\delta+}$ overlaps with contribution of Pd^{2+} in PdO. Therefore, it is not possible to disinguish between these two by means of SRPES.

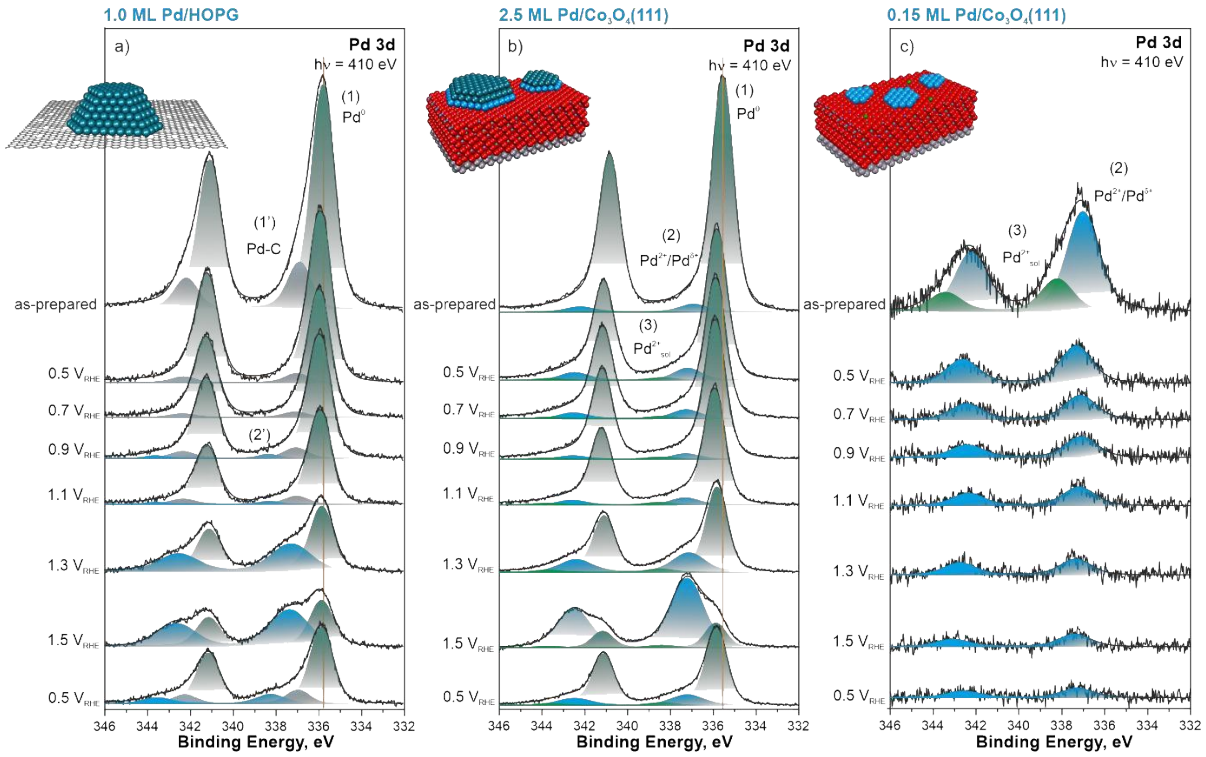

Figure 4.11: SRPES, Pd 3d spectra after after immersion in electrolyte a) 1.0 ML Pd/HOPG b) 2.5 ML Pd/Co_3O_4 c) 0.15 ML Pd/Co_3O_4. Adapted from ref. 185.

The intensity analysis shows a drop of intensity after the first emersion at 0.5 V_{RHE}. The drop is partially caused by attenuation of the signal by adsorbed carbon and residues of electrolyte. However, approximately 15 % of the intensity loss is related to dissolution of Pd. At higher potentials, only a small decrease in intensity was observed, which may be explained by gradual accumulation of adsorbed carbon and electrolyte residues.

The depth profiles of Pd/HOPG and 2.5 ML Pd/ Co_3O_4(111) after emersion at 1.3 V_{RHE} and 1.5 V_{RHE} (Figure 4.12) show that in both cases PdO is formed on the surface of the nanoparticles. The intensity analysis revealed that the formed PdO covers less than the top layer of the nanoparticles in both cases after emersion at 1.3 V_{RHE}. The coverage remains below a full monolayer for Pd/HOPG after emersion at 1.5 V_{RHE}, but greatly exceeds this amount for Pd/ Co_3O_4(111). The intensity simulations of different height distributions of Pd nanoparticles suggest that the key parameter affecting the extend of oxidation is the height. Particles with heights of 2 – 3 ML are fully oxidized, whereas, for higher nanoparticles, only the top layer is oxidized. This behavior may originate in EMSI, which influence the stability of Pd nanoparticles.

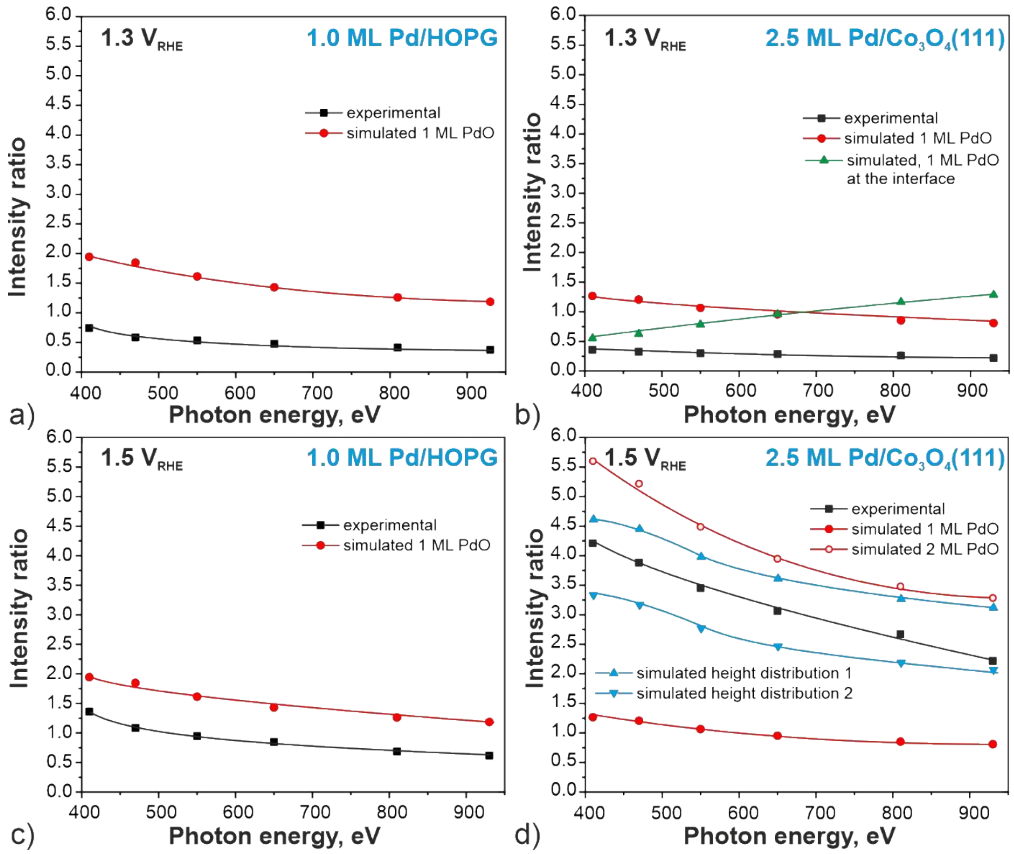

Figure 4.12: Intensity ratio between metallic Pd and PdO contributions after emersion at a given potencial as a function of photon energy. a) c) Pd/HOPG b) d) Pd/Co_3O_4. Adapted from ref. 185.

The Sections 4.2 – 4.4 represent a complex model study devoted to properties, EMSI, and stability of Pd/Co_3O_4 model catalyst under various conditions from UHV to elechtrochemical environment. The last one focuses on the stability and chemical state of supported Pd nanoparticles in alkaline electrolyte as a function of applied potential, particle size, and shape. The ultra small Pd nanoparticles on Co_3O_4 remain oxidizied after emersion. Therefore, no changes in Pd 3d spectra were observed apart from drop of intensity and loss of atomically disperse Pd^{2+}. For larger nanoprticles, the emersion between 0.5 – 1.1 V_{RHE} has basically no effect on oxidation state of Pd nanoparticles. Formation of surface PdO occurs at potentials 1.3 – 1.5 V_{RHE}. The extent of oxidation is larger for cylindrical nanoparticles on Co_3O_4 than for hemispherical nanoparticles on HOPG. Therefore, the stability of Pd nanoparticles depends on their shape, and consequently the EMSI.

4.5. [P5] - Stability, redox properties, and hydrogen intercalation in ceria-Pt model electrocatalyst

The model metal-oxide catalysts in conventional geometry are the perfect tool for studying the properties of the metal phase – typically supported nanoparticles or highly dispersed adatoms. However, these systems are less suitable for studying the properties of oxide phase. For such studies, the inverse model metal-oxide catalysts serve the best. Here, the properties of inverse model ceria-Pt catalyst are investigated in electrochemical environments. Ceria-Pt system exhibits favourable synergistic bi-functional effect in various energetically relevant reactions.[94,186] This work focuses on the stability of model ceria/Pt catalyst and oxidation/reduction properties of ceria nanoislands supported on Pt(111) in alkaline environment.

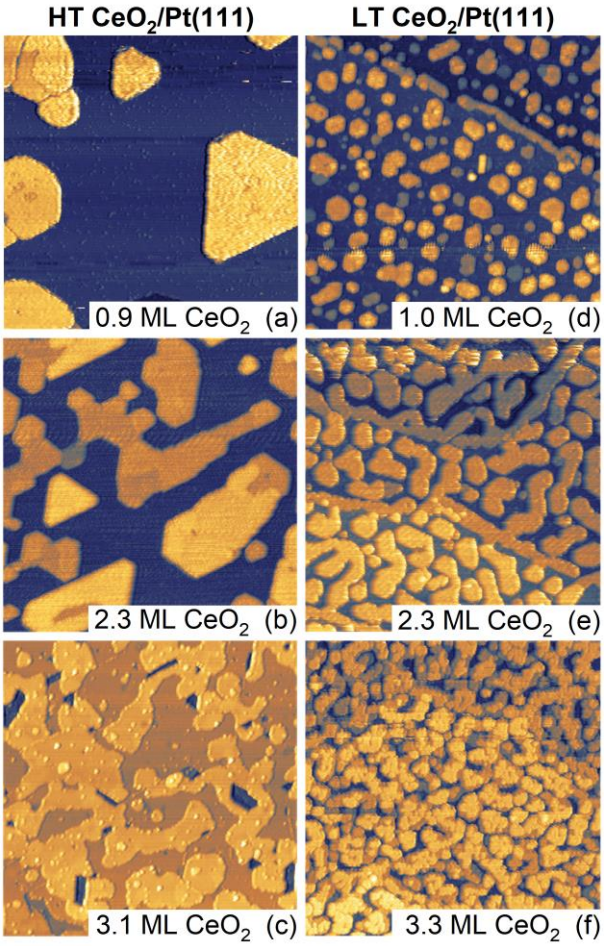

Figure 4.13: STM images (150 × 150 nm^2) of as-prepared CeO_2/Pt(111) model catalysts. a) HT sample, 0.9 MLE, b) HT sample, 2.3 MLE, c) HT sample, 3.1 MLE, d) LT sample 1.0 MLE, e) LT sample 2.3 MLE, f) LT sample, 3.3 MLE. Adapted from ref. 187.

Two series of CeO_2(111) nanoislands were deposited onto Pt(111) with varying ceria coverage by two preparation procedures and analyzed with the methods of surface science. STM analysis (Figure 4.13) reveals significant morphological differences between the two series. Ceria nanoislands annealed in the last step to 1050 K (Figure 4.13 a-c), hereafter denoted as high-temperature (HT) samples, show large flat islands with characteristic sizes of tens of nanometers and the island edges aligned with substrate main crystallographic directions (Figure 4.13 a). With increasing coverage, the nanoislands grow laterally forming almost a contiunous layer (Figure 4.13 c) resembling layer-by-layer deposition consistent with previous observations.[100] On the other hand, samples annealed in the last step to 850 K, hereafter denoted as low-temperature (LT) samples (Figure 4.13 d-f), results in small but still flat ceria nanoislands with round edges. With incresing coverage, the nanoislands coalesce forming structures with characteristic lateral size of few nanometers. Please note that LT and HT with the given coverage has the same height of nanoislands and show the same LEED pattern.

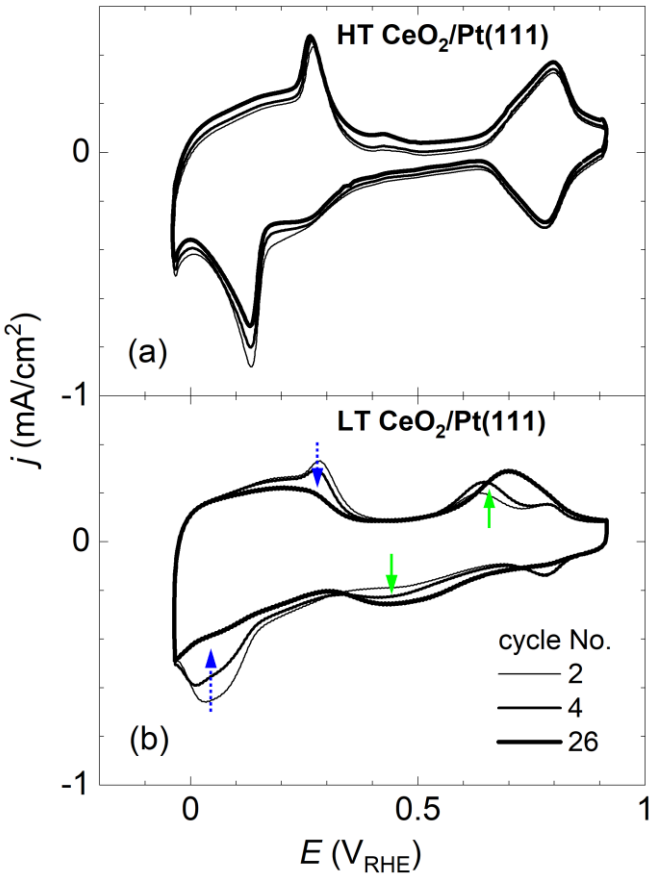

Figure 4.14: Electrochemical stability of HT (top) and LT (bottom) sample – CV cycle dependance. Adapted from ref. 187.

Apart from the characteristic size, these two types of qualitatively different structures (LT and HT) differ quantitatively in the length of the metal-oxide boundary. Whereas for the HT samples, 1 – 3 % of platinum surface atoms lie on the metal-oxide boundary, for the LT samples this ratio increases to 5 -7 %. XPS revealed differences in the chemical state of ceria. Concentration of Ce^{3+} ions is in the range of 4 – 8 % and 12 – 16 % for HT samples and LT samples, respectively.

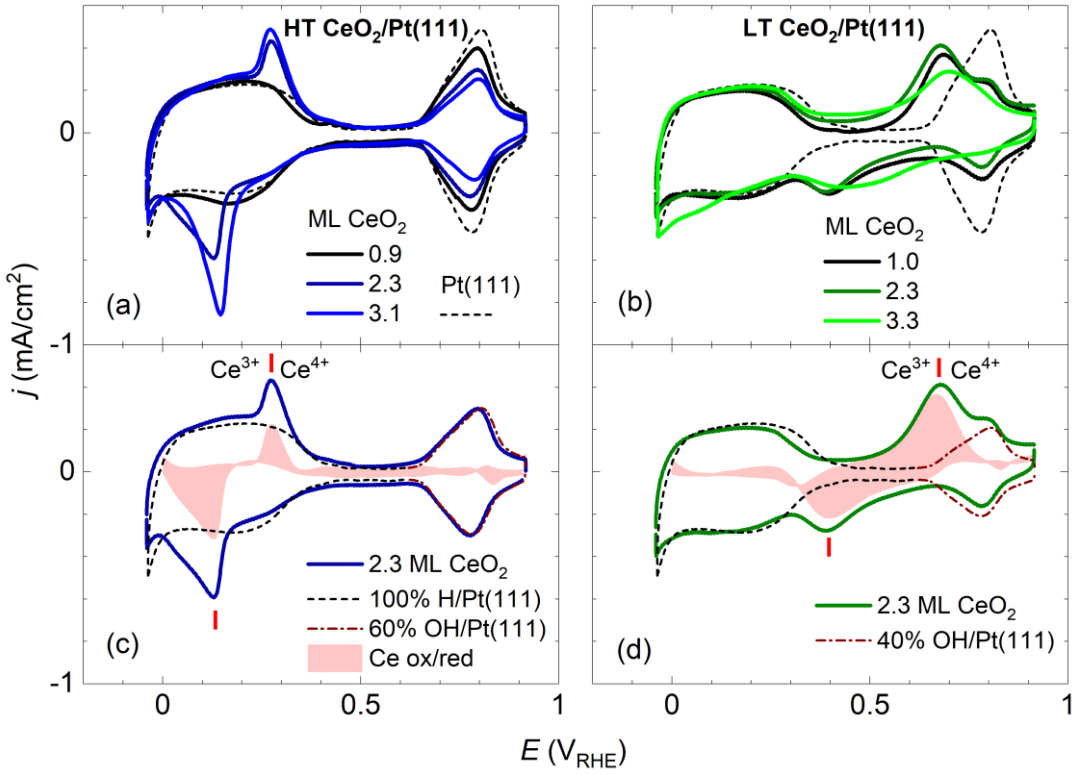

Figure 4.15: Stabilized CVs of HT and LT samples and charge analysis, reference CV of bare Pt(111) (dotted line). a) HT sample, 2.25 ML b) LT sample, 2.25 ML c) charge decomposition of stabilized HT CV, red area – contribution of Ce^{3+}/Ce^{4+} transition d) charge decomposition of stabilized LT CV, red area – contribution of Ce^{3+}/Ce^{4+} transition. Adapted from ref. 187.

After the preparation and characterization in UHV, the samples were transferred to EC cell. CVs obtained in 0.1 M KOH between -0.05 V_{RHE} and 0.9 V_{RHE} show electrochemical instability of LT samples. Voltammogram of HT samples doesn't change while cycling (Figure 4.14 top). In the case of LT samples (Figure 4.14 bottom), oxidation/reduction pair of peaks at 0 – 0.3 V_{RHE} dimishes and new pair of peaks appears at 0.4 – 0.7 V_{RHE}.

Analysis and assignment of the peaks is provided in Figure 4.14. CV of bare Pt(111) serving as a reference (dotted line, Figure 4.15 a,b) shows typical butterfly shape consisting of three distinct regions – H adsorption/desorption at potentials between -0.05 V_{RHE} and 0.35 V_{RHE}, double layer region from 0.35 V_{RHE} to 0.65 V_{RHE}, and OH adsorption/desorption at 0.65 –

0.9 V_{RHE}. In stabilized CVs of ceria, an additional irreversible pair of peaks aapears in H adsorption/desorption region for HT samples (Figure 4.15 a) and, in the LT samples a shifted one in the double layer region (Figure 4.15 b). In both cases, the irreversible pair is assigned to Ce^{3+}/Ce^{4+} redox transition. The shift of peaks to higher potentials for LT sample indicates change of Ce^{4+} phase. Ceria is predominantly identified as cubic CeO_2.[188,189] However, hydrated $CeO_2 \cdot 2H_2O$ was observed as amorphous phase[188] and the observed shift corresponds well with the value expected for the hydrated CeO_2.[190] Therefore, the observed irreversible pairs correspond to $CeO_2 \Leftrightarrow Ce(OH)_3$ and $CeO_2 \cdot 2H_2O \Leftrightarrow Ce(OH)_3$ transitions for HT and LT samples, respectively.

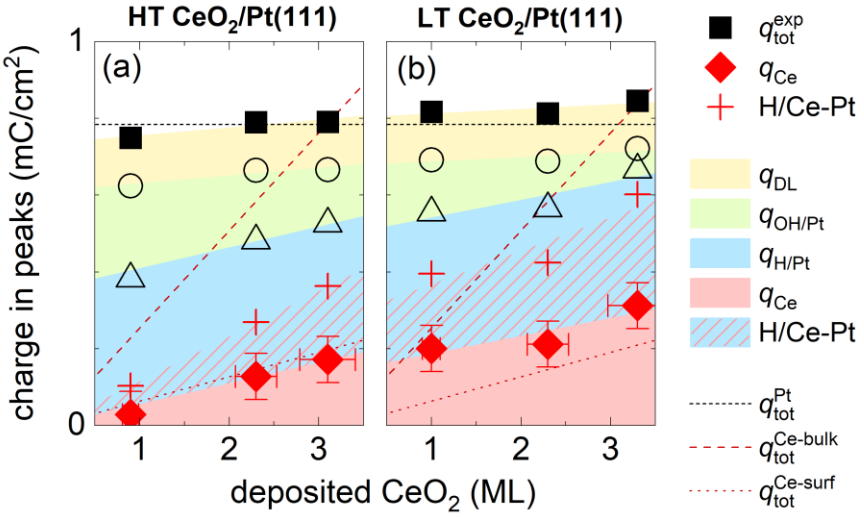

Figure 4.16: Charge contribution in the CVs. Adapted from ref. 187.

Finally, the charges of the Faradaic processes are analyzed in the CV (Figure 4.15 c,d). Three main contributions to the total charge (Figure 4.16) correspond to the following processes: the Ce^{3+}/Ce^{4+} transition (q_{Ce}), the H adsorption/desorption on Pt(111) ($q_{H/Pt}$), and the OH adsorption/desorption on Pt(111) ($q_{OH/Pt}$). Additionally, there is a small constant contribution of double layer (q_{DL}), which was determined from reference CV of bare Pt(111). For both types of samples, the charges of OH adsorption/desorption decrease proportionally to the coverage of the ceria nanoislands blocking the electrochemically active surface of platinum. Surprisingly, the charges of H adsorption/desorption do not decrease as one would expect based on the observations from previous metal inverse model catalyst studies.[69,191] To explain this counterintuitive behavior, there has to be a fast, reversible, non-Faradaic process removing the underpotentially deposited H from Pt(111) surface and replenishing it back during cathodic and anodic scan. Therefore, the suggested is H_{upd} intercalation at the ceria/Pt interface.

This study demonstrated a clear link between the structural properties of ceria nanoislands and their stability. Large ceria nanoislands with straight edges are stable during cycling in alkaline environment, while small ceria nanoisland with rounded edges undergo a phase transition to amorphous ceria hydrate. Additionally, an unexpected behavior of H atoms adsorbed at Pt(111) surface is observed – namely surface diffusion and intercalation of H atoms at the Pt/ceria interface.

4.6. [P6] Anchoring of porhyrins on atomically defined cobalt oxide: In-situ infrared spectroscopy at the electrified solid/liquid interface

While the previous studies dealt with the structure and stability of selected (electro)catalysts, the focus of this work is moved on to the third aspect of model electrocatalysis – adsorption properties. In this case, the adsorption of 5-mono(4-phosphonatophenyl)-10-15-20-triphenyl porphyrin (MPTPP) on a well-defined $Co_3O_4(111)$ thin film is studied to functionalize an electrode. In general, porphyrins are very good sensitizers for dye sensitized solar cells (DSSCs). However, the properties of DSSC and overall light to electron conversion efficiency is strongly affected by the functionality of organic/inorganic interface, and causatively the anchor group and binding motif are the key factors.

The Co_3O_4 substrate was prepared in UHV chamber by PVD as described in Section 3.4. After the preparation, the sample was transferred into 0.1 mM MPTPP solution in dichloromethane (DCM) without exposure to air. The porphyrin from the solution anchored to the $Co_3O_4(111)$ thin film. In the last step, the sample was transferred to EC cell with ammonia buffer for characterization by EC-IRRAS.

EC-IRRAS spectra were measured in the potential range of 0.3 V_{RHE} – 1.3 V_{RHE} with a step size of 0.1 V. In the anodic scan recorded with p-polarized light (Figure 4.17), a formation band appears at 1450 cm^{-1} and consumption band appears at 1115 cm^{-1} starting at 0.7 V_{RHE}. Additionally, s-shape band at 970 cm^{-1} appears at 0.9 V_{RHE}. The first two bands are related bending modes of NH_4^+ and NH_3, respectively, which indicates protonation of the ammonia buffer. This behavior is explained by hydroxylation of the substrate resulting in oxidation of surface Co^{2+} ions to Co^{3+} and releasing protons.

The band at 970 cm^{-1} is in the frequency region of phosphonates. Based on a DFT calculated spectrum (calculated by prof. Görling's group)‡, a reference transmission spectrum and our previous studies of phenylphosphonic acid,[192] we assign this band to the stretching vibration of PO_3^{2-}. Because no other bands related to the porphyrin are observed, we assume that MPTPP binds to the surface via phosphonate group in the form of chelating tridentate – i. e. all three oxygen atoms bind to one surface Co^{2+} ion.

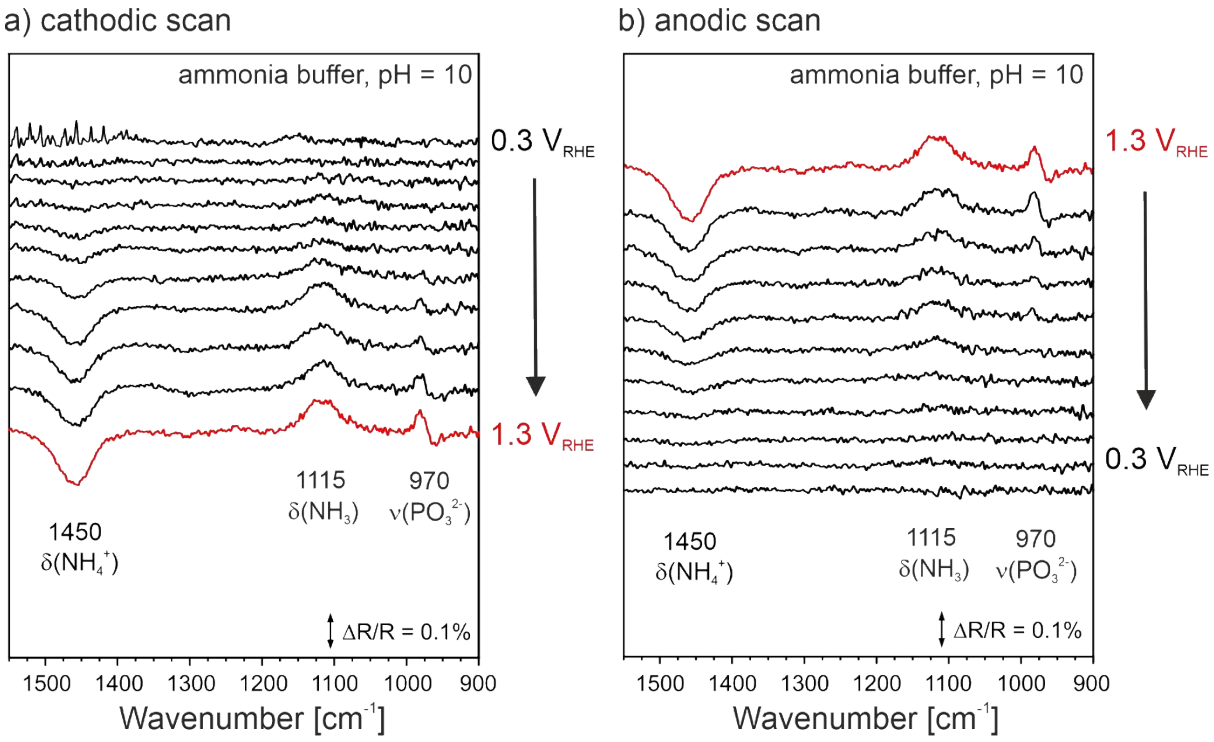

Figure 4.17: EC-IRRAS, $Co_3O_4(111)$ functionalized with MPTPP measured with p-polarized light at the potential window between 0.3 – 1.3 V_{RHE} a) cathodic scan b) anodic scan. Reference spectra measured at 0.3 V_{RHE}. Adapted from ref. 193.

In the cathodic scan, the intensities of all bands decrease with decreasing potential. The porphyrin band at 970 cm^{-1} fully disappears at 0.9 V_{RHE}, which is the same potential at which it appeared. Similarly, the ammonia buffer bands disappear at 0.7 V_{RHE}. This shows that all processes are fully reversible.

The bands described above were observed only with p-polarized light. There are no potential dependent changes in spectra measured with s-polarized light. Due to MSSR, only species in solution are observed with s-polarized light. Therefore, all processes are related to surface species.

‡ DFT calculation were performed by a theoretical group of prof. Andreas Görling, FAU Erlangen-Nürnberg

To determine the effect of solvent used during the porphyrin anchoring on the binding motif, the same experimental procedure was repeated using ethanol as a solvent instead of DCM. The same features as for DCM were identified in the spectra appearing at the same potentials. An additional band appears at 1240 cm^{-1} at 0.7 V_{RHE} and it is also related to ammonia buffer. Thus, the solvent does not affect the binding motif. However, the bands measured after anchoring from ethanol have higher intensities than bands measured after anchoring from DCM. Therefore, additional species co-adsorb to the surface during anchoring from DCM. These species are partially blocking the adsorption sites resulting in lower MPTPP coverage as well as lower ammonia protonation rate, and subsequently lower intensities of corresponding bands.

In conclusion, this study showed that MPTPP anchor to Co^{2+} terminated $Co_3O_4(111)$ surface in the form of chelating tridentate. The choice of the solvent (DCM or ethanol) during anchoring does not affect the binding motif. However, a co-adsorption of additional species from DCM blocks the adsorption sites and effectively decreases the porphyrin coverage.

4.7. [P7] Direct fuel cell liquid organic hydrogen carriers: The electrooxidation of cyclohexylethanol

Finally, we get to the last aspect of model catalysis, the reaction itself. The electrooxidation of 1-cyclohexylethanol on Pt catalyst for a potential use as an electrochemically active liquid organic hydrogen carrier (EC-LOHC). The key parameters of LOHC are the amount of hydrogen, which can be stored in and released from the molecule (hydrogen density), and the conditions under which the hydrogen is released. In this work, different possible reaction paths of 1-cyclohexylethanol oxidation are considered with different products as shown in Figure 4.18 and we determined which of them are realized during the reaction.

Firstly, the activity of different platinum single crystal catalysts towards the oxidation of 1-cyclohexylethanol was studied by prof. Thiele's group.[§] CVs (Figure 4.19) of Pt(100), Pt(110) and Pt(111) showed that the highest activity is reached with Pt(111) and the maximum is reached at 0.37 V_{RHE}. The activity of the other two surfaces is approximately one order of magnitude lower. However, the activity quickly drops and the oxidation peak shifts to higher potential during cycling. This might be caused by poisoning of the catalyst surface.

[§] CV measurement were performed by group of prof. Simon Thiele, Helmholtz Institute Erlangen-Nürnberg

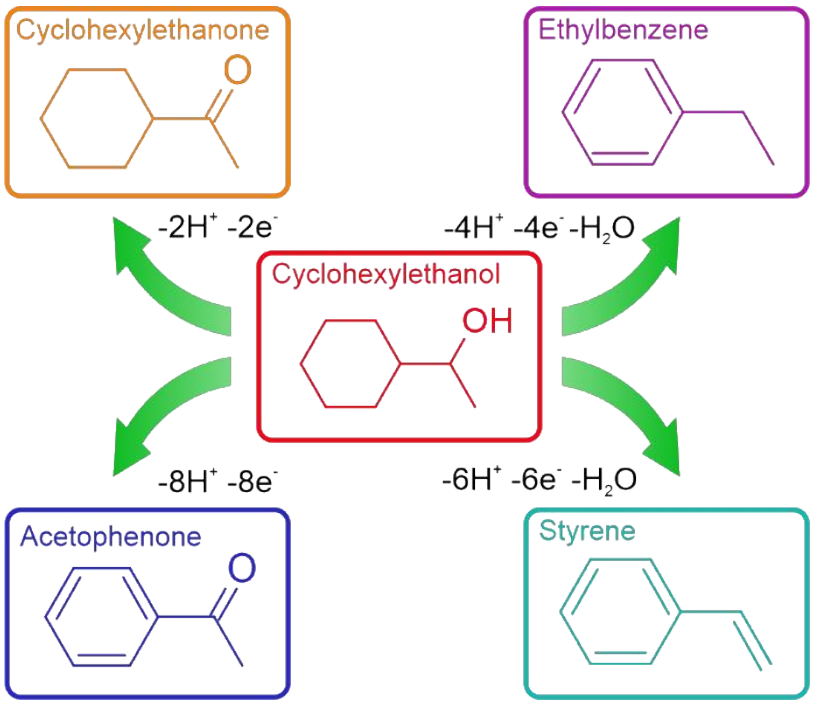

Figure 4.18: Schematic visualization of possible reaction products. Adapted from ref. 194.

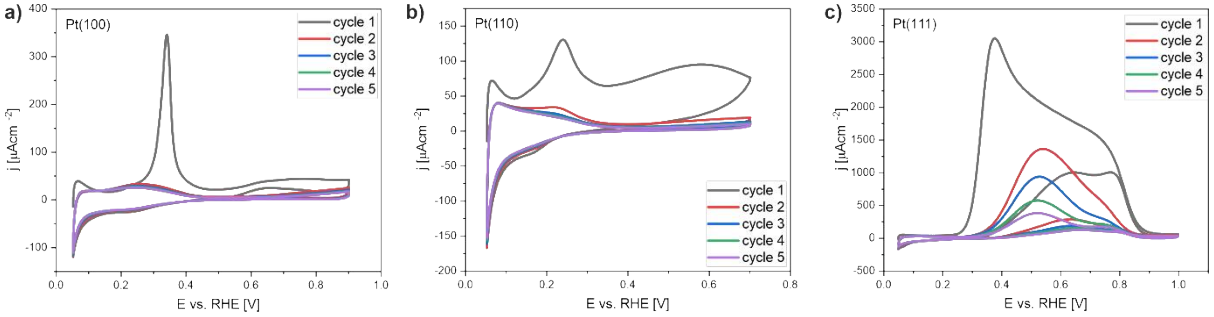

Figure 4.19: CVs of low-index Pt single crystals in 0.1M $HClO_4$ + 0.02 M 1-cyclohexyl ethanol. Adapted from ref. 194.

The products of the reaction were determined by EC-IRRAS. The spectra measured with s-polarized light between 0.05 V_{RHE} and 1.1 V_{RHE} (Figure 4.20) showed formation bands at 1174 cm^{-1}, 1199 cm^{-1}, 1259 cm^{-1}, 1295 cm^{-1}, 1359 cm^{-1} and 1435 cm^{-1}. The bands start to appear at 0.3 V_{RHE}, which is in perfect agreement with the onset potential of 0.27 V_{RHE} determined by CV. The similar features were observed with p-polarized light. Additional band was detected at 1690 cm^{-1}, which is overlapping with water-band region.

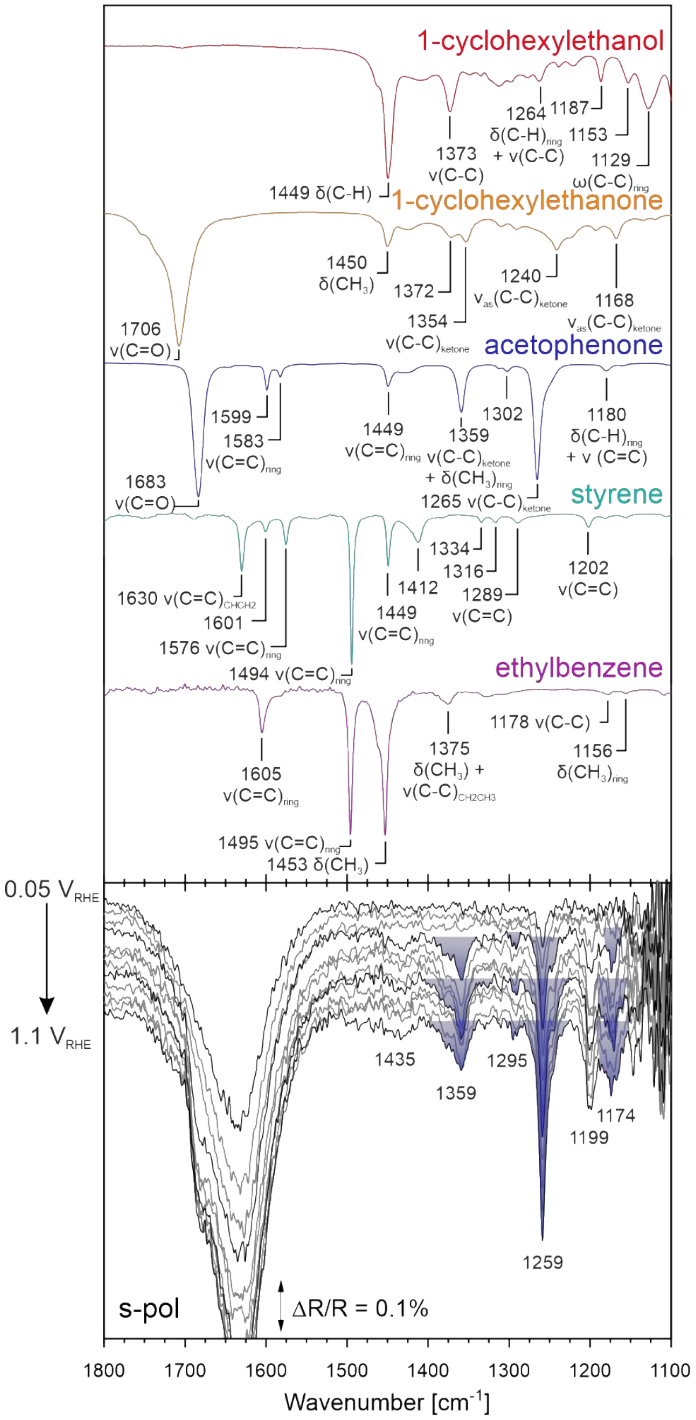

Figure 4.20: ATR IR reference spectra of 1-cyclohexyl ethanol and possible products of its dehydrogenation (top), potential dependent EC-IRRAS measured with s-polarized light (bottom). Adapted from ref. 194.

Based on ATR reference spectra and DFT calculated spectra (calculated by prof. Görling's group)[**], we assign bands at 1174 cm^{-1}, 1259 cm^{-1}, 1259 cm^{-1}, 1359 cm^{-1} and 1690 cm^{-1} to the formation of acetophenone. The bands have shoulders at 1259 cm^{-1} and 1359 cm^{-1}, which

[**] DFT calculation were performed by a theoretical group of prof. Andreas Görling, FAU Erlangen-Nürnberg

indicate that a fraction of 1-cyclohexylethanone is also formed. The band at 1450 cm^{-1} is related to vibrations of a C-H bond and cannot be assigned easily to a single molecule. Finally, the band at 1199 cm^{-1} is assigned to an unknown decomposition product. The presence of the acetophenone's bands in both, s-polarized and p-polarized, spectra shows that it desorbs from the surface and is present in the solution.

To reach a better understanding, a detailed EC-IRRA spectra were measured at 0.4 V_{RHE} (Figure 4.21) consisting of three cycles. In the first cycle, all bands were observed as described above. However, in the second and third cycle, only bands at 1199 cm^{-1} and 1259 cm^{-1} remain. This band is assigned to fragments of the molecules. This observation is in agreement with CV measurements and support the hypothesis of a quick poisoning of the Pt(111) surface.

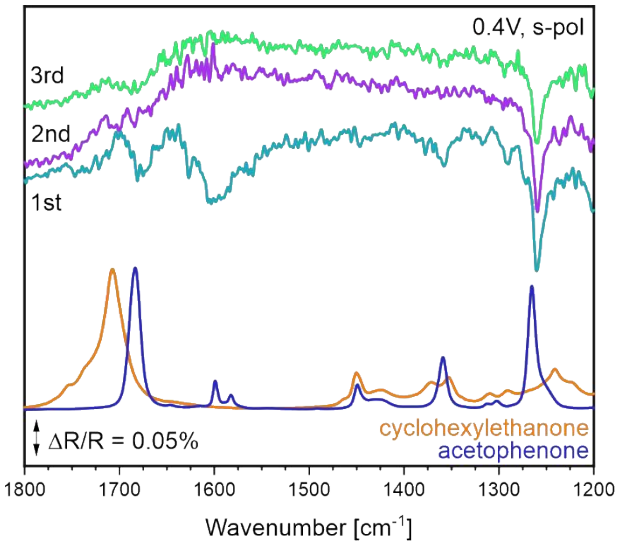

Figure 4.21: Time evolution of EC-IRRAS bands measured with s-polarized light at 0.4 V_{RHE}. Adapted from ref. 194.

In summary, Pt(111) shows among the low-index Pt surfaces the highest activity towards 1-cyclohexylethanol oxidation. Two products were identified – acetophenone and partially oxidized 1-cyclohexylethanone. This shows that it is possible to dehydrogenate both hydrogen storage functionalities – the cyclohexyl ring and the secondary alcohol functionality. So far the reaction is limited by a quick deactivation of the catalyst caused by decomposition of the molecule poisoning the surface. The major challenge will be to develop highly selective catalysts, which prevent decomposition and deactivation.

5. Summary

The thesis was conducted under the bilateral cotutelle agreement between the Charles University in Prague and the Friedrich-Alexander-Universität Erlangen-Nürnberg. It supported a long-lasting cooperation and transfer of knowledge between these institutions. During this thesis, a new EC cell designed at FAU was successfully implemented into the experimental setup at CU. The focus of this thesis lies on the model electrocatalytic studies of metal and metal-oxide based catalysts for application in energy relevant reactions and hydrogen economy. Due to the wide range of experimental methods, it was possible to address different aspects of model electrocatalysis and demonstrate their applicability to various (electro-)catalytic systems – namely Pt single crystal, $Co_3O_4(111)$, $Pt/Co_3O_4(111)$, $Pd/Co_3O_4(111)$, and ceria/Pt. The main findings of the individual studies are summarized as follows:

1) **Properties of $Pt/Co_3O_4(111)$ in UHV:** Pt forms on $Co_3O_4(111)$ a highly dispersed structure. The interaction between Pt and $Co_3O_4(111)$ results in significant charge transfer, which is also predicted by DFT calculations. The analysis of Bader charges shows positive charge on Pt atoms at the metal-oxide interface. The atomically dispersed Pt^{2+} and Pt^{4+} may substitute surface Co^{2+} and sub-surface Co^{3+} ions, respectively. In the presence of water, Pt^{4+} can be stabilized at FCC sites and form triaqua complex suppressing the sub-surface substitution.

2) **Properties of $Pd/Co_3O_4(111)$ in UHV:** Analogically to Pt, Pd species on $Co_3O_4(111)$ are highly dispersed and undergo a substantial charge transfer with $Co_3O_4(111)$. The transferred charge in the substrate is delocalized over top two layers. SRPES identified two main contribution, which correspond to atomically dispersed Pd^{2+} species, and small $Pd^{\delta+}$ aggregates or Pd_4O_x clusters. The depth profiling shows that above mentioned Pd species forms up to 2 ML thick clusters on top of which metallic Pd^0 nanoparticles grow.

3) **Stability of $Pd/Co_3O_4(111)$ under humid and oxidizing conditions:** After exposure to oxygen, Pd nanoparticles oxidize and form PdO layer. The degree of oxidation increases with increasing temperature. PdO is stable in the whole studied temperature range between 300 and 700 K. However, it decomposes after annealing in UHV

yielding metallic Pd^0 nanoparticles above 500 K. The oxidiation to PdO is accompanied by diffusion of Pd into $Co_3O_4(111)$ and further Ir(100). Whereas the diffusion into $Co_3O_4(111)$ is reversible, the diffusion into Ir(100) is irreversible. The exposure to humid environment does not affect Pd oxidation state.

4) **Stability of supported Pd nanoparticles in electrochemical environment:** In contrast with Co_3O_4 supported Pd, HOPG supported Pd forms metallic Pd^0 hemispherical nanoparticles due to weaker electronic metal-support interaction. Immersion of both types of Pd nanoparticles into alkaline electrolyte at potentials between 0.5 V_{RHE} and 1.1 V_{RHE} has no major effect on their oxidation state. At potentials between 1.3 and 1.5 V_{RHE}, the formation of PdO is observed, which is more pronounced on $Pd/Co_3O_4(111)$ than on Pd/HOPG. PdO is reduced back to Pd^0 after returning to initial potential of 0.5 V_{RHE}.

5) **Stability of ceria/Pt in electrochemical environment:** This study demonstrated structural effect on stability of ceria nanoislands in alkaline environment. Large nanoislands with straight edges are stable at potentials between -0.05 V_{RHE} and 0.9 V_{RHE}. On the other hand, small nanoislands with round edges are unstable and undergo transition to amorphous ceria hydrate. Charge analysis in the CVs revealed interesting behavior of H atoms adsorbed on Pt(111). These atoms reversibly diffuse and intercalate at the Pt/ceria interface allowing to accommodate H also on the Pt surface covered by ceria.

6) **Anchoring of porphyrin to $Co_3O_4(111)$:** It is possible to anchor monophosphatophenyl-triphenyl porphyrin (MPTPP) to $Co_3O_4(111)$ from a solution. MPTPP binds to the surface via phosphonic acid functionality to Co^{2+} surface atom in the form of chelating tridentate. The binding motif is stable in the potential range of 0.3 – 1.3 V_{RHE}. The choice of solvent (dichloromethane or ethanol) has no effect on binding motif. However, a co-adsorption of additional species was observed when adsorbing from DCM. The co-adsorbed species are blocking the adsorption sites resulting in lower porphyrin coverage than for adsorption from ethanol.

7) **Electrooxidation of 1-cyclohexylethanol:** Pt(111) shows in comparison with Pt(100) and Pt(110) the highest activity towards the oxidation of 1-cyclohexyl ethanol with

the onset potential of 0.3 V_{RHE} . However, all three surfaces quickly deactivate due to poisoning effect of decomposition products. EC-IRRAS identifies two products of 1-cyclohexyl ethanol oxidation – acetophenone and 1-cyclohexyl ethanone. The presence of acetophenone shows that it is possible to use and fully dehydrogenate two hydrogen storage functionalities in one molecule – cyclohexyl ring and secondary alcohol. However, finding a highly selective catalyst preventing the decomposition of the product will be the key factor for a potential use of this molecule as an electrochemically active liquid organic carrier (EC-LOHC).

In general, the presented model studies address different aspects of model electrocatalysis. The main focus was on the properties and stability of metal-oxide catalysts combining the noble metals (Pt, Pd) with reducible oxides (Co_3O_4, CeO_2). The results demostrated a strong impact of EMSI on the structural parameters of the supported metal nanoparticles, their oxidation state and consequently their stability in the electrochemical environment and their electrocatalytic properties. In addition, futher aspects of model electrocatalysis such as the adsorption of molecules from a solution and the identification of products of electrochemical reactions were studied. The presented findings clearly show the importance of model electrocatalysis and its role in the design, development and optimization of novel highly active and selective electrocatalysts.

6. Zusammenfassung

Die Arbeit wurde im Rahmen des bilateralen Cotutelle-Abkommens zwischen der Karls-Universität Prag und der Friedrich-Alexander-Universität Erlangen-Nürnberg durchgeführt. Dieses unterstützte eine langfristige Zusammenarbeit und den Wissenstransfer zwischen diesen Institutionen.

Im Rahmen der Arbeit wurde eine neue, an der FAU entwickelte EC-Zelle erfolgreich in den Versuchsaufbau an der Karls-Universität implementiert. Der Schwerpunkt dieser Arbeit liegt auf elektrokatalytischen Modellstudien von Metall- und Metalloxid-basierten Katalysatoren für die Anwendung in energierelevanten Reaktionen und der Wasserstoffwirtschaft. Dank des breiten Spektrums an experimentellen Methoden konnten verschiedene Aspekte der Modellelektrokatalyse behandelt und ihre Anwendbarkeit auf unterschiedliche katalytische Systeme gezeigt werden - nämlich Pt-Einkristalle, $Co_3O_4(111)$, Pt/ $Co_3O_4(111)$, Pd/$Co_3O_4(111)$ und Ceroxid/Pt. Die wichtigsten Ergebnisse der einzelnen Studien lassen sich wie folgt zusammenfassen:

1) **Eigenschaften von Pt/$Co_3O_4(111)$ im UHV:** Pt bildet auf $Co_3O_4(111)$ eine hochdisperse Struktur. Die Wechselwirkung zwischen Pt und $Co_3O_4(111)$ führt zu einem ausgeprägten Ladungstransfer, der auch durch DFT-Berechnungen vorhergesagt wird. Die Analyse der Bader-Ladung zeigt eine positive Ladung der Pt-Atome an der Metall-Oxid-Grenzfläche. Die atomar dispergierten Pt^{2+} und Pt^{4+} Spezies können die Co^{2+}-Ionen an der Oberfläche bzw. die Co^{3+}-Ionen unter der Oberfläche ersetzen. In Gegenwart von Wasser kann Pt^{4+} an FCC-Stellen stabilisiert werden und einen Triaqua-Komplex bilden, der die Substitution unter der Oberfläche unterdrückt.

2) **Eigenschaften von Pd/$Co_3O_4(111)$ im UHV:** Analog zu Pt sind die Pd-Spezies auf $Co_3O_4(111)$ hochgradig dispergiert und erfahren einen deutlichen Ladungstransfer mit $Co_3O_4(111)$. Die übertragene Ladung im Substrat ist über die beiden oberen Schichten delokalisiert. Spektroskopisch wurden zwei Hauptbeiträge identifiziert, erstens atomar dispergierte Pd^{2+}-Spezies und zweitens kleine $Pd^{\delta+}$-Aggregate oder Pd_4Ox-Cluster. Die Tiefenprofilierung zeigt, dass die oben genannten Pd-Spezies bis zu 2 ML dicke Cluster bilden, auf denen metallische Pd^0-Nanopartikel wachsen.

3) **Stabilität von Pd/Co_3O_4(111) unter oxidierenden Bedingungen und Wasser-Atmosphere:** Nach der Einwirkung von Sauerstoff oxidieren die Pd-Nanopartikel und bilden eine PdO-Schicht. Der Grad der Oxidation nimmt mit steigender Temperatur zu. PdO ist im gesamten untersuchten Temperaturbereich von 300 - 700 K stabil. Es zersetzt sich jedoch nach dem Glühen im UHV, wobei oberhalb von 500 K metallische Pd^0-Nanopartikel entstehen. Die Oxidation zu PdO wird von der Diffusion von Pd in Co_3O_4(111) und weiter in Ir(100) begleitet. Während die Diffusion in Co_3O_4(111) reversibel ist, ist die Diffusion in Ir(100) irreversibel. Die Einwirkung einer Wasserdampfumgebung hat keinen Einfluss auf den Oxidationszustand von Pd.

4) **Stabilität der geträgerten Pd-Nanopartikel in elektrochemischer Umgebung:** Im Gegensatz zu Pd auf Co_3O_4-Substrate bildet Pd auf HOPG-Substrate aufgrund einer schwächeren elektronischen Metall-Substrat-Wechselwirkung metallische halbkugelförmige Pd^0-Nanopartikel. Das Anlegen von Potentialen zwischen 0,5 V_{RHE} und 1,1 V_{RHE} in einem alkalischen Elektrolyten (Phosphat Puffer, pH 10) hat auf den Oxidationszustand beider Arten von Pd-Nanopartikeln keinen wesentlichen Einfluss. Bei Potentialen von 1,3 - 1,5 V_{RHE} beobachtet man die PdO-Bildung, die auf Pd/Co_3O_4(111) stärker ausgeprägt ist als auf Pd/HOPG. PdO wird nach der Rückkehr zum Anfangspotential von 0,5 V_{RHE} wieder zu Pd reduziert.

5) **Stabilität von Ceroxid/Pt in elektrochemischer Umgebung:** Es wurden die strukturelle Auswirkungen auf die Stabilität von Ceroxid-Nanoinseln in alkalischer Umgebung nachgewiesen. Große Nanoinseln mit geraden Kanten sind bei Potentialen zwischen -0,05 V_{RHE} und 0,9 V_{RHE} stabil. Dagegen sind kleine Nanoinseln mit runden Kanten instabil und gehen in amorphes Ceroxidhydrat über. Die Ladungsanalyse in den CVs ergab ein interessantes Verhalten der auf Pt(111) adsorbierten H-Atome. Diese Atome diffundieren reversibel und interkalieren an der Pt/Ceroxid-Grenzfläche.

6) **Verankerung eines Porphyrins auf Co_3O_4(111):** Es ist möglich, Monophosphatophenyl-Triphenyl-Porphyrin (MPTPP) aus einer Lösung auf Co_3O_4(111) zu verankern. MPTPP bindet an die Oberfläche über eine Phosphonsäurefunktionalität an das Co^{2+}-Oberflächenatom in Form eines chelatbildenden Tridentats. Das Bindungsmotiv ist in einem Potentialbereich von 0,3 - 1,3 V_{RHE} stabil. Die Wahl des Lösungsmittels (Dichlormethan oder Ethanol) zur

Verankerung hat keinen Einfluss auf das Bindungsmotiv. Allerdings wurde bei der Adsorption aus DCM eine Koadsorption zusätzlicher Spezies beobachtet. Die koadsorbierten Spezies blockieren die Adsorptionsstellen, was zu einer geringeren Porphyrinbedeckung im Vergleich zur Adsorption aus Ethanol führt.

7) **Elektrooxidation von 1-Cyclohexylethanol:** Pt(111) zeigt im Vergleich zu Pt(100) und Pt(110) die höchste Aktivität bei der Oxidation von 1-Cyclohexylethanol mit einem Onset-Potential von 0,3 V_{RHE}. Alle drei Oberflächen deaktivieren jedoch schnell aufgrund von Katalysatorvergiftung durch Zersetzungsprodukte. Durch EC-IRRAS wurden zwei Produkte der 1-Cyclohexylethanoloxidation - Acetophenon und 1-Cyclohexylethanon - identifiziert. Das Auftreten von Acetophenon zeigt, dass es möglich ist, zwei Wasserstoffspeicherfunktionen in einem Molekül – nämlich der Cyclohexylring und die sekudäre Alkoholfuktion - zu nutzen und vollständig zu oxydieren. Die Suche nach einem hochselektiven Katalysator, der die Zersetzung des Produkts verhindert, wird jedoch der Schlüsselschritt für eine potenzielle Verwendung dieser Verbindung als elektrochemisch aktiver flüssiger organischer Wasserstoffträger sein.

Zusammenfassend wurde eine Reihe von Modellstudien durchgeführt, die verschiedene Aspekte der Modellelektrokatalyse behandeln. Der Schwerpunkt lag dabei auf den Eigenschaften und der Stabilität von Metalloxid-Katalysatoren, die Edelmetalle (Pt, Pd) mit reduzierbaren Oxiden (Co_3O_4, CeO2) kombinieren. Es konnte ein starker Einfluss der EMSI auf die strukturellen Parameter der Metallnanopartikel, ihren Oxidationszustand und folglich ihre Stabilität in elektrochemischer Umgebung, sowie ihre elektrokatalytischen Eigenschaften nachweisen. Darüber hinaus wurden Studien durchgeführt, die sich mit weiteren Aspekten der Modellelektrokatalyse befassen: Die Adsorption von Molekülen aus einer Lösung und die Identifizierung von Produkten elektrochemischer Reaktionen. Die vorgestellten Ergebnisse zeigen deutlich die Bedeutung der Modellelektrokatalyse und ihre Rolle bei der Konzeption, Entwicklung und Optimierung neuartiger hochaktiver und selektiver Elektrokatalysatoren.

7. Závěr

Práce byla vypracována v rámci bilaterální dohody cotutelle mezi Univerzitou Karlovou v Praze a Univerzitou Friedricha Alexandra Erlangen-Nürnberg. Podpořila tak dlouhodobou spolupráci a přenos znalostí mezi těmito institucemi. V rámci této práce byla úspěšně implementována do experimentálního uspořádání na UK nová elektrochemická cela navržená na FAU. Práce se zaměřuje na modelové studie katalyzátorů na bázi kovů a oxidů kovů pro použití v energeticky významných reakcích a vodíkovém hospodářství. Díky širokému spektru experimentálních metod jsme se mohli zabývat různými aspekty modelové elektrokatalýzy a prokázat jejich použitelnost na různých katalytických systémech - konkrétně na monokrystalu Pt, $Co_3O_4(111)$, $Pt/Co_3O_4(111)$, $Pd/Co_3O_4(111)$ a CeO_2/Pt. Hlavní poznatky jednotlivých studií lze shrnout následovně:

1) **Vlastnosti Pt/Co3O4(111) v UHV**: Pt nanočástice na $Co_3O_4(111)$ jsou vysoce dispergované. Interakce mezi Pt a $Co_3O_4(111)$ vede ke značnému přenosu náboje, který byl předpovězen i DFT výpočty. Analýza Baderova náboje ukazuje kladný náboj na Pt částicích na rozhraní kov-oxid. Atomárně rozptýlené Pt^{2+} a Pt^{4+} mohou nahradit povrchové Co^{2+} a podpovrchové Co^{3+} ionty. V přítomnosti vody se Pt^{4+} může stabilizovat v FCC pozici a vytvářet triaqua komplex potlačující podpovrchovou substituci Co.

2) **Vlastnosti Pd/Co3O4(111) v UHV**: Analogicky k Pt nanočásticím, Pd tvoří na $Co_3O_4(111)$ vysoce disperzní strukturu a pozorujeme významný přenos náboje. Přenesený náboj je v substrátu delokalizován v horních dvou monovrstvách. Spektroskopicky jsme identifikovali dva hlavní příspěvky, které přiřazujeme atomárně rozptýleným částicím Pd^{2+} a malým agregátům $Pd^{\delta+}$ nebo klastrům Pd_4O_x. Hloubkové profilování ukazuje, že výše zmíněné částice Pd tvoří až 2 ML silné klastry, na jejichž vrcholu rostou kovové nanočástice Pd^0.

3) **Stabilita $Pd/Co_3O_4(111)$ v oxidačních podmínkách a za přítomnosti vody**: Po působení kyslíku nanočástice Pd oxidují a vytvářejí vrstvu PdO. Stupeň oxidace se zvyšuje s rostoucí teplotou. PdO je stabilní v celém studovaném teplotním rozsahu 300 - 700 K. Po žíhání nad 500 K v UHV se však rozkládá za vzniku kovových nanočástic Pd^0. Oxidace na PdO je doprovázena pronikáním Pd do $Co_3O_4(111)$ a dále

do Ir(100). Zatímco pronikání do $Co_3O_4(111)$ je vratné, pronikání do Ir(100) je trvalé. Přítomnost vody nemá vliv na oxidační stav Pd.

4) **Stabilita nanočástic Pd v elektrochemickém prostředí**: Díky slabší interkci mezi kovem a substrátem tvoří Pd na HOPG, narozdíl od Pd na $Co_3O_4(111)$, polokulovité nanočástice Pd^0. Ponoření obou typů nanočástic Pd do alkalického elektrolytu při potenciálech mezi 0,5 V_{RHE} a 1,1 V_{RHE} nemá žádný zásadní vliv na jejich oxidační stav. Při potenciálech 1,3 - 1,5 V_{RHE} pozorujeme tvorbu PdO, která je výraznější na $Pd/Co_3O_4(111)$ než na Pd/HOPG. Po návratu na počáteční potenciál 0,5 V_{RHE} se PdO redukuje zpět na Pd.

5) **Stabilita CeO_2/Pt v elektrochemickém prostředí**: Prokázali jsme strukturní vliv na stabilitu ceroxidových nanoostrůvků v alkalickém prostředí. Velké nanoostrůvky s rovnými hranami jsou stabilní při potenciálech mezi -0,05 V_{RHE} a 0,9 V_{RHE}. Naproti tomu malé nanoostrůvky se zaoblenými hranami jsou nestabilní a podléhají přechodu na amorfní hydrát ceru. Nábojová analýza v CV odhalila zajímavé chování atomů H adsorbovaných na Pt(111). Tyto atomy reverzibilně difundují a interkalují na rozhraní Pt/CeO_2, což umožňuje akumulaci H i na povrchu Pt pokrytém ceroxidem.

6) **Adsorpce porfyrinu na Co3O4(111)**: Monofosfátofenyl-trifenyl porfyrin (MPTPP) je možné z roztoku adsorbovat na $Co_3O_4(111)$. MPTPP se váže na povrch prostřednictvím funkční skupiny kyseliny fosforečné na povrchový atom Co^{2+} pomocí tří vazeb Co-O. Vazebný motiv je stabilní v rozsahu potenciálů 0,3 - 1,3 V_{RHE}. Volba rozpouštědla (dichlormethan nebo ethanol) nemá na vazebný motiv vliv. Při adsorpci z DCM jsme však pozorovali koadsorpci dalších molekul. Koadsorbované molekuly blokují adsorpční místa, což má za následek nižší pokrytí porfyrinu než při adsorpci z ethanolu.

7) **Elektrooxidace 1-cyklohexyletanolu**: Pt(111) vykazuje ve srovnání s Pt(100) a Pt(110) nejvyšší aktivitu vůči oxidaci 1-cyklohexylethanolu s onset potenciálem 0,3 V_{RHE} . Všechny tři povrchy se však rychle deaktivují v důsledku jejich otravy molekulami vzniklými rozpadem produktu. Pomocí EC-IRRAS jsme identifikovali dva produkty oxidace 1-cyklohexylethanolu - acetofenon a 1-cyklohexylethanon. Přítomnost acetofenonu ukazuje, že je možné využít a plně dehydrogenovat dvě různé

funkční skupiny v jedné molekule - cyklohexylové jádro a sekundární alkohol. Klíčovým faktorem pro potenciální využití této molekuly jako kapalného organického nosiče pro přímé palivové články (D-LOHC) však bude nalezení vysoce selektivního katalyzátoru, který zabrání rozpadu produktu.

V této práci jsme představili řadu modelových studií, které se zabývají různými aspekty modelové elektrokatalýzy. Hlavní pozornost byla věnována vlastnostem a stabilitě katalyzátorů typu kov-oxid kombinujících vzácné kovy (Pt, Pd) s redukovatelnými oxidy (Co_3O_4, CeO_2). Ukázali jsme vliv EMSI na strukturní parametry kovových nanočástic na oxidových susbstrátech, jejich oxidační stav a následně jejich stabilitu v elektrochemickém prostředí a jejich elektrokatalytické vlastnosti. Dále jsme provedli studie zabývající se dalšími aspekty modelové elektrokatalýzy, kde jsme se věnovali adsorpci organických molekul a identifikaci produktů elektrokatalytických reakcí. Předložené výsledky jasně ukazují význam modelové elektrokatalýzy a její úlohu při navrhování, vývoji a optimalizaci vlastností nových vysoce aktivních a selektivních elektrokatalyzátorů.

8. Acknowledgement

The whole doctoral studies and preparation of this thesis was an amazing journey, which showed me a fascinating field of model catalysis, taught me to be self-sufficient and systematic in solving complex problems and allowed me to be a part of a fruitful international and interdisciplinary cooparation offering new experience and friendships. Nothing of this wouldn't have happened without a help and support of many people. Here, I would like to sincerely thank them all.

Namely and firstly, I would like to thank prof. Dr. Jörg Libuda and doc. Mgr. Josef Mysliveček, Ph.D. for their help and guidance along the whole journey, and especially their courage and willingness to conduct the doctorate under cotutelle agreement, which was new for both of them.

I would also like to thank all my colleagues for the friendly working environment, willingness to help, all scientfic discussions and friendly talks. Namely, doc. RNDr. Viktor Johánek, Ph.D., Michal Ronovský, Pankaj Kumar Samal, Jan Škvára, Vitaliy Uvarov and Zdeněk Rafaj from CU, and Dr. Olaf Brummel, Dr. Yaroslava Lykhach, Dr. Tanja Bauer, Alexander Simanenko, Dr. Corrina Stumm, Dr. Chantal Hohner, Dr. Christian Schuschke, Dr. Dominik Blaumeiser, Evanie Franz, Felix Hilpert, Georg Fickenscher, Hanna Bühlmeyer, Huiyi Xu, Jonas Hauner, Juntao Yang, Kailun Zhang, Karl Farrugia, Dr. Manon Bertram, Maximilian Kastenmeier, Dr. Ralf Schuster, Robert Hübsch, Roman Eschenbacher, Simon Schötz, Simone Reindl and Zarah Hussain from FAU. Apart from that I would like to thank Melanie Füssel and Marcela Chvalkovská for their help with all administrative matters.

Furthermore, I would like to thank all collaboration partners – Dr. Tomáš Skála, Dr. Nataliya Tsud and Dr. Sascha Mehl from Elettra-Sincrotrone, prof. Dr. Andreas Görling and Lukas Fromm from Theoretical Chemistry FAU, prof. Dr. Simone Piccinin, Dr. Stefano Fabris and Dr. Matteo Farnesi Camellone from Istituto Officina dei Materiali Trieste, prof. Dr. Peter Wasserschied, Dr. Serhiy Cherevko, Maria Minichová and Valentín Briega-Martos from Helmholtz-Institute, and many others.

Last but not least, I would like to thank my family for their support. Espescially, I would like to thank my parents Pavel and Šárka for never doubting me and supporting me when I decided for science, my sister Martina all the honest and encouraging talks we had (and for helping me with Python). And finally, great thanks belong to my wife Hanka for her patience

during my long trips to Germany, for always standing by my side, for cheering me up when I was low, for all scientific conversations we had and all the tips on academic writing.

9. Bibliography

(1) *Enerdata - Total energy consuption*. https://yearbook.enerdata.net/total-energy/world-consumption-statistics.html (accessed 2023-06-02).

(2) *Enerdata - Total final energy consumption*. https://eneroutlook.enerdata.net/forecast-world-final-energy-consumption.html (accessed 2023-06-02).

(3) *IPCC 2018 - Intergovernmental Panel on Climate Change. Special Report, Global Warming of 1.5°C, Summary for Policymakers*. https://www.ipcc.ch/ (accessed 2023-06-02).

(4) IPCC. *Global Warming of 1.5°C*; Cambridge University Press, 2022. https://doi.org/10.1017/9781009157940.

(5) Detz, R. J.; van der Zwaan, B. Transitioning towards Negative CO2 Emissions. *Energy Policy* **2019**, *133*, 110938. https://doi.org/10.1016/j.enpol.2019.110938.

(6) Scarlat, N.; Dallemand, J.-F.; Monforti-Ferrario, F.; Banja, M.; Motola, V. Renewable Energy Policy Framework and Bioenergy Contribution in the European Union – An Overview from National Renewable Energy Action Plans and Progress Reports. *Renewable and Sustainable Energy Reviews* **2015**, *51*, 969–985. https://doi.org/10.1016/j.rser.2015.06.062.

(7) European Commission. *Energy Roadmap 2050*. https://energy.ec.europa.eu/system/files/2014-10/roadmap2050_ia_20120430_en_0.pdf (accessed 2023-06-05).

(8) European Council. *Conclusions on 2030 Climate and Energy Policy Framework*. https://www.eea.europa.eu/policy-documents/european-council-23-24-10 (accessed 2023-06-05).

(9) Liu, C.; Li, F.; Ma, L.-P.; Cheng, H.-M. Advanced Materials for Energy Storage. *Advanced Materials* **2010**, *22* (8), E28–E62. https://doi.org/10.1002/adma.200903328.

(10) Zakeri, B.; Syri, S. Electrical Energy Storage Systems: A Comparative Life Cycle Cost Analysis. *Renewable and Sustainable Energy Reviews* **2015**, *42*, 569–596. https://doi.org/10.1016/j.rser.2014.10.011.

(11) Schlögl, R. The Revolution Continues: Energiewende 2.0. *Angewandte Chemie International Edition* **2015**, *54* (15), 4436–4439. https://doi.org/10.1002/anie.201405876.

(12) Lewis, N. S. Toward Cost-Effective Solar Energy Use. *Science (1979)* **2007**, *315* (5813), 798–801. https://doi.org/10.1126/science.1137014.

(13) Olabi, A. G.; Onumaegbu, C.; Wilberforce, T.; Ramadan, M.; Abdelkareem, M. A.; Al – Alami, A. H. Critical Review of Energy Storage Systems. *Energy* **2021**, *214*, 118987. https://doi.org/10.1016/j.energy.2020.118987.

(14) Blanco, H.; Faaij, A. A Review at the Role of Storage in Energy Systems with a Focus on Power to Gas and Long-Term Storage. *Renewable and Sustainable Energy Reviews* **2018**, *81*, 1049–1086. https://doi.org/10.1016/j.rser.2017.07.062.

(15) Zhang, F.; Zhao, P.; Niu, M.; Maddy, J. The Survey of Key Technologies in Hydrogen Energy Storage. *Int J Hydrogen Energy* **2016**, *41* (33), 14535–14552. https://doi.org/10.1016/j.ijhydene.2016.05.293.

(16) Hanley, E. S.; Deane, J.; Gallachóir, B. Ó. The Role of Hydrogen in Low Carbon Energy Futures–A Review of Existing Perspectives. *Renewable and Sustainable Energy Reviews* **2018**, *82*, 3027–3045. https://doi.org/10.1016/j.rser.2017.10.034.

(17) Abe, J. O.; Popoola, A. P. I.; Ajenifuja, E.; Popoola, O. M. Hydrogen Energy, Economy and Storage: Review and Recommendation. *Int J Hydrogen Energy* **2019**, *44* (29), 15072–15086. https://doi.org/10.1016/j.ijhydene.2019.04.068.

(18) Bhandari, R.; Trudewind, C. A.; Zapp, P. Life Cycle Assessment of Hydrogen Production via Electrolysis – a Review. *J Clean Prod* **2014**, *85*, 151–163. https://doi.org/10.1016/j.jclepro.2013.07.048.

(19) Gahleitner, G. Hydrogen from Renewable Electricity: An International Review of Power-to-Gas Pilot Plants for Stationary Applications. *Int J Hydrogen Energy* **2013**, *38* (5), 2039–2061. https://doi.org/10.1016/j.ijhydene.2012.12.010.

(20) Falcão, D. S.; Pinto, A. M. F. R. A Review on PEM Electrolyzer Modelling: Guidelines for Beginners. *J Clean Prod* **2020**, *261*, 121184. https://doi.org/10.1016/j.jclepro.2020.121184.

(21) Usman, M. R. Hydrogen Storage Methods: Review and Current Status. *Renewable and Sustainable Energy Reviews* **2022**, *167*, 112743. https://doi.org/10.1016/j.rser.2022.112743.

(22) Dalebrook, A. F.; Gan, W.; Grasemann, M.; Moret, S.; Laurenczy, G. Hydrogen Storage: Beyond Conventional Methods. *Chemical Communications* **2013**, *49* (78), 8735–8751. https://doi.org/10.1039/c3cc43836h.

(23) Abe, J. O.; Popoola, A. P. I.; Ajenifuja, E.; Popoola, O. M. Hydrogen Energy, Economy and Storage: Review and Recommendation. *Int J Hydrogen Energy* **2019**, *44* (29), 15072–15086. https://doi.org/10.1016/j.ijhydene.2019.04.068.

(24) Tarkowski, R. Underground Hydrogen Storage: Characteristics and Prospects. *Renewable and Sustainable Energy Reviews* **2019**, *105*, 86–94. https://doi.org/10.1016/j.rser.2019.01.051.

(25) Lim, K. L.; Kazemian, H.; Yaakob, Z.; Daud, W. R. W. Solid-State Materials and Methods for Hydrogen Storage: A Critical Review. *Chem Eng Technol* **2010**, *33* (2), 213–226. https://doi.org/10.1002/ceat.200900376.

(26) Shet, S. P.; Shanmuga Priya, S.; Sudhakar, K.; Tahir, M. A Review on Current Trends in Potential Use of Metal-Organic Framework for Hydrogen Storage. *Int J Hydrogen Energy* **2021**, *46* (21), 11782–11803. https://doi.org/10.1016/j.ijhydene.2021.01.020.

(27) Bénard, P.; Chahine, R. Storage of Hydrogen by Physisorption on Carbon and Nanostructured Materials. *Scr Mater* **2007**, *56* (10), 803–808. https://doi.org/10.1016/j.scriptamat.2007.01.008.

(28) Niaz, S.; Manzoor, T.; Pandith, A. H. Hydrogen Storage: Materials, Methods and Perspectives. *Renewable and Sustainable Energy Reviews* **2015**, *50*, 457–469. https://doi.org/10.1016/j.rser.2015.05.011.

(29) Bellosta von Colbe, J.; Ares, J.-R.; Barale, J.; Baricco, M.; Buckley, C.; Capurso, G.; Gallandat, N.; Grant, D. M.; Guzik, M. N.; Jacob, I.; Jensen, E. H.; Jensen, T.; Jepsen, J.; Klassen, T.; Lototskyy, M. V.; Manickam, K.; Montone, A.; Puszkiel, J.; Sartori, S.; Sheppard, D. A.; Stuart, A.; Walker, G.; Webb, C. J.; Yang, H.; Yartys, V.; Züttel, A.; Dornheim, M. Application of Hydrides in Hydrogen Storage and Compression: Achievements, Outlook and Perspectives. *Int J Hydrogen Energy* **2019**, *44* (15), 7780–7808. https://doi.org/10.1016/j.ijhydene.2019.01.104.

(30) Tarasov, B. P.; Fursikov, P. V.; Volodin, A. A.; Bocharnikov, M. S.; Shimkus, Y. Y.; Kashin, A. M.; Yartys, V. A.; Chidziva, S.; Pasupathi, S.; Lototskyy, M. V. Metal Hydride Hydrogen Storage and Compression Systems for Energy Storage Technologies. *Int J Hydrogen Energy* **2021**, *46* (25), 13647–13657. https://doi.org/10.1016/j.ijhydene.2020.07.085.

(31) Luo, Y.; Wang, Q.; Li, J.; Xu, F.; Sun, L.; Zou, Y.; Chu, H.; Li, B.; Zhang, K. Enhanced Hydrogen Storage/Sensing of Metal Hydrides by Nanomodification. *Mater Today Nano* **2020**, *9*, 100071. https://doi.org/10.1016/j.mtnano.2019.100071.

(32) Aziz, M.; Wijayanta, A. T.; Nandiyanto, A. B. D. Ammonia as Effective Hydrogen Storage: A Review on Production, Storage and Utilization. *Energies (Basel)* **2020**, *13* (12), 3062. https://doi.org/10.3390/en13123062.

(33) He, T.; Pei, Q.; Chen, P. Liquid Organic Hydrogen Carriers. *Journal of Energy Chemistry*. Elsevier B.V. September 1, 2015, pp 587–594. https://doi.org/10.1016/j.jechem.2015.08.007.

(34) Preuster, P.; Papp, C.; Wasserscheid, P. Liquid Organic Hydrogen Carriers (LOHCs): Toward a Hydrogen-Free Hydrogen Economy. *Acc Chem Res* **2017**, *50* (1), 74–85. https://doi.org/10.1021/acs.accounts.6b00474.

(35) Niermann, M.; Beckendorff, A.; Kaltschmitt, M.; Bonhoff, K. Liquid Organic Hydrogen Carrier (LOHC) – Assessment Based on Chemical and Economic Properties. *International Journal of Hydrogen Energy*. Elsevier Ltd March 8, 2019, pp 6631–6654. https://doi.org/10.1016/j.ijhydene.2019.01.199.

(36) Sekine, Y.; Higo, T. Recent Trends on the Dehydrogenation Catalysis of Liquid Organic Hydrogen Carrier (LOHC): A Review. *Top Catal* **2021**, *64* (7–8), 470–480. https://doi.org/10.1007/s11244-021-01452-x.

(37) Bourane, A.; Elanany, M.; Pham, T. V.; Katikaneni, S. P. An Overview of Organic Liquid Phase Hydrogen Carriers. *International Journal of Hydrogen Energy*. Elsevier Ltd December 28, 2016, pp 23075–23091. https://doi.org/10.1016/j.ijhydene.2016.07.167.

(38) Wei, C.; Rao, R. R.; Peng, J.; Huang, B.; Stephens, I. E. L.; Risch, M.; Xu, Z. J.; Shao-Horn, Y. Recommended Practices and Benchmark Activity for Hydrogen and Oxygen Electrocatalysis in Water Splitting and Fuel Cells. *Advanced Materials* **2019**, *31* (31), 1806296. https://doi.org/10.1002/adma.201806296.

(39) Xiao, F.; Wang, Y.; Wu, Z.; Chen, G.; Yang, F.; Zhu, S.; Siddharth, K.; Kong, Z.; Lu, A.; Li, J.; Zhong, C.; Zhou, Z.; Shao, M. Recent Advances in Electrocatalysts for Proton Exchange Membrane Fuel Cells and Alkaline Membrane Fuel Cells. *Advanced Materials* **2021**, *33* (50), 2006292. https://doi.org/10.1002/adma.202006292.

(40) Zhu, J.; Hu, L.; Zhao, P.; Lee, L. Y. S.; Wong, K.-Y. Recent Advances in Electrocatalytic Hydrogen Evolution Using Nanoparticles. *Chem Rev* **2020**, *120* (2), 851–918. https://doi.org/10.1021/acs.chemrev.9b00248.

(41) Gong, Y.; Yao, J.; Wang, P.; Li, Z.; Zhou, H.; Xu, C. Perspective of Hydrogen Energy and Recent Progress in Electrocatalytic Water Splitting. *Chin J Chem Eng* **2022**, *43*, 282–296. https://doi.org/10.1016/j.cjche.2022.02.010.

(42) Wang, S.; Lu, A.; Zhong, C.-J. Hydrogen Production from Water Electrolysis: Role of Catalysts. *Nano Converg* **2021**, *8* (1), 4. https://doi.org/10.1186/s40580-021-00254-x.

(43) Pollet, B. G.; Kocha, S. S.; Staffell, I. Current Status of Automotive Fuel Cells for Sustainable Transport. *Curr Opin Electrochem* **2019**, *16*, 90–95. https://doi.org/10.1016/j.coelec.2019.04.021.

(44) Du, L.; Prabhakaran, V.; Xie, X.; Park, S.; Wang, Y.; Shao, Y. Low-PGM and PGM-Free Catalysts for Proton Exchange Membrane Fuel Cells: Stability Challenges and Material Solutions. *Advanced Materials* **2021**, *33* (6), 1908232. https://doi.org/10.1002/adma.201908232.

(45) Sauer, J.; Freund, H.-J. Models in Catalysis. *Catal Letters* **2015**, *145* (1), 109–125. https://doi.org/10.1007/s10562-014-1387-1.

(46) Ertl, G. Elementary Steps in Heterogeneous Catalysis. *Angewandte Chemie International Edition in English*. 1990, pp 1219–1227. https://doi.org/10.1002/anie.199012191.

(47) Ertl, G. Reactions at Surfaces: From Atoms to Complexity (Nobel Lecture). *Angewandte Chemie - International Edition* **2008**, *47* (19), 3524–3535. https://doi.org/10.1002/anie.200800480.

(48) Lykhach, Y.; Kozlov, S. M.; Skála, T.; Tovt, A.; Stetsovych, V.; Tsud, N.; Dvořák, F.; Johánek, V.; Neitzel, A.; Mysliveček, J.; Fabris, S.; Matolín, V.; Neyman, K. M.; Libuda, J. Counting Electrons on Supported Nanoparticles. *Nat Mater* **2016**, *15* (3), 284–288. https://doi.org/10.1038/nmat4500.

(49) Faisal, F.; Stumm, C.; Bertram, M.; Waidhas, F.; Lykhach, Y.; Cherevko, S.; Xiang, F.; Ammon, M.; Vorokhta, M.; Šmíd, B.; Skála, T.; Tsud, N.; Neitzel, A.; Beranová, K.; Prince, K. C.; Geiger, S.; Kasian, O.; Wähler, T.; Schuster, R.; Schneider, M. A.; Matolín, V.; Mayrhofer, K. J. J.; Brummel, O.; Libuda, J. Electrifying Model Catalysts for Understanding Electrocatalytic Reactions in Liquid Electrolytes. *Nat Mater* **2018**, *17* (7), 592–598. https://doi.org/10.1038/s41563-018-0088-3.

(50) Abdel-Mageed, A. M.; Rungtaweevoranit, B.; Impeng, S.; Bansmann, J.; Rabeah, J.; Chen, S.; Häring, T.; Namuangrak, S.; Faungnawakij, K.; Brückner, A.; Behm, R. J. Unveiling the CO Oxidation Mechanism over a Molecularly Defined Copper Single-Atom Catalyst Supported on a Metal–Organic Framework. *Angewandte Chemie International Edition* **2023**, *62* (30). https://doi.org/10.1002/anie.202301920.

(51) Libuda, J.; Schauermann, S.; Laurin, M.; Schalow, T.; Freund, H. J. Model Studies in Heterogeneous Catalysis. From Structure to Kinetics. *Monatsh Chem* **2005**, *136* (1), 59–75. https://doi.org/10.1007/s00706-004-0249-8.

(52) Clavilier, J.; Faure, R.; Guinet, G.; Durand, R. Preparation of Monocrystalline Pt Microelectrodes and Electrochemical Study of the Plane Surfaces Cut in the Direction of the {111} and {110} Planes. *J Electroanal Chem Interfacial Electrochem* **1980**, *107* (1), 205–209. https://doi.org/10.1016/S0022-0728(79)80022-4.

(53) O'Grady, W. E.; Woo, M. Y. C.; Hagans, P. L.; Yeager, E. Electrode Surface Studies by Leed–Auger. *Journal of Vacuum Science and Technology* **1977**, *14* (1), 365–368. https://doi.org/10.1116/1.569208.

(54) Kolb, D. M. Electrochemical Surface Science: Past, Present and Future. *Journal of Solid State Electrochemistry* **2011**, *15* (7–8), 1391–1399. https://doi.org/10.1007/s10008-011-1396-6.

(55) Markovic, N. M.; Ross, P. N. Surface Science Studies of Model Fuel Cell Electrocatalysts. *Surf Sci Rep* **2002**, *45* (4–6), 117–229.

(56) Brummel, O.; Libuda, J. Electrifying Oxide Model Catalysis: Complex Electrodes Based on Atomically-Defined Oxide Films. *Catal Letters* **2020**, *150* (6), 1546–1560. https://doi.org/10.1007/s10562-019-03078-x.

(57) Sun, Y.; Gao, S.; Lei, F.; Xie, Y. Atomically-Thin Two-Dimensional Sheets for Understanding Active Sites in Catalysis. *Chem Soc Rev* **2015**, *44* (3), 623–636. https://doi.org/10.1039/C4CS00236A.

(58) Faisal, F.; Bertram, M.; Stumm, C.; Cherevko, S.; Geiger, S.; Kasian, O.; Lykhach, Y.; Lytken, O.; Mayrhofer, K. J. J.; Brummel, O.; Libuda, J. Atomically Defined Co3O4(111) Thin Films Prepared in Ultrahigh Vacuum: Stability under Electrochemical Conditions. *Journal of Physical Chemistry C* **2018**, *122* (13), 7236–7248. https://doi.org/10.1021/acs.jpcc.8b00558.

(59) Faisal, F.; Stumm, C.; Bertram, M.; Wähler, T.; Schuster, R.; Xiang, F.; Lytken, O.; Katsounaros, I.; Mayrhofer, K. J. J.; Schneider, M. A.; Brummel, O.; Libuda, J. Atomically-Defined Model Catalysts in Ultrahigh Vacuum and in Liquid Electrolytes: Particle Size-Dependent CO Adsorption on Pt Nanoparticles on Ordered Co3O4(111) Films. *Physical Chemistry Chemical Physics* **2018**, *20* (36), 23702–23716. https://doi.org/10.1039/c8cp03770a.

(60) Rodríguez, J. A.; Hrbek, J. Inverse Oxide/Metal Catalysts: A Versatile Approach for Activity Tests and Mechanistic Studies. *Surf Sci* **2010**, *604* (3–4), 241–244. https://doi.org/10.1016/j.susc.2009.11.038.

(61) Yu, W.; Porosoff, M. D.; Chen, J. G. Review of Pt-Based Bimetallic Catalysis: From Model Surfaces to Supported Catalysts. *Chem Rev* **2012**, *112* (11), 5780–5817. https://doi.org/10.1021/cr300096b.

(62) Ertl, G.; Freund, H.-J. Catalysis and Surface Science. *Phys Today* **1999**, *52* (1), 32–38. https://doi.org/10.1063/1.882569.

(63) Faisal, F.; Bertram, M.; Stumm, C.; Waidhas, F.; Brummel, O.; Libuda, J. Preparation of Complex Model Electrocatalysts in Ultra-High Vacuum and Transfer into the Electrolyte for Electrochemical IR Spectroscopy and Other Techniques. *Review of Scientific Instruments* **2018**, *89* (11). https://doi.org/10.1063/1.5047056.

(64) Cherevko, S.; Geiger, S.; Kasian, O.; Kulyk, N.; Grote, J.-P.; Savan, A.; Shrestha, B. R.; Merzlikin, S.; Breitbach, B.; Ludwig, A.; Mayrhofer, K. J. J. Oxygen and Hydrogen Evolution Reactions on Ru, RuO 2 , Ir, and IrO 2 Thin Film Electrodes in Acidic and Alkaline Electrolytes: A Comparative Study on Activity and Stability. *Catal Today* **2016**, *262*, 170–180. https://doi.org/10.1016/j.cattod.2015.08.014.

(65) Stumm, C.; Bertram, M.; Kastenmeier, M.; Speck, F. D.; Sun, Z.; Rodríguez-Fernández, J.; Lauritsen, J. V.; Mayrhofer, K. J. J.; Cherevko, S.; Brummel, O.; Libuda, J. Structural Dynamics of

Ultrathin Cobalt Oxide Nanoislands under Potential Control. *Adv Funct Mater* **2021**, *31* (13). https://doi.org/10.1002/adfm.202009923.

(66) Bertram, M.; Prössl, C.; Ronovský, M.; Knöppel, J.; Matvija, P.; Fusek, L.; Skála, T.; Tsud, N.; Kastenmeier, M.; Matolín, V.; Mayrhofer, K. J. J.; Johánek, V.; Mysliveček, J.; Cherevko, S.; Lykhach, Y.; Brummel, O.; Libuda, J. Cobalt Oxide-Supported Pt Electrocatalysts: Intimate Correlation between Particle Size, Electronic Metal–Support Interaction and Stability. *J Phys Chem Lett* **2020**, 8365–8371. https://doi.org/10.1021/acs.jpclett.0c02233.

(67) Gasperi, G.; Luches, P.; Barth, C. Stability of Ultra-Thin Ceria Films on Pt (111) Exposed to Air and Treated in Redox Cycles. **2018**, No. 111. https://doi.org/10.1021/acs.jpcc.8b07231.

(68) Králik, M. Adsorption, Chemisorption, and Catalysis. *Chemical Papers* **2014**, *68* (12). https://doi.org/10.2478/s11696-014-0624-9.

(69) Subbaraman, R.; Tripkovic, D.; Chang, K. C.; Strmcnik, D.; Paulikas, A. P.; Hirunsit, P.; Chan, M.; Greeley, J.; Stamenkovic, V.; Markovic, N. M. Trends in Activity for the Water Electrolyser Reactions on 3d M(Ni,Co,Fe,Mn) Hydr(Oxy)Oxide Catalysts. *Nat Mater* **2012**, *11* (6), 550–557. https://doi.org/10.1038/nmat3313.

(70) Danilovic, N.; Subbaraman, R.; Strmcnik, D.; Chang, K. C.; Paulikas, A. P.; Stamenkovic, V. R.; Markovic, N. M. Enhancing the Alkaline Hydrogen Evolution Reaction Activity through the Bifunctionality of Ni(OH)2/Metal Catalysts. *Angewandte Chemie - International Edition* **2012**, *51* (50), 12495–12498. https://doi.org/10.1002/anie.201204842.

(71) Vo, T.-G.; Tsai, P.-Y.; Chiang, C.-Y. Tuning Selectivity and Activity of the Electrochemical Glycerol Oxidation Reaction by Manipulating Morphology and Exposed Facet of Spinel Cobalt Oxides. *J Catal* **2023**, *424*, 64–73. https://doi.org/10.1016/j.jcat.2023.05.010.

(72) Libuda, J.; Görling, A. Functional Molecular Structures on Complex Oxide Surfaces. *Surf Sci* **2023**, *729*, 122237. https://doi.org/10.1016/j.susc.2022.122237.

(73) Grätzel, M. Dye-Sensitized Solar Cells. *Journal of Photochemistry and Photobiology C: Photochemistry Reviews* **2003**, *4* (2), 145–153. https://doi.org/10.1016/S1389-5567(03)00026-1.

(74) Hagfeldt, A.; Boschloo, G.; Sun, L.; Kloo, L.; Pettersson, H. Dye-Sensitized Solar Cells. *Chem Rev* **2010**, *110* (11), 6595–6663. https://doi.org/10.1021/cr900356p.

(75) Joachim, C.; Gimzewski, J. K.; Aviram, A. Electronics Using Hybrid-Molecular and Mono-Molecular Devices. *Nature* **2000**, *408* (6812), 541–548. https://doi.org/10.1038/35046000.

(76) Jurow, M.; Schuckman, A. E.; Batteas, J. D.; Drain, C. M. Porphyrins as Molecular Electronic Components of Functional Devices. *Coord Chem Rev* **2010**, *254* (19–20), 2297–2310. https://doi.org/10.1016/j.ccr.2010.05.014.

(77) Kaushik, A.; Kumar, R.; Arya, S. K.; Nair, M.; Malhotra, B. D.; Bhansali, S. Organic–Inorganic Hybrid Nanocomposite-Based Gas Sensors for Environmental Monitoring. *Chem Rev* **2015**, *115* (11), 4571–4606. https://doi.org/10.1021/cr400659h.

(78) Ekrami, M.; Magna, G.; Emam-Djomeh, Z.; Yarmand, M. S.; Paolesse, R.; Di Natale, C. Porphyrin-Functionalized Zinc Oxide Nanostructures for Sensor Applications. *Sensors (Switzerland)* **2018**, *18* (7), 1–12. https://doi.org/10.3390/s18072279.

(79) van Deelen, T. W.; Hernández Mejía, C.; de Jong, K. P. Control of Metal-Support Interactions in Heterogeneous Catalysts to Enhance Activity and Selectivity. *Nature Catalysis*. Nature Publishing Group November 1, 2019, pp 955–970. https://doi.org/10.1038/s41929-019-0364-x.

(80) Lauritsen, J. V.; Nyberg, M.; Nørskov, J. K.; Clausen, B. S.; Topsøe, H.; Lægsgaard, E.; Besenbacher, F. Hydrodesulfurization Reaction Pathways on MoS2 Nanoclusters Revealed by Scanning Tunneling Microscopy. *J Catal* **2004**, *224* (1), 94–106. https://doi.org/10.1016/j.jcat.2004.02.009.

(81) Senanayake, S. D.; Stacchiola, D.; Rodriguez, J. A. Unique Properties of Ceria Nanoparticles Supported on Metals: Novel Inverse Ceria/Copper Catalysts for CO Oxidation and the Water-Gas Shift Reaction. *Acc Chem Res* **2013**, *46* (8), 1702–1711. https://doi.org/10.1021/ar300231p.

(82) Wang, Y.; Wang, D.; Li, Y. A Fundamental Comprehension and Recent Progress in Advanced Pt-based ORR Nanocatalysts. *SmartMat* **2021**, *2* (1), 56–75. https://doi.org/10.1002/smm2.1023.

(83) Laursen, A. B.; Varela, A. S.; Dionigi, F.; Fanchiu, H.; Miller, C.; Trinhammer, O. L.; Rossmeisl, J.; Dahl, S. Electrochemical Hydrogen Evolution: Sabatier's Principle and the Volcano Plot. *J Chem Educ* **2012**, *89* (12), 1595–1599. https://doi.org/10.1021/ed200818t.

(84) Lykhach, Y.; Brummel, O.; Bruix, A.; Fabris, S.; Matolínová, I.; Matolín, V.; Neyman, K. M.; Libuda, J. Pt–CeO2 Catalysts for Fuel Cell Applications: From Surface Science to Electrochemistry. In *Encyclopedia of Interfacial Chemistry*; Elsevier, 2018; pp 189–201. https://doi.org/10.1016/B978-0-12-409547-2.14155-1.

(85) Brummel, O.; Waidhas, F.; Faisal, F.; Fiala, R.; Vorokhta, M.; Khalakhan, I.; Dubau, M.; Figueroba, A.; Kovács, G.; Aleksandrov, H. A.; Vayssilov, G. N.; Kozlov, S. M.; Neyman, K. M.; Matolín, V.; Libuda, J. Stabilization of Small Platinum Nanoparticles on Pt–CeO_2 Thin Film Electrocatalysts During Methanol Oxidation. *The Journal of Physical Chemistry C* **2016**, *120* (35), 19723–19736. https://doi.org/10.1021/acs.jpcc.6b05962.

(86) Lykhach, Y.; Bruix, A.; Fabris, S.; Potin, V.; Matolínová, I.; Matolín, V.; Libuda, J.; Neyman, K. M. Oxide-Based Nanomaterials for Fuel Cell Catalysis: The Interplay between Supported Single Pt Atoms and Particles. *Catal Sci Technol* **2017**, *7* (19), 4315–4345. https://doi.org/10.1039/C7CY00710H.

(87) Wang, A.; Li, J.; Zhang, T. Heterogeneous Single-Atom Catalysis. *Nat Rev Chem* **2018**, *2* (6), 65–81. https://doi.org/10.1038/s41570-018-0010-1.

(88) Suchorski, Y.; Wrobel, R.; Becker, S.; Weiss, H. CO Oxidation on a CeOx/Pt(111) Inverse Model Catalyst Surface: Catalytic Promotion and Tuning of Kinetic Phase Diagrams. *Journal of Physical Chemistry C* **2008**, *112* (50), 20012–20017. https://doi.org/10.1021/jp806033v.

(89) Li, Y.; Fu, Q.; Flytzani-Stephanopoulos, M. Low-Temperature Water-Gas Shift Reaction over Cu- and Ni-Loaded Cerium Oxide Catalysts. *Appl Catal B* **2000**, *27* (3), 179–191. https://doi.org/10.1016/S0926-3373(00)00147-8.

(90) Xu, C.; Shen, P. K. Electrochamical Oxidation of Ethanol on Pt-CeO2/C Catalysts. *J Power Sources* **2005**, *142* (1–2), 27–29. https://doi.org/10.1016/j.jpowsour.2004.10.017.

(91) Qi, G.; Yang, R. T.; Chang, R. MnOx-CeO2 Mixed Oxides Prepared by Co-Precipitation for Selective Catalytic Reduction of NO with NH3 at Low Temperatures. *Appl Catal B* **2004**, *51* (2), 93–106. https://doi.org/10.1016/j.apcatb.2004.01.023.

(92) Eyring, L. Chapter 27 The Binary Rare Earth Oxides; 1979; pp 337–399. https://doi.org/10.1016/S0168-1273(79)03010-5.

(93) TROVARELLI, A. Catalytic Properties of Ceria and CeO $_2$ -Containing Materials. *Catalysis Reviews* **1996**, *38* (4), 439–520. https://doi.org/10.1080/01614949608006464.

(94) Mullins, D. R. The Surface Chemistry of Cerium Oxide. *Surf Sci Rep* **2015**, *70* (1), 42–85. https://doi.org/10.1016/j.surfrep.2014.12.001.

(95) Fiala, R.; Figueroba, A.; Bruix, A.; Vaclavu, M.; Rednyk, A.; Khalakhan, I.; Vorokhta, M.; Lavkova, J.; Illas, F.; Potin, V.; Matolinova, I.; Neyman, K. M.; Matolin, V. High Efficiency of Pt2+- CeO2 Novel Thin Film Catalyst as Anode for Proton Exchange Membrane Fuel Cells. *Appl Catal B* **2016**, *197*, 262–270. https://doi.org/10.1016/j.apcatb.2016.02.036.

(96) Mori, T.; Ou, D. R.; Zou, J.; Drennan, J. Present Status and Future Prospect of Design of Pt–Cerium Oxide Electrodes for Fuel Cell Applications. *Progress in Natural Science: Materials International* **2012**, *22* (6), 561–571. https://doi.org/10.1016/j.pnsc.2012.11.010.

(97) Salaev, M. A.; Salaeva, A. A.; Kharlamova, T. S.; Mamontov, G. V. Pt–CeO2-Based Composites in Environmental Catalysis: A Review. *Appl Catal B* **2021**, *295*, 120286. https://doi.org/10.1016/j.apcatb.2021.120286.

(98) Luches, P.; Valeri, S. Structure, Morphology and Reducibility of Epitaxial Cerium Oxide Ultrathin Films and Nanostructures. **2015**, 5818–5833. https://doi.org/10.3390/ma8095278.

(99) Luches, P.; Pagliuca, F.; Valeri, S. Structural and Morphological Modifications of Thermally Reduced Cerium Oxide Ultrathin Epitaxial Films on Pt (111). *Physical Chemistry Chemical Physics* **2014**, *16* (111), 18848–18857. https://doi.org/10.1039/C4CP02723J.

(100) Luches, P.; Pagliuca, F.; Valeri, S. Morphology, Stoichiometry, and Interface Structure of CeO2 Ultrathin Films on Pt(111). *Journal of Physical Chemistry C* **2011**, *115* (21), 10718–10726. https://doi.org/10.1021/jp201139y.

(101) Luches, P.; Pagliuca, F.; Valeri, S.; Boscherini, F. Structure of Ultrathin CeO 2 Films on Pt(111) by Polarization- Dependent X - Ray Absorption Fine Structure. **2012**, No. 111.

(102) Luches, P.; Gasperi, G.; Sauerbrey, M.; Valeri, S.; Falta, J.; Flege, J. I. Dynamics of the Interaction between Ceria and Platinum during Redox Processes. *Front Chem* **2019**, *7* (FEB), 1–11. https://doi.org/10.3389/fchem.2019.00057.

(103) Sauerbrey, M.; Gasperi, G.; Luches, P.; Falta, J.; Valeri, S.; Flege, J. I. Cerium Oxide Epitaxial Nanostructures on Pt(111): Growth, Morphology and Structure. *Top Catal* **2017**, *60* (6–7), 513–521. https://doi.org/10.1007/s11244-016-0716-6.

(104) Iravani, S.; Varma, R. S. Sustainable Synthesis of Cobalt and Cobalt Oxide Nanoparticles and Their Catalytic and Biomedical Applications. *Green Chemistry* **2020**, *22* (9), 2643–2661. https://doi.org/10.1039/D0GC00885K.

(105) Eranna, G.; Joshi, B. C.; Runthala, D. P.; Gupta, R. P. Oxide Materials for Development of Integrated Gas Sensors—A Comprehensive Review. *Critical Reviews in Solid State and Materials Sciences* **2004**, *29* (3–4), 111–188. https://doi.org/10.1080/10408430490888977.

(106) Nitta, N.; Wu, F.; Lee, J. T.; Yushin, G. Li-Ion Battery Materials: Present and Future. *Materials Today* **2015**, *18* (5), 252–264. https://doi.org/10.1016/j.mattod.2014.10.040.

(107) Osgood, H.; Devaguptapu, S. V.; Xu, H.; Cho, J.; Wu, G. Transition Metal (Fe, Co, Ni, and Mn) Oxides for Oxygen Reduction and Evolution Bifunctional Catalysts in Alkaline Media. *Nano Today* **2016**, *11* (5), 601–625. https://doi.org/10.1016/j.nantod.2016.09.001.

(108) Royer, S.; Duprez, D. Catalytic Oxidation of Carbon Monoxide over Transition Metal Oxides. *ChemCatChem* **2011**, *3* (1), 24–65. https://doi.org/10.1002/cctc.201000378.

(109) Ferstl, P.; Mehl, S.; Arman, M. A.; Schuler, M.; Toghan, A.; Laszlo, B.; Lykhach, Y.; Brummel, O.; Lundgren, E.; Knudsen, J.; Hammer, L.; Schneider, M. A.; Libuda, J. Adsorption and Activation of CO on Co_3O_4 (111) Thin Films. *The Journal of Physical Chemistry C* **2015**, *119* (29), 16688–16699. https://doi.org/10.1021/acs.jpcc.5b04145.

(110) Bai, B.; Qiao, Q.; Li, J.; Hao, J. Progress in Research on Catalysts for Catalytic Oxidation of Formaldehyde. *Chinese Journal of Catalysis* **2016**, *37* (1), 102–122. https://doi.org/10.1016/S1872-2067(15)61007-5.

(111) Buchner, F.; Fuchs, S.; Behm, R. J. UHV Preparation and Electrochemical/-Catalytic Properties of Well-Defined Co– and Fe-Containing Unary and Binary Oxide Model Cathodes for the Oxygen Reduction and Oxygen Evolution Reaction in Zn-Air Batteries. *Journal of Electroanalytical Chemistry* **2021**, *896*, 115497. https://doi.org/10.1016/j.jelechem.2021.115497.

(112) Buchner, F.; Eckardt, M.; Böhler, T.; Kim, J.; Gerlach, J.; Schnaidt, J.; Behm, R. J. Oxygen Reduction and Evolution on Ni-modified Co_3O_4 (1 1 1) Cathodes for Zn–Air Batteries: A Combined Surface Science and Electrochemical Model Study. *ChemSusChem* **2020**, *13* (12), 3199–3211. https://doi.org/10.1002/cssc.202000503.

(113) Werner, K.; Mohr, S.; Schwarz, M.; Xu, T.; Amende, M.; Döpper, T.; Görling, A.; Libuda, J. Functionalized Porphyrins on an Atomically Defined Oxide Surface: Anchoring and Coverage-Dependent Reorientation of MCTPP on Co_3O_4 (111). *J Phys Chem Lett* **2016**, *7* (3), 555–560. https://doi.org/10.1021/acs.jpclett.5b02784.

(114) Xu, T.; Schwarz, M.; Werner, K.; Mohr, S.; Amende, M.; Libuda, J. Structure-Dependent Anchoring of Organic Molecules to Atomically Defined Oxide Surfaces: Phthalic Acid on Co_3O_4 (111), CoO(100), and CoO(111). *Chemistry – A European Journal* **2016**, *22* (15), 5384–5396. https://doi.org/10.1002/chem.201504810.

(115) Heinz, K.; Hammer, L. Epitaxial Cobalt Oxide Films on Ir(100)—the Importance of Crystallographic Analyses. *Journal of Physics: Condensed Matter* **2013**, *25* (17), 173001. https://doi.org/10.1088/0953-8984/25/17/173001.

(116) Biedermann, K.; Gubo, M.; Hammer, L.; Heinz, K. Phases and Phase Transitions of Hexagonal Cobalt Oxide Films on Ir(100)-(1 × 1). *Journal of Physics Condensed Matter* **2009**, *21* (18). https://doi.org/10.1088/0953-8984/21/18/185003.

(117) Meyer, W.; Biedermann, K.; Gubo, M.; Hammer, L.; Heinz, K. Surface Structure of Polar Co 3 O 4 (111) Films Grown Epitaxially on Ir(100)-(1 × 1). *Journal of Physics: Condensed Matter* **2008**, *20* (26), 265011. https://doi.org/10.1088/0953-8984/20/26/265011.

(118) Binnig G.; Rohrer H. Scanning Tunneling Microscopy. *Helvetica Physica Acta* **1982**, *55* (6), 726–735. https://doi.org/10.5169/seals-115309.

(119) Cohen-Tannoudji, C.; Diu, B.; Laloë, F.; Hemley, S. R.; Ostrowsky, N.; Ostrowsky, D. *QUANTUM MECHANICS Volume I Basic Concepts, Tools, and Applications*.

(120) Fowler R. H.; Nordheim L. Electron Emission in Intense Electric Fields. *Proc. R. Soc. Lond.* **1928**, 173–181.

(121) Bardeen, J. Tunnelling from a Many-Particle Point of View. *Phys Rev Lett* **1961**, *6* (2), 57–59. https://doi.org/10.1103/PhysRevLett.6.57.

(122) Chen J. C. *Introduction to Scanning Tunneling Microscopy*; Oxford Science Publications, 2008.

(123) Chen, C. J. Theory of Scanning Tunneling Spectroscopy. *Journal of Vacuum Science & Technology A: Vacuum, Surfaces, and Films* **1988**, *6* (2), 319–322. https://doi.org/10.1116/1.575444.

(124) Tersoff, J.; Hamann, D. R. *Theory and Application for the Scanning Tunneling Microscope*; 1985; Vol. 50.

(125) Tersoff ', J.; Hamann, D. R. *Theory of the Scanning Tunneling Microscope*; 1985; Vol. 31.

(126) Bocquet, M. L.; Wang, B. Metal-Organic Interaction Probed by First Principles STM Simulations. *Progress in Surface Science*. September 2010, pp 435–459. https://doi.org/10.1016/j.progsurf.2010.09.001.

(127) Hofer, W. A.; Foster, A. S.; Shluger, A. L. *Theories of Scanning Probe Microscopes at the Atomic Scale*.

(128) Kratzer, P.; Neugebauer, J. The Basics of Electronic Structure Theory for Periodic Systems. *Frontiers in Chemistry*. Frontiers Media S.A. 2019. https://doi.org/10.3389/fchem.2019.00106.

(129) Julian Chen, C.; Julian, C. *Scanning Tunneling Microscopy: A Chemical Perspective*; 1993; Vol. 7. https://digitalcommons.usu.edu/microscopyAvailableat:https://digitalcommons.usu.edu/microscopy/vol7/iss3/4.

(130) Feuchtwang, T.; Cutler, P.; Kazes, E.; Feuchtwang, T. E.; Cutler, P. H. COMMENTS ON THE THEORY OF THE RESOLUTION IN THE SCANNING TUNNELING MICROSCOPE (STM) AND THE STRUCTURE OF THE TUNNELING BARRIER COMMENTS ON THE THEORY OF THE RESOLUTION I N THE SCANNING TUNNELING MICROSCOPE (STM) AND THE STRUCTURE OF THE TUNNELING BARRIER. *Journal de Physique Colloques* **1984**, *45* (C9). https://doi.org/10.1051/jphyscol:1984920ï.

(131) Lippmann G. Principle de La Conservation de l'electricitea Ou Second Principle de La Theorie Des Phenomenes Electriques . *J. de Phys.* **1881**, *10*, 381–394.

(132) Curie J.; Curie P. Deformation Electrique Du Quartz. *Comptes Rendus* **1882**, *95*, 914–917.

(133) Van De Leemput, L. E. C.; Rongen, P. H. H.; Timmerman, B. H.; Van Kempen, H. Calibration and Characterization of Piezoelectric Elements as Used in Scanning Tunneling Microscopy. *Review of Scientific Instruments* **1991**, *62* (4), 989–992. https://doi.org/10.1063/1.1141989.

(134) Binnig, G.; Smith, D. P. E. Single-Tube Three-Dimensional Scanner for Scanning Tunneling Microscopy. *Review of Scientific Instruments* **1986**, *57* (8), 1688–1689. https://doi.org/10.1063/1.1139196.

(135) Garcia, N. *Theory of Scanning Tunneling Microscopy and Spectroscopy: Resolution, Image and Field States, and Thin Oxide Layers*; 1986.

(136) Song, J. P.; Pryds, N. H.; Glejbøl, K.; Mørch, K. A.; Thölén, A. R.; Christensen, L. N. A Development in the Preparation of Sharp Scanning Tunneling Microscopy Tips. *Review of Scientific Instruments* **1993**, *64* (4), 900–903. https://doi.org/10.1063/1.1144140.

(137) Einstein Albert. Über Einen Die Erzeugung Und Verwandlung Des Lichtes Betreffenden Heuristischen Gesichtspunkt. *Ann Phys* **1905**, *17* (132), 132–148.

(138) Briggs David. XPS: Basic Principles, Spectral Features and Qualitative Analysis. In *Surface Analysis by Auger and X-Ray Photoelectron Spectroscopy*; Briggs David, Grant John T., Eds.; IM Publications and SurfaceSpectra Limited, 2003; pp 31–57.

(139) Yang, D.-Q.; Sacher, E. *Initial-and Final-State Effects on Metal Cluster/Substrate Interactions, as Determined by XPS: Copper Clusters on Dow Cyclotene and Highly Oriented Pyrolytic Graphite*.

(140) Roberts, F. S.; Anderson, S. L.; Reber, A. C.; Khanna, S. N. Initial and Final State Effects in the Ultraviolet and X-Ray Photoelectron Spectroscopy (UPS and XPS) of Size-Selected Pdn Clusters Supported on TiO2(110). *Journal of Physical Chemistry C* **2015**, *119* (11), 6033–6046. https://doi.org/10.1021/jp512263w.

(141) Seah Martin P. Instrument Calibration for AES and XPS. In *Surface Analysis by Auger and X-Ray Photoelectron Spectroscopy*; Briggs D., Grant John T., Eds.; IM Publications, 2003; pp 167–210.

(142) Kövér Laszlo. Chemical Effects in XPS. In *Surface Analysis by Auger and X-Ray Photoelectron Spectroscopy*; Briggs D., Grant John T., Eds.; IM Publications, 2003.

(143) John F. Moulder. *Handbook of X-Ray Photoelectron Spectroscopy*; 1992.

(144) Eckertová Ludmila. *Metody Analýzy Povrchů - Elektronová Spektroskopie*; Academia: Prague, 1990.

(145) Manne, R.; Aberg, T. KOOPMANS' THEOREM FOR INNER-SHELL IONIZATION. *Chem Phys Lett* **1970**, *7*.

(146) Grant John T. AES: Basic Principles, Spectral Features and Quantitative Analysis. In *Surface Analysis by Auger and X-Ray Photoelectron Spectroscopy*; Briggs David, Grant John T., Eds.; IM Publications, 2003.

(147) Tanuma, S.; Powell, C. J.; Penn, D. R. Calculations of Electron Inelastic Mean Free Paths (IMFPs): VI. Analysis of the Gries Inelastic Scattering Model and Predictive IMFP Equation. *Surface and Interface Analysis* **1997**, *25* (1), 25–35. https://doi.org/10.1002/(SICI)1096-9918(199701)25:1<25::AID-SIA207>3.0.CO;2-2.

(148) Whitten, J. E. Ultraviolet Photoelectron Spectroscopy: Practical Aspects and Best Practices. *Applied Surface Science Advances* **2023**, *13*, 100384. https://doi.org/10.1016/j.apsadv.2023.100384.

(149) Matolín, V.; Cabala, M.; Cháb, V.; Matolínová, I.; Prince, K. C.; Škoda, M.; Šutara, F.; Skála, T.; Veltruská, K. A Resonant Photoelectron Spectroscopy Study of Sn(O_x) Doped CeO_2 Catalysts. *Surface and Interface Analysis* **2008**, *40* (3–4), 225–230. https://doi.org/10.1002/sia.2625.

(150) Lykhach, Y.; Piccinin, S.; Skála, T.; Bertram, M.; Tsud, N.; Brummel, O.; Farnesi Camellone, M.; Beranová, K.; Neitzel, A.; Fabris, S.; Prince, K. C.; Matolín, V.; Libuda, J. Quantitative Analysis of the Oxidation State of Cobalt Oxides by Resonant Photoemission Spectroscopy. *J Phys Chem Lett* **2019**, *10* (20), 6129–6136. https://doi.org/10.1021/acs.jpclett.9b02398.

(151) Benito, N.; Galindo, R. E.; Rubio-Zuazo, J.; Castro, G. R.; Palacio, C. High- and Low-Energy x-Ray Photoelectron Techniques for Compositional Depth Profiles: Destructive versus Non-Destructive Methods. *J Phys D Appl Phys* **2013**, *46* (6), 065310. https://doi.org/10.1088/0022-3727/46/6/065310.

(152) Reihl, B.; Mårtensson, N.; Eastman, D. E.; Arko, A. J.; Vogt, O. Resonant Photoemission as a Tool to Study <math Display="inline"> <mi>f</Mi> </Math> and <math Display="inline"> <mi>d</Mi> </Math> Electrons in Actinide Compounds. *Phys Rev B* **1982**, *26* (4), 1842–1851. https://doi.org/10.1103/PhysRevB.26.1842.

(153) Matolín, V.; Sedláček, L.; Matolínová, I.; Šutara, F.; Skála, T.; Šmíd, B.; Libra, J.; Nehasil, V.; Prince, K. C. Photoemission Spectroscopy Study of Cu/CeO_2 Systems: Cu/CeO_2 Nanosized Catalyst and CeO_2 (111)/Cu(111) Inverse Model Catalyst. *The Journal of Physical Chemistry C* **2008**, *112* (10), 3751–3758. https://doi.org/10.1021/jp077739g.

(154) Hoffmann, F. M. *INFRARED REFLECTION-ABSORPTION SPECTROSCOPY OF ADSORBED MOLECULES*; North-Holland Publishing Company, 1983; Vol. 3.

(155) Bradshaw A.M.; Schweizer E. Infrared Reflection-Absorption Spectroscopy of Adsorbed Molescules. In *Spectroscopy of Surfaces*; Clark R. J. H., Hester R. E., Eds.; John Wiley & Sons.

(156) Steele Derek. Infrared Spectroscopy: Theory. In *Handbook of Vibrational Spectroscopy vol. 1: Theory and Instumentation*; Wiley, 2002.

(157) Christy A. A.; Ozaki Y.; Gregoriou V. G. *Modern Fourier Transform Infrared Spectroscopy*; Elsevier, 2001.

(158) Greenler, R. G. Infraredc Study of Adsorbed Molecules on Metal Surfaces by Reflection Tehniques. *J Chem Phys* **1966**, *44* (1), 310–315. https://doi.org/10.1063/1.1726462.

(159) Richards P. L.; Tobin R. G. Infrared Spectroscopy of Adsorbates on Metals: Direct Absorption and Emission. In *Vibrational Spectroscopy of Molecules in Surfaces*; Yates J. T., Madey T. E., Eds.; Springer, 1987.

(160) Werner, K.; Mohr, S.; Schwarz, M.; Xu, T.; Amende, M.; Döpper, T.; Görling, A.; Libuda, J. Functionalized Porphyrins on an Atomically Defined Oxide Surface: Anchoring and Coverage-Dependent Reorientation of MCTPP on Co3O4(111). *Journal of Physical Chemistry Letters* **2016**, *7* (3), 555–560. https://doi.org/10.1021/acs.jpclett.5b02784.

(161) Yang, C.; Wöll, C. IR Spectroscopy Applied to Metal Oxide Surfaces: Adsorbate Vibrations and Beyond. *Advances in Physics: X*. Taylor and Francis Ltd. March 4, 2017, pp 373–408. https://doi.org/10.1080/23746149.2017.1296372.

(162) Zamlynny, V.; Lipkowski, J. Quantitative SNIFTIRS and PM IRRAS of Organic Molecules at Electrode Surfaces; Wiley-VCH, 2006; pp 315–376. https://doi.org/10.1002/9783527616817.ch9.

(163) Bewick, A.; Kunimatsu, K. *INFRA RED SPECTROSCOPY OF THE ELECTRODE-ELECTROLYTE INTERPHASE*; 1980; Vol. 101.

(164) Bewick, A.; Kunlmatsu, K.; Pans, S. *Infra Red Spectroscopy of the Electrode-Electrolyte Interphase*.

(165) Iwasita, T.; Nart, F. C. *IN SITU INFRARED SPECTROSCOPY AT ELECTROCHEMICAL INTERFACES*; 1997; Vol. 55.

(166) Iwasita, T.; Nart, F. C. *Bulk Effects in External Reflection IR Spectroscopy The Interpretation of Adsorption Data for Ionic Species*; Elsevier Sequoia S.A, 1990.

(167) Corrigan, D. S.; Weaver, M. J. *THE INTERPRETATION OF SOLUTION ELECTROLYTE VIBRATIONAL BANDS IN POTENTIAL-DIFFERENCE INFRARED SPECTROSCOPY*; 1988; Vol. 239.

(168) Lambert, D. K. Stark Effect of Adsorbate Vibrations. *Solid State Commun* **1984**, *51* (5), 297–300. https://doi.org/10.1016/0038-1098(84)90691-4.

(169) Cuesta, A. Composition, Structure, and Reaction Dynamics at Electrode-Electrolyte Interfaces Using Infrared Spectroscopy. In *Vibrational Spectroscopy at Electrified Interfaces*; John Wiley & Sons, Inc.: Hoboken, NJ, USA, 2013; pp 266–306. https://doi.org/10.1002/9781118658871.ch8.

(170) Nečas, D.; Klapetek, P. Gwyddion: An Open-Source Software for SPM Data Analysis. *Open Physics* **2012**, *10* (1). https://doi.org/10.2478/s11534-011-0096-2.

(171) Brummel, O.; Waidhas, F.; Bauer, U.; Wu, Y.; Bochmann, S.; Steinrück, H.-P.; Papp, C.; Bachmann, J.; Libuda, J. Photochemical Energy Storage and Electrochemically Triggered Energy Release in the Norbornadiene–Quadricyclane System: UV Photochemistry and IR Spectroelectrochemistry in a Combined Experiment. *J Phys Chem Lett* **2017**, *8* (13), 2819–2825. https://doi.org/10.1021/acs.jpclett.7b00995.

(172) Skala Tomas. *MSB Beamline Overview*. https://www.elettra.eu/lightsources/elettra/elettra-beamlines/msb/manual-beamline-overview/all.html (accessed 2023-05-25).

(173) Matolín, V.; Libra, J.; Matolínová, I.; Nehasil, V.; Sedláček, L.; Šutara, F. Growth of Ultra-Thin Cerium Oxide Layers on Cu(1 1 1). *Appl Surf Sci* **2007**, *254* (1), 153–155. https://doi.org/10.1016/j.apsusc.2007.07.010.

(174) Sauerbrey, G. Verwendung von Schwingquarzen Zur Wägung Dünner Schichten Und Zur Mikrowägung. *Zeitschrift für Physik* **1959**, *155* (2), 206–222. https://doi.org/10.1007/BF01337937.

(175) Luches, P.; Giordano, L.; Grillo, V.; Gazzadi, G. C.; Prada, S.; Campanini, M.; Bertoni, G.; Magen, C.; Pagliuca, F.; Pacchioni, G.; Valeri, S. Atomic Scale Structure and Reduction of Cerium Oxide

at the Interface with Platinum. *Adv Mater Interfaces* **2015**, *2* (18), 1–10. https://doi.org/10.1002/admi.201500375.

(176) van Deelen, T. W.; Hernández Mejía, C.; de Jong, K. P. Control of Metal-Support Interactions in Heterogeneous Catalysts to Enhance Activity and Selectivity. *Nat Catal* **2019**, *2* (11), 955–970. https://doi.org/10.1038/s41929-019-0364-x.

(177) Fusek, L.; Farnesi Camellone, M.; Ronovský, M.; Kastenmeier, M.; Skála, T.; Kumar Samal, P.; Tsud, N.; Mehl, S.; Škvára, J.; Dolák, T.; Uvarov, V.; Setvín, M.; Johánek, V.; Fabris, S.; Brummel, O.; Libuda, J.; Mysliveček, J.; Piccinin, S.; Lykhach, Y. Atomistic Picture of Electronic Metal Support Interaction and the Role of Water. *J Mater Chem A Mater* **2024**, *12* (6), 3258–3264. https://doi.org/10.1039/D3TA06595B.

(178) Rice, P. S.; Hu, P. Understanding Supported Noble Metal Catalysts Using First-Principles Calculations. *J Chem Phys* **2019**, *151* (18). https://doi.org/10.1063/1.5126090.

(179) Kastenmeier, M.; Fusek, L.; Mohamed, F.; Schuschke, C.; Ronovský, M.; Skála, T.; Farnesi Camellone, M.; Tsud, N.; Johánek, V.; Fabris, S.; Libuda, J.; Piccinin, S.; Lykhach, Y.; Mysliveček, J.; Brummel, O. Pd/Co_3O_4 (111) Interface Formation. *The Journal of Physical Chemistry C* **2023**, *127* (12), 6034–6044. https://doi.org/10.1021/acs.jpcc.3c00261.

(180) Wertheim, G. K.; DiCenzo, S. B. Cluster Growth and Core-Electron Binding Energies in Supported Metal Clusters. *Phys Rev B* **1988**, *37* (2), 844–847. https://doi.org/10.1103/PhysRevB.37.844.

(181) Stará, I.; Gruzza, B.; Matolín, V. EELS Investigation of Pd Thin Film Growth on Aluminum Oxide Substrate. *J Electron Spectros Relat Phenomena* **2001**, *114–116*, 575–580. https://doi.org/10.1016/S0368-2048(00)00337-6.

(182) Schuschke, C.; Fusek, L.; Uvarov, V.; Vorokhta, M.; Šmíd, B.; Johánek, V.; Lykhach, Y.; Libuda, J.; Mysliveček, J.; Brummel, O. Stability of the Pd/Co 3 O 4 (111) Model Catalysts in Oxidizing and Humid Environments. *The Journal of Physical Chemistry C* **2021**, *125* (5), 2907–2917. https://doi.org/10.1021/acs.jpcc.0c08915.

(183) Liu, L.; Corma, A. Structural Transformations of Solid. *Nat Rev Chem* **2021**, *5* (April). https://doi.org/10.1038/s41570-021-00255-8.

(184) Campbell, C. T.; Mao, Z. Chemical Potential of Metal Atoms in Supported Nanoparticles: Dependence upon Particle Size and Support. *ACS Catal* **2017**, *7* (12), 8460–8466. https://doi.org/10.1021/acscatal.7b03090.

(185) Kastenmeier, M.; Fusek, L.; Deng, X.; Skála, T.; Mehl, S.; Tsud, N.; Grau, S.; Stumm, C.; Uvarov, V.; Johánek, V.; Libuda, J.; Lykhach, Y.; Mysliveček, J.; Brummel, O. Particle Size and Shape Effects in Electrochemical Environments: Pd Particles Supported on Ordered Co_3O_4 (111) and Highly Oriented Pyrolytic Graphite. *The Journal of Physical Chemistry C* **2022**, *126* (30), 12870–12881. https://doi.org/10.1021/acs.jpcc.2c03109.

(186) Trovarelli, A. *Catalysis by Ceria and Related Materials*; 2005; Vol. 2. https://doi.org/10.1016/j.cattod.2004.12.016.

(187) Fusek, L.; Samal, P. K.; Keresteš, J.; Khalakhan, I.; Johánek, V.; Lykhach, Y.; Libuda, J.; Brummel, O.; Mysliveček, J. A Model Study of Ceria–Pt Electrocatalysts: Stability, Redox Properties and

Hydrogen Intercalation. *Physical Chemistry Chemical Physics* **2024**, *26* (3), 1630–1639. https://doi.org/10.1039/D3CP03831A.

(188) Neal, C. J.; Sakthivel, T. S.; Fu, Y.; Seal, S. Aging of Nanoscale Cerium Oxide in a Peroxide Environment: Its Influence on the Redox, Surface, and Dispersion Character. *The Journal of Physical Chemistry C* **2021**, *125* (49), 27323–27334. https://doi.org/10.1021/acs.jpcc.1c06279.

(189) Duchoň, T.; Dvořák, F.; Aulická, M.; Stetsovych, V.; Vorokhta, M.; Mazur, D.; Veltruská, K.; Skála, T.; Mysliveček, J.; Matolínová, I.; Matolín, V. Ordered Phases of Reduced Ceria As Epitaxial Films on Cu(111). *The Journal of Physical Chemistry C* **2014**, *118* (1), 357–365. https://doi.org/10.1021/jp409220p.

(190) Hayes, S. A.; Yu, P.; O'Keefe, T. J.; O'Keefe, M. J.; Stoffer, J. O. The Phase Stability of Cerium Species in Aqueous Systems. *J Electrochem Soc* **2002**, *149* (12), C623. https://doi.org/10.1149/1.1516775.

(191) Subbaraman, R.; Tripkovic, D.; Strmcnik, D.; Chang, K. C.; Uchimura, M.; Paulikas, A. P.; Stamenkovic, V. R.; Markovic, N. M. Enhancing Hydrogen Evolution Activity in Water Splitting by Tailoring Li+-Ni(OH)2-Pt Interfaces. *Science (1979)* **2011**, *334* (6060), 1256–1260. https://doi.org/10.1126/science.1211934.

(192) Bertram, M.; Schuschke, C.; Waidhas, F.; Schwarz, M.; Hohner, C.; Montero, M. A.; Brummel, O.; Libuda, J. Molecular Anchoring to Oxide Surfaces in Ultrahigh Vacuum and in Aqueous Electrolytes: Phosphonic Acids on Atomically-Defined Cobalt Oxide. *Physical Chemistry Chemical Physics* **2019**, *21* (42), 23364–23374. https://doi.org/10.1039/c9cp03779a.

(193) Fusek, L.; Kastenmeier, M.; Franz, E.; Fromm, L.; Görling, A.; Brummel, O.; Libuda, J. Anchoring of Porphyrins on Atomically Defined Cobalt Oxide: In-Situ Infrared Spectroscopy at the Electrified Solid/Liquid Interface. *Surf Sci* **2021**, *718* (October 2021), 122013. https://doi.org/10.1016/j.susc.2021.122013.

(194) Fusek, L.; Briega-Martos, V.; Minichová, M.; Fromm, L.; Franz, E.; Yang, J.; Görling, A.; Mayrhofer, K. J. J.; Wasserscheid, P.; Cherevko, S.; Brummel, O.; Libuda, J. Toward High-Energy-Density Fuels for Direct Liquid Organic Hydrogen Carrier Fuel Cells: Electrooxidation of 1-Cyclohexylethanol. *J Phys Chem Lett* **2024**, *15* (9), 2529–2536. https://doi.org/10.1021/acs.jpclett.3c03331.

10. Abbreviations

ATR	Attenuated total reflection
CU	Charles University
CV	Cyclic voltammetry
DCM	Dichloromethane
DFT	Density function theory
DSSC	Dye sensitized solar cell
EC	Electrochemical
EC-IRRAS	Electrochemical infrared reflection absorption spectroscopy
EC-LOHC	Electrochemicall active liquid organic hydrogen carrier
EMSI	Electronic metal-support interaction
FAU	Friedriech-Alexander University Eralngen-Nürnberg
FC	Fuel cell
FCC	Face centered cubic
FTIR	Fourier transformed infrared
HER	Hydrogen evolution reaction
HOPG	Highly ordered pyrolytic graphite
HT	High temperature
IMFP	Inelastic mean free path
IP	Ion pump
IR	Infrared
IRRAS	Infrared reflection absorption spectroscopy
LEED	Low energy electron diffraction
LOHC	Liquid organic hydrogen carrier
LT	Low temperature
LN_2	Liquid nitrogen
MCT	Mercury-cadmium-telluride
MLE	Monolayer equivalent
MPTPP	Monophosphonatophenyltriphenyl porphirin
MSB	Material Science Beamline
MSSR	Metal-surface selection rule
NAP	Near ambient pressure
ORR	Oxygen reduction reaction
PEMFC	Proton exchange membrane fuel cell
PTFE	Polytetrafluorethylen (teflon)
PVD	Physical vapor deposition
QCM	Quartz crystal microbalance
QMS	Quadrupole mass spectrometer
RES	Renewable energy sources
RHE	Reference hydrogen electrode
RPES	Resonant photoemission spectroscopy
SP	Scroll pump
SRPES	Synchrotron radiation photoelectron spectroscopy
STM	Scanning tunneling microscopy

TMP	Turbomolecular pump
UHV	Ultrahigh vacuum
UPS	Ultra-violet photoelectron spectroscopy
WGS	Water gas shift
XPS	X-ray photoelectron spectroscopy

11. List of publications

[P1] **Atomistic Picture of Electronic Metal Support Interaction and the Role of Water**
Fusek, L.; Farnesi Camellone, M.; Ronovský, M.; Kastenmeier, M.; Skála, T.; Kumar Samal, P.; Tsud, N.; Mehl, S.; Škvára, J.; Dolák, T.; Uvarov, V.; Setvín, M.; Johánek, V.; Fabris, S.; Brummel, O.; Libuda, J.; Mysliveček, J.; Piccinin, S.; Lykhach, Y.
Journal of Materials Chemistry A 2024, *12* (6), 3258–3264
DOI: 10.1039/D3TA06595B

[P2] **Pd/Co $_3$ O $_4$ (111) Interface Formation**
Kastenmeier, M.; Fusek, L.; Mohamed, F.; Schuschke, C.; Ronovský, M.; Skála, T.; Farnesi Camellone, M.; Tsud, N.; Johánek, V.; Fabris, S.; Libuda, J.; Piccinin, S.; Lykhach, Y.; Mysliveček, J.; Brummel, O.
The Journal of Physical Chemistry C 2023, *127* (12), 6034–6044.
DOI: 10.1021/acs.jpcc.3c00261

[P3] **Stability of the Pd/Co 3 O 4 (111) Model Catalysts in Oxidizing and Humid Environments**
Schuschke, C.; Fusek, L.; Uvarov, V.; Vorokhta, M.; Šmíd, B.; Johánek, V.; Lykhach, Y.; Libuda, J.; Mysliveček, J.; Brummel, O.
The Journal of Physical Chemistry C 2021, *125* (5), 2907–2917
DOI: 10.1021/acs.jpcc.0c08915

[P4] **Particle Size and Shape Effects in Electrochemical Environments: Pd Particles Supported on Ordered Co $_3$ O $_4$ (111) and Highly Oriented Pyrolytic Graphite**
Kastenmeier, M.; Fusek, L.; Deng, X.; Skála, T.; Mehl, S.; Tsud, N.; Grau, S.; Stumm, C.; Uvarov, V.; Johánek, V.; Libuda, J.; Lykhach, Y.; Mysliveček, J.; Brummel, O.
The Journal of Physical Chemistry C 2022, *126* (30), 12870–12881
DOI: 10.1021/acs.jpcc.2c03109

[P5] **A Model Study of Ceria–Pt Electrocatalysts: Stability, Redox Properties and Hydrogen Intercalation**
Fusek, L.; Samal, P. K.; Keresteš, J.; Khalakhan, I.; Johánek, V.; Lykhach, Y.; Libuda, J.; Brummel, O.; Mysliveček, J.
Physical Chemistry Chemical Physics 2024, *26* (3), 1630–1639
DOI: 10.1039/D3CP03831A

[P6] **Anchoring of Porphyrins on Atomically Defined Cobalt Oxide: In-Situ Infrared Spectroscopy at the Electrified Solid/Liquid Interface**
Fusek, L.; Kastenmeier, M.; Franz, E.; Fromm, L.; Görling, A.; Brummel, O.; Libuda, J.
Surface Science 2021, *718* (October 2021), 122013
DOI: 10.1016/j.susc.2021.122013

[P7] **Toward High-Energy-Density Fuels for Direct Liquid Organic Hydrogen Carrier Fuel Cells: Electrooxidation of 1-Cyclohexylethanol**
Fusek, L.; Briega-Martos, V.; Minichová, M.; Fromm, L.; Franz, E.; Yang, J.; Görling, A.; Mayrhofer, K. J. J.; Wasserscheid, P.; Cherevko, S.; Brummel, O.; Libuda, J.
Journal of Physical Chemistry Letters 2024, *15* (9), 2529–2536
DOI: 10.1021/acs.jpclett.3c03331.